

Localized Corrosion Initiation of Steel in CO₂ Environments

A dissertation presented to
the faculty of
the Russ College of Engineering and Technology of Ohio University

In partial fulfillment
of the requirements for the degree
Doctor of Philosophy

Xin Gao
August 2020
© 2020 Xin Gao. All Rights Reserved.

This dissertation titled
Localized Corrosion Initiation of Steel in CO₂ Environments

by

XIN GAO

has been approved for
the Department of Chemical and Biomolecular Engineering
and the Russ College of Engineering and Technology by

Srdjan Nesic

Professor of Chemical and Biomolecular Engineering

Mei Wei

Dean, Russ College of Engineering and Technology

Abstract

GAO, XIN, Ph.D., August 2020, Chemical Engineering

Localized Corrosion Initiation of Steel in CO₂ Environments

Director of Dissertation: Srdjan Nesic

The objective of this dissertation research was to investigate initiation mechanisms for CO₂ localized corrosion on mild steel, encompassing the effects of chloride, oxygen, and acetic acid. In CO₂ corrosion, iron in steel will be oxidized to ferrous ions under deareated conditions. The ferrous and carbonate ions can combine to form FeCO₃ and precipitate once exceeding the solubility limit. When the precipitation of FeCO₃ occurs evenly on the steel surface it forms a compact and protective layer. This acts as a diffusion barrier hindering the mass transfer of electrochemical species and covers(blocks) the surface making it unavailable for corrosion, which enhances the resistance of mild steel to further uniform CO₂ corrosion. However, there are various scenarios where localized corrosion may occur. When the environment becomes more aggressive, the FeCO₃ could be partially removed. This leads to localized regions of the bare steel surface that become exposed to the corrosive solution and, subsequently, localized corrosion could be initiated.

To study CO₂ localized corrosion, two-stage experiments were performed: (1) a uniform protective FeCO₃ layer was first formed on a carbon steel with high initial FeCO₃ saturation; (2) localized CO₂ corrosion scenarios were then developed by adding

additional salts (NaCl or NaClO₄), oxygen or acetic acid to challenge the protective FeCO₃ layer.

The experiments were conducted in a two-liter glass cell with a three-electrode system, working electrode (X65 carbon steel), reference electrode (Ag/AgCl saturated electrode), and counter electrode (platinum). Electrochemical measurements (linear polarization resistance) were carried out to observe electrochemical behaviors and calculate the corrosion rates. Weight loss was also used to determine general corrosion rates. Fe²⁺ concentration was measured using spectrophotometry in order to study the solubilization of FeCO₃. Scanning electron microscopy (SEM), energy dispersive X-ray spectroscopy (EDS), X-ray diffraction (XRD), and profilometry by infinite focus microscopy (IFM) were used to determine pitting.

The results in non-ideal solutions showed that no localized corrosion was initiated by introducing more salt. The introduction of acetic acid resulted in localized corrosion. When oxygen was introduced, severe pitting occurred. A new water chemistry model based on Oddo & Tomson's equation was proposed by the author. Based on EQCM results, a new model to calculate the solubility constant of iron carbonate in non-ideal solution at 80°C was developed based on Sun & Nesic model.

Dedication

To

My Family

Acknowledgments

I would like first to express my deepest gratitude and appreciation to my advisor, Dr. Srdjan Nesic, who offered me the Ph.D study opportunity and invaluable guidance and generous support through the journey. I feel very fortunate to have Dr. Nesic as my advisor. Without his patience, encouragement, and support (including allowing me to take the long maternity leave that I needed), it would be impossible for me to finish my Ph.D. study.

I want to take this opportunity to thank Dr. Bruce Brown, my project leader, for his always taking care of my experimental needs, taking many discussion notes when I presented my work, and offering advice to my research. I also want to express my gratitude to both Dr. Bruce Brown and Dr. David Young for their generosity of reviewing and improving my proposal and dissertation. Thanks also go to Dr. Marc Singer, Dr. Gheorghe Bota and Dr. Xi Wang for their helpful discussion in meetings.

I would like to specially thank Dr. Ramgopal Thodla at DNV GL Columbus and greatly appreciate his generosity to allow me conduct one important chapter of my dissertation work in his research laboratory and use his lab resources.

I would also like to thank our business coordinator, Mrs. Rebecca Gill. She was always nice to me and very helpful with many administrative issues I had to resolve. I would also like to thank Tom Riggs for helping answer all the questions and prepare all the forms related to my Ph.D. program.

Thanks also go to our engineers and technicians, Mr. Danny Cain, Mr. Phil Bullington, Mr. Al Schubert, Mr. Cody Shafer and Mr. Alexis Barxias for their technical assistance.

I am especially thankful to my colleagues, Jing Ning, Yougui Zheng, Peng Jin, and Marijan Babic for their accompaniment through the journey especially when I needed to do experiments late in the night. Thanks also go to Zheng Ma and Fazlollah Madani Sani for their useful discussion.

I want to thank Dr. David Young, Dr. Kevin Crist, Dr. Monica Burdick, Dr. Jixin Chen, Dr. Lauren McMills and Dr. Douglas Green for their willingness to be my committee members and offering advice to my proposal/dissertation.

Thanks also go to all sponsors for Corrosion Center-Joint Industry Project for their financial support.

Lastly, I would like to show my deepest love and appreciation to my husband for his unwavering love, support, and patience. Without his support I would have never been here. I want to say thank you to my two lovely daughters for bringing the greatest joy to our life. And I am grateful to my parents and to my brother for their unconditional love and support.

Table of Contents

	Page
Abstract	3
Dedication	5
Acknowledgments.....	6
Table of Contents	8
List of Tables	11
List of Figures	12
Chapter 1: Introduction	19
1.1 CO ₂ General Corrosion	19
1.2 CO ₂ Localized Corrosion.....	22
1.2.1 Chloride Effect.....	25
1.2.2 Oxygen Effect	28
1.2.3 Acetic Acid Effect.....	30
Chapter 2: Research Objectives	32
Chapter 3: General CO ₂ Corrosion in Non-Ideal Solutions.....	34
3.1 Introduction.....	34
3.2 Water Chemistry	35
3.3 pH Measurement.....	37
3.4 Does the Expected pH from the Model Match the Measured pH?	38
3.5 Revision of the Current Water Chemistry Model.....	40
3.6 Validation of the New Model	44
3.7 Summary	46
Chapter 4: Effect of Chloride on Initiation of CO ₂ Localized Corrosion of Carbon Steel.....	47
4.1 Introduction.....	47
4.2 Hypotheses.....	47
4.3 Experimental Method.....	47
4.3.1 Experimental Setup	47
4.3.2 Experimental Procedure.....	48
4.4 Tests in NaCl Electrolyte	52
4.4.1 Results and Discussion	52
4.4.2 Summary I.....	67
4.5 Tests in NaClO ₄ solution.....	67

4.5.1 Why Change the Salt?.....	67
4.5.2 Results and Discussion	69
4.6 Summary	76
Chapter 5: Qualitative Study of the Equilibrium of FeCO ₃ Precipitation in Non-ideal Solutions	77
5.1 Introduction.....	77
5.2 Objective	78
5.3 Equilibrium of Iron Carbonate on an Iron Coated Quartz Crystal in High Concentration Salt Solution (without pH Adjustment).....	78
5.3.1 Experimental Method.....	78
5.3.2 Results and Discussion	83
5.4 Equilibrium of Iron Carbonate on an Iron Coated Quartz Crystal in High Salt Solution with pH Adjustment	86
5.4.1 Experimental Method.....	86
5.4.2 Results and Discussion	87
5.5 Equilibrium of Iron Carbonate on a Gold Coated Quartz Crystal in High Concentration Salt Solution (with pH Adjustment and Adding NaCl Gradually From 1 wt.% to 25 wt.%)	93
5.5.1 Experimental Method.....	93
5.5.2 Results and Discussion	95
5.6 Modelling	106
5.6.1 New Model Proposed.....	106
5.6.2 Verification of the New Proposed Model	110
5.6.3 Application of the New Model	113
5.7 Conclusions.....	117
Chapter 6: Effect of Acetic Acid on Localized Corrosion Initiation in CO ₂ Environments	118
6.1 Objective	118
6.2 Introduction.....	118
6.3 Hypotheses.....	119
6.4 Experimental Method.....	119
6.4.1 Experimental Setup.....	119
6.4.2 Experimental Procedure.....	119
6.5 Results.....	122

6.5.1 The Baseline Test in NaCl Electrolyte Without HAc	122
6.5.2 The Test in NaCl Electrolyte with 600 ppm Undissociated HAc.....	128
6.6 Discussion	136
6.7 Summary	137
Chapter 7: Localized Corrosion Initiation by O ₂ in CO ₂ Environments.....	138
7.1 Introduction.....	138
7.2 Experimental Setup.....	138
7.3 Experimental Procedure.....	139
7.4 Results.....	142
7.4.1 Test with 2.5 ppm of Dissolved O ₂	142
7.4.2 Test with 1.4 ppm of Dissolved O ₂	155
7.5 Discussion	166
7.6 Summary	168
Chapter 8: Conclusions and Future Work.....	170
Conclusions.....	170
Recommendations for future work	171
References.....	172
Appendix A: Procedure of Iron Ion Measurement	178
Appendix B: Calculation of General Corrosion Rate, Pitting Penetration Rate and Pitting Ratio.....	180
Appendix C: Calculation of the Dissolved Oxygen Concentration in The Glass Cell ...	183
Appendix D: Mass Change, SFeCO ₃ and pH Variation on a Polarized Au-coated Crystal at Various Accumulated NaCl concentrations from 10 wt.% to 25 wt.%.	186

List of Tables

	Page
Table 1 Weight of NaCl added for different salt concentrations	37
Table 2 Types of specimens used in this dissertation	49
Table 3 Test matrix for experiments in NaCl electrolyte	50
Table 4 Test conditions for experiments in NaClO ₄ electrolyte	51
Table 5 Weight loss results for the four tests.....	65
Table 6 Test conditions for experiments associated with aqueous equilibrium of FeCO ₃ on iron-coated quartz crystal.....	81
Table 7 Experimental conditions for the test of equilibrium of FeCO ₃ on Au-coated crystal	94
Table 8 The mass, pH and S _{FeCO₃} change with more NaCl addition.....	104
Table 9 The key experimental parameters for tests in Chapter 4	114
Table 10 Test conditions without HAc	120
Table 11 Test Conditions with HAc	121
Table 12 Test matrix for tests with O ₂	141
Table 13 Solubility of oxygen in NaCl solutions as a function of temperature and concentration[80]	185

List of Figures

	Page
Figure 1 Comparison of LPR corrosion rates measured at 5°C, pH 4.0 at 100 rpm (revolutions per minute), 1000 rpm and 6000 rpm. Taken from Fang [33]	26
Figure 2 Salt effect on LPR corrosion rate in CO ₂ sparged solutions (1000, 4000 rpm, pH 4, 20°C). Taken from Fang [33].....	26
Figure 3 The predicted and measured pH vs. NaCl concentrations at 80°C.....	39
Figure 4 The predicted and measured pH vs. NaCl concentrations at 50°C.....	39
Figure 5 The predicted and measured pH vs. NaCl concentrations at 30°C.....	40
Figure 6 CO ₂ solubility in NaCl solution (Oddo & Tomson's model and Li & Duan's model (calculated by F. Madani Sani) vs. experimental data from ref. [60] at 25°C).....	41
Figure 7 CO ₂ solubility in NaCl solution- the prediction of Oddo & Tomson's model vs. Li & Duan's model (calculated by F. Madani Sani) at 50°C.....	42
Figure 8 CO ₂ solubility in NaCl solution - the prediction of Oddo & Tomson's model vs. Li & Duan's model (calculated by F. Madani Sani) at 80°C.....	42
Figure 9 The best fit line (the black dot-line and the orange equation) for the K _{ca} equation.....	44
Figure 10 The predicted and measured pH vs. NaCl concentrations at 80°C.....	45
Figure 11 The predicted and measured pH vs. NaCl concentrations at 50°C.....	45
Figure 12 The predicted and measured pH vs. NaCl concentrations at 30°C.....	46
Figure 13 Glass cell setup	48
Figure 14 Surface morphology after the layer building process (0.1 wt.% NaCl electrolyte, 80 °C, initial pH 6.6, pCO ₂ 0.53 bar): (a): Test 1; (b):Test 2	55
Figure 15 Cross-section analysis after the layer building process (0.1 wt.% NaCl solution, 80°C, initial pH 6.6, pCO ₂ 0.53 bar) for Test 2	54
Figure 16 XRD results comparison for corrosion product formed in 1wt.% NaCl electrolyte at 80°C.....	54
Figure 17 Surface morphology after FeCO ₃ building process: (a): Test 3 (1 wt.% NaCl); (b): Test 4 (3 wt.% NaCl)	56
Figure 18 Cross-section analysis after FeCO ₃ building a): Test 3 (1 wt.% NaCl); (b): Test 4 (3 wt.% NaCl)	57
Figure 19 Surface morphology after adding more NaCl for: (a): Test 3 (1 wt.% NaCl); (b): Test 4 (3 wt.% NaCl)	59
Figure 20 Cross-section after adding more NaCl for: Test 3 (1 wt.% NaCl); (b): Test 4 (3 wt.% NaCl)	59

Figure 21 Surface morphology of specimens in Test 3 (10 wt.% NaCl) at the end of the experiment , (a) and (b) from two different specimens	60
Figure 22 Composition analysis of the corrosion layer by EDS of specimen in Test 3 (10 wt.% NaCl) at the end of the experiment.....	60
Figure 23 Surface morphology of specimens in Test 4 (15 wt.% NaCl) at the end of the experiment.....	61
Figure 24 Cross-section for: (a) Test 3 (10 wt.% NaCl); (b) Test 4 (15 wt.% NaCl).....	62
Figure 25 IFM images and analysis of the corrosion product layer after layer removal for: (a): Test 3 (1 wt.% NaCl); (b): Test 4 (3 wt.% NaCl).....	64
Figure 26 IFM images and analysis of the corrosion product layer after layer removal: (a): Test 3 (10 wt.% NaCl); (b): Test 4 (15 wt.% NaCl)	64
Figure 27 General corrosion rate comparison for the four tests defined in Table 3	66
Figure 28 Pit penetration rate with respect to the general corrosion rate for those four tests	67
Figure 29 Comparison of the calculated FeCO ₃ saturation values after adding chloride for the four tests (first points were before adding more salt)	68
Figure 30 Variance of SFeCO ₃ and pH of the solution with time (NaClO ₄ , 80 °C).....	69
Figure 31 Surface morphology after FeCO ₃ layer building process (1 wt.% NaClO ₄ solution, 80 °C)	70
Figure 32 Cross-section analysis after FeCO ₃ building process (1 wt.% NaClO ₄ solution, 80°C)	71
Figure 33 Surface morphology after adding more NaClO ₄ (6 days in 21 wt.% NaClO ₄ , 80°C)	72
Figure 34 Cross-section analysis after adding more NaClO ₄ (6 days at 21 wt.% NaClO ₄)	72
Figure 35 Surface morphology after adding more NaClO ₄ (12 days at 21 wt.% NaClO ₄)	73
Figure 36 Cross-Section analysis after adding more NaClO ₄ (12 days at 21 wt.% NaClO ₄)	73
Figure 37 IFM images and analysis of the corrosion product layer after layer removal (12 days at 21 wt.% NaClO ₄)	74
Figure 38 XRD results comparison for corrosion product formed at NaClO ₄ and NaCl (Test 3, 10 wt. % NaCl) solutions.....	75
Figure 39 Corrosion rate comparison between NaCl and NaClO ₄	76
Figure 40 Complete QCM setup consisting of Digital Controller, Crystal Oscillator, and Crystal Holder. Taken from [25]	79

Figure 41 Experimental setup with EQCM (Image courtesy of Cody Shafer, ICMT)[61]	80
Figure 42 Specially designed container for adding extra NaCl into the glass cell	80
Figure 43 Mass change (left y-axis) and SFeCO ₃ (right y-axis) obtained on Fe-coated quartz crystal in FeCO ₃ layer formation test at 80°C.....	84
Figure 44 Mass change (left) and SFeCO ₃ (right) obtained on a Fe-coated quartz crystal at 80°C	85
Figure 45 SEM image of iron carbonate layer formed on iron-coated quartz crystal at the end of the experiment.....	86
Figure 46 Mass change (left) and SFeCO ₃ (right) obtained on Fe-coated quartz crystal in FeCO ₃ layer formation test at 80°C and 1 wt.% NaCl.....	88
Figure 47 The pH variation in FeCO ₃ layer formation test at 80°C and 1 wt.% NaCl....	88
Figure 48 Mass change and SFeCO ₃ obtained on Fe-coated quartz crystal with pH adjustment by adding 1N HCl at 80°C. (pH adjusted from pH 6.2 to pH 5.2 at ~100 hours)	90
Figure 49 The pH variation after adding 1N HCl. (pH adjusted from pH 6.2 to pH 5.2 at ~100 hours)	90
Figure 50 Mass change (left) and SFeCO ₃ (right) obtained on Fe-coated quartz crystal with adding more NaCl (from 1 wt.% to 10 wt.%) at 80°C. (pH adjusted from pH 6.2 to pH 5.2 at ~100 hours, [NaCl] increased at 150 hours)	91
Figure 51 The pH variation on Fe-coated quartz crystal with adding more NaCl (from 1 wt.% to 10 wt.%) at 80°C. (pH adjusted from pH 6.2 to pH 5.2 at ~100 hours, [NaCl] increased at 150 hours)	92
Figure 52 SEM image iron coated quartz crystal at the end of the experiment.....	92
Figure 53 Mass change (left) and SFeCO ₃ (right) obtained on a polarized Au-coated quartz crystal in FeCO ₃ layer formation test at 80°C and 1 wt.% NaCl	96
Figure 54 The pH change in FeCO ₃ layer formation test at 80°C and 1 wt.% NaCl.....	97
Figure 55 Mass change (left) and SFeCO ₃ (right) obtained on a polarized Au-coated quartz crystal with pH adjustment by adding 1N HCl at 80°C and 1 wt.% NaCl. (pH adjusted from pH 6.3 to pH 5.0 at 22 hours)	98
Figure 56 The pH variation on a polarized Au-coated quartz crystal with pH adjustment by adding 1N HCl at 80°C and 1 wt.% NaCl. (pH adjusted from pH 6.3 to pH 5.0 at 22 hours)	99
Figure 57 Mass change and SFeCO ₃ obtained on a polarized Au-coated quartz crystal with adding more NaCl (from 1 wt.% to 3 wt.%). The right graph is the enlarged detail of the left one.....	100
Figure 58 Mass change (left) and SFeCO ₃ (right) obtained on a polarized Au-coated quartz crystal with adding more NaCl (3 wt.%)	101

Figure 59 Mass change (left) and SFeCO ₃ (right) obtained on a polarized Au-coated quartz crystal with adding more NaCl (from 3 wt.% to 5 wt.%)	102
Figure 60 Mass change (left) and the pH variation (right) on a polarized Au-coated quartz crystal with adding more NaCl (from 3 wt.% to 5 wt.%)	103
Figure 61 Mass change (left) and SFeCO ₃ (right) on a polarized Au-coated quartz crystal for the whole complete experiment	104
Figure 62 Mass change (left) and the pH variation (right) on a polarized Au-coated quartz crystal for the whole complete experiment	105
Figure 63 SEM image of iron carbonate layer formed on polarized (-700mV) Au-coated quartz crystal at the end of the experiment	106
Figure 64 Parity plot comparison of experimental pK _{sp} vs. calculated pK _{sp} from Sun & Nesic model at 80°C	108
Figure 65 Parity plot comparison of experimental pK _{sp} vs. calculated pK _{sp} from the new model with the new K _{ca} at 80°C	109
Figure 66 The best fit line for the modified pK _{sp} equation at 80°C	110
Figure 67 Parity plot comparison of experimental pK _{sp} vs. calculated pK _{sp} from the new model with the new K _{ca} and new K _{sp} at 80°C	111
Figure 68 Mass change (left) and SFeCO ₃ (right, recalculated based on K _{ca} adjusted model, equation(27)) on a polarized Au-coated quartz crystal for the whole complete experiment at 80°C	112
Figure 69 Mass change (left) and SFeCO ₃ (right, recalculated based on K _{ca} and K _{sp} adjusted model, equation (33)) on a polarized Au-coated quartz crystal for the whole complete experiment at 80°C	113
Figure 70 Comparison of the calculated SFeCO ₃ (K _{ca} based on equation (22) and K _{sp} based on equation (28)) values after adding more salt	115
Figure 71 Comparison of the calculated SFeCO ₃ (K _{ca} based on equation (27) and K _{sp} based on equation (28)) values after adding more salt	116
Figure 72 Comparison of the calculated SFeCO ₃ (K _{ca} based on equation (27) and K _{sp} based on equation (28)) values after adding more salt at 80°C	117
Figure 73 Schematic of periodic removal of flat weight loss specimens for the baseline experiment	121
Figure 74 Schematic of periodic removal of flat weight loss specimens for the experiment with 600 ppm HAc added	122
Figure 75 Change of bulk pH, ferrous ions concentration (measured) and iron carbonate saturation (calculated) with time (1 wt.% NaCl and 80°C)	123
Figure 76 Variation of corrosion rate and potential with test time (1 wt.% NaCl and 80 °C)	124

Figure 77 Surface and cross-section morphologies after iron carbonate layer formation process on day 4 (1 wt.% NaCl and 80°C)	125
Figure 78 XRD results comparison for corrosion product on day 4 and day 14 (1 wt.% NaCl and 80 °C).....	125
Figure 79 Surface and cross-section morphologies on day 7 (1 wt.% NaCl and 80°C). .	126
Figure 80 Surface and cross-section morphologies on day 14 (1 wt.% NaCl and 80 °C)	127
Figure 81 IFM images and analysis of the corrosion product layer after layer removal on day 14 (1 wt.% NaCl and 80 °C)	128
Figure 82 Change of bulk pH and $[Fe^{2+}]$ with time (1 wt.% NaCl and 80 °C).....	129
Figure 83 The variation of saturation of $FeCO_3$ with time (1 wt.% NaCl and 80 °C)....	130
Figure 84 Variation of corrosion rate and potential with test time as determined by LPR measurements (1 wt.% NaCl and 80 °C)	131
Figure 85 Surface and cross-section morphologies on day 4 (1 wt.% NaCl and 80 °C) 132	
Figure 86 Surface and cross-section analysis on day 7 with HAc (1 wt.% NaCl, 80 °C)	133
Figure 87 Surface and cross-section analysis on day 14 with HAc (1 wt.% NaCl, 80 °C)	134
Figure 88 XRD results comparison for corrosion product on day 4, day 7 and day 14 (1 wt.% NaCl, 80 °C)	134
Figure 89 IFM images and analysis of the corrosion product layer after layer removal on day 14 (1 wt.% NaCl, 80 °C)	135
Figure 90 The relationship between when the localized corrosion occurred with respect to the ionic strength.....	137
Figure 91 Glass cell setup used to determine the effect of O_2 on localized CO_2 corrosion	139
Figure 92 Schematic of periodic removal of flat weight loss specimens for 2.5 ppm dissolved O_2 added experiment.....	140
Figure 93 Schematic of periodic removal of flat weight loss specimens for 1.4 ppm dissolved O_2 added experiment.....	141
Figure 94 Change of measured bulk pH (red) and measured ferrous ion concentration (blue) (1 wt.% NaCl and 80 °C), 2.5 ppm of oxygen was continuously added from day 4	143
Figure 95 Variation of corrosion rate and corrosion potential with test time as determined by LPR (1 wt.% NaCl and 80 °C), 2.5 ppm of oxygen was continuously added from day 4.....	144
Figure 96 Surface morphology and cross-section after 4 days in 1 wt.% NaCl at 80°C 145	

Figure 97 Surface morphology after 1 days in 2.5 ppm O ₂ (1 wt.% NaCl and 80 °C) ...	146
Figure 98 Composition analysis of the corrosion product by EDS after 1 in 2.5 ppm O ₂ (1 wt.% NaCl and 80 °C)	147
Figure 99 XRD analysis after 1 days in 2.5 ppm O ₂ (1 wt.% NaCl and 80 °C)	147
Figure 100 Cross-section after 1 days in 2.5 ppm O ₂ (1 wt.% NaCl and 80 °C).....	148
Figure 101 Surface morphology after 4 days in 2.5 ppm O ₂ (1 wt.% NaCl and 80 °C). .	149
Figure 102 XRD analysis after 4 days (in 2.5 ppm O ₂ (1 wt.% NaCl and 80 °C).....	149
Figure 103 Cross-section after 4 days in 2.5 ppm O ₂ (1 wt.% NaCl and 80 °C).....	150
Figure 104 Surface morphology at 6 different locations on the specimen after 10 days in 2.5 ppm O ₂ (1 wt.% NaCl and 80 °C).....	151
Figure 105 Composition analysis of the corrosion product by EDS after 10 days in 2.5 ppm O ₂ (1 wt.% NaCl and 80 °C).....	151
Figure 106 Cross-section after 10 days in 2.5 ppm O ₂ (1 wt.% NaCl and 80 °C).....	152
Figure 107 XRD analysis after 10 days in 2.5 ppm O ₂ (1 wt.% NaCl and 80 °C)	152
Figure 108 IFM 3D images of the corrosion product layer before layer removal after 10 days in 2.5 ppm O ₂ (1 wt.% NaCl and 80 °C)	153
Figure 109 IFM 3D images of the corrosion product layer after layer removal after 10 days in 2.5 ppm O ₂ (1 wt.% NaCl and 80 °C)	154
Figure 110 IFM images and analysis of the corrosion product layer after layer removal after 10 days in 2.5 ppm O ₂ (1 wt.% NaCl and 80 °C)	154
Figure 111 Change of measured bulk pH (red) and measured total ferrous and ferric ion concentration (green) with time, 1.4 ppm of oxygen was added after 6 days (1 wt.% NaCl and 80 °C)	156
Figure 112 Variation of corrosion rate and corrosion potential with test time as determined by LPR ,1.4 ppm of oxygen was added at 6 days (1 wt.% NaCl and 80 °C)	157
Figure 113 Surface morphology and cross-section after 4 days in 1 wt. % NaCl (80 °C, initial pH 6.6, initial [Fe ²⁺] 100ppm, and pCO ₂ 0.53 bar)	158
Figure 114 Surface morphology after 4 days in 1.4 ppm O ₂ (1 wt.% NaCl and 80°C)..	159
Figure 115 XRD analysis after 4 days in 1.4 ppm dissolved O ₂ (1 wt.% NaCl and 80 °C)	160
Figure 116 Cross-section after 4 days in 1.4 ppm dissolved O ₂ (1 wt.% NaCl and 80 °C)	160
Figure 117 Cross-section and EDS analysis after 4 days in 1.4 ppm dissolved O ₂ (1 wt.% NaCl and 80 °C).....	161
Figure 118 Surface morphology after 8 days in 1.4 ppm dissolved O ₂ (1 wt.% NaCl and 80 °C)	162

Figure 119 XRD analysis after 8 days in 1.4 ppm dissolved O ₂ (1 wt.% NaCl and 80 °C)	163
Figure 120 Cross-section after 8 days in 1.4 ppm dissolved O ₂ (1 wt.% NaCl and 80 °C)	163
Figure 121 IFM 3D images of the corrosion product layer before layer removal after 8 days in 1.4 ppm dissolved O ₂ (1 wt.% NaCl and 80 °C)	164
Figure 122 IFM 3D images of the corrosion product layer after layer removal after 8 days in 1.4 ppm dissolved O ₂ (1 wt.% NaCl and 80 °C)	165
Figure 123 IFM images and analysis of the corrosion product layer after layer removal after 8 days in 1.4 ppm dissolved O ₂ (1 wt.% NaCl and 80 °C)	165
Figure 124 Proposed tuberculation mechanism by Rosli in CO ₂ corrosion with O ₂ intrusion, taken from Roslin[74].....	168
Figure 125 Cross section diagram of a weight loss specimen	180
Figure 126 Cross section diagram of a weight loss specimen with a pitting	181
Figure 127 Mass change (left) and SFeCO ₃ (right) obtained on a polarized Au-coated quartz crystal with adding more NaCl (10 wt.%) at 80°C	186
Figure 128 Mass change (left) and the pH variation (right) on a polarized Au-coated quartz crystal with adding more NaCl (10 wt.%) at 80°C	187
Figure 129 Mass change (left) and SFeCO ₃ (right) obtained on a polarized Au-coated quartz crystal with adding more NaCl (15 wt.%) at 80°C	187
Figure 130 Mass change (left) and the pH variation (right) on a polarized Au-coated quartz crystal with adding more NaCl (15 wt.%) at 80°C	188
Figure 131 Mass change (left) and SFeCO ₃ (right) obtained on a polarized Au-coated quartz crystal with adding more NaCl (25 wt.%) at 80°C	188
Figure 132 Mass change (left) and the pH change variation (right) obtained on a polarized Au-coated quartz crystal with adding more NaCl (25 wt.%) at 80°C.....	189
Figure 133 Mass change (left) and SFeCO ₃ (right) obtained on a polarized Au-coated quartz crystal with adding more NaCl (20 wt.%) at 80°C	189
Figure 134 Mass change (left) and the pH variation (right) on a polarized Au-coated quartz crystal with adding more NaCl (20 wt.%) at 80°C	190

Chapter 1: Introduction

CO₂ corrosion is a significant issue for steel components in the oil and gas industry, for example, it may cause leakage in pipeline transmission systems, resulting in serious damage to the environment, risks to human life, and economic losses. Localized CO₂ corrosion is of particular research interest because it can cause a severe attack to oil and gas pipelines [1]. There are a variety of factors that could lead to or accelerate localized corrosion in CO₂ environments; major factors have been reported to include chloride ion concentration, temperature, anodic/cathodic polarization, organic acids, CO₂/H₂S partial pressures, total pressures, and flow rate [2] [3]. The dissertation research described herein focuses on evaluating and understanding the effects of chloride, oxygen, and acetic acid on CO₂ corrosion (or ‘sweet corrosion’[4]) from the perspective of localized attack.

1.1 CO₂ General Corrosion

CO₂ corrosion, often referred to as ‘sweet corrosion’, occurs when CO₂ dissolves in an aqueous solution that contacts a steel surface. CO₂ corrosion is an electrochemical process made of two half-cell reactions: anodic and cathodic reactions [2]. The anodic reaction is oxidative iron dissolution, in which iron oxidizes to ferrous ions:

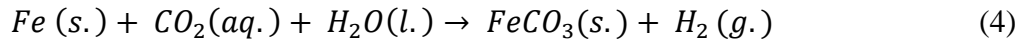


Two cathodic reactions are reported to happen, hydrogen evolution and the reduction of carbonic acid (recent research has reported the former to be overwhelmingly dominant [5] [6]):

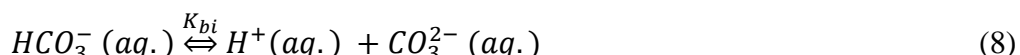
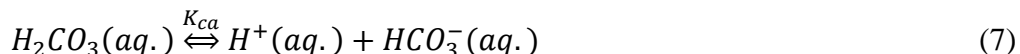
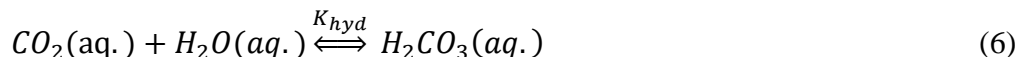
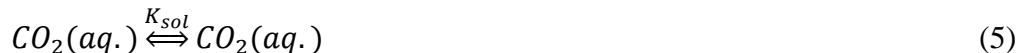




The overall reaction is shown below:



Besides these oxidation-reduction reactions, other chemical reactions that occur in the system are [4]:



Reactions (5) – (8) are used for water chemistry calculations. CO₂ dissolves in the aqueous solution, as shown in reaction (5). A small amount of the dissolved CO₂ hydrates to form carbonic acid, as shown in reaction (6). According to reactions (7) and (8), some of the generated carbonic acid and resultant bicarbonate ions dissociate.



According to reaction (9), when the product of the ferrous and carbonate ions concentration becomes larger than the equilibrium constant of FeCO₃, $K_{sp(FeCO_3)}$, solid FeCO₃ will precipitate [4]; this could occur homogeneously to produce a uniform product layer on the steel surface. If the FeCO₃ layer is compact and covers the metal surface completely, the layer can act as a diffusion barrier and blocks/covers the steel surface making it unavailable for corrosion, and, therefore, the metal would become resistant to

further corrosion in the CO₂ environment. However, if the FeCO₃ layer is porous or damaged, it will not be protective, and the corrosion rate of the steel will remain high.

Significant achievements have been made regarding understanding CO₂ general corrosion of carbon steel. Consequently, several models have been developed to facilitate prediction of its likelihood and magnitude. The models can be divided into two categories: empirical/semi-empirical and mechanistic [7].

The most popular empirical/semi-empirical model was initially developed by de Waard and Milliams [8]. In 1975, based on the experimental data, a simple model was constructed to predict the relationship between corrosion rate and pH, temperature, and CO₂ partial pressure [8]. Over the next two decades, the authors developed the model further and more effects were incorporated [9] [10].

Gray, *et al.* [11] developed an electrochemical model for CO₂ corrosion which can be applied for pH 2-11 and temperatures 25°C-125°C; corrosion rate being calculable as a function of pH and temperature. Nesic, *et al.* [2], [12]–[14] further developed this mechanistic model by incorporating chemical reactions, electrochemical reactions and transport phenomena. Nesic's model is the most comprehensive model for CO₂ general corrosion thus far developed. The models have been proven to accurately model the corrosion mechanisms within the scope of temperatures from 1°C to 120°C, pH from 3 to 7, and pipe diameter from 0.01m to 1m, liquid velocity from 0.001 to 20m/s [15].

Kahyarian, *et al.* [16] wrote a comprehensive summary of all the existing models for CO₂ general corrosion. They considered the understanding of uniform CO₂ corrosion

is a mature topic. However, modeling of localized CO₂ corrosion still has a long way to go.

1.2 CO₂ Localized Corrosion

Compared to general corrosion, less progress has been achieved in understanding localized CO₂ corrosion. Localized corrosion is more complicated to detect and predict than general corrosion. Once the mechanism of localized CO₂ corrosion is established, it will help in the development of targeted, cost effective mitigation strategies in the oil and gas industry; this has major economic and, indirectly, environmental benefits. Therefore, it is necessary to study localized CO₂ corrosion.

Localized corrosion can be divided into three stages: initiation which involves protective layer formation, layer breakdown and layer penetration; early pit growth; and propagation [17]. Since there is not always a clear boundary between early pit growth and propagation, localized corrosion is also considered to have two stages: initiation and propagation [17]. Three theories of passive layer breakdown were proposed [18]: penetration of passive layer [19], layer breaking [20], and adsorption of chloride ions [21].

It is noteworthy that the localized corrosion mechanisms described in the above literature are related to stainless steel or nickel-based alloys, which can be passivated to form a very thin protective layer. It is this layer that can be broken-down and cause localized corrosion. Han, *et al.*'s [22] results indicated that a trace amount of iron oxide was detected by GIXRD (grazing incidence X-ray diffraction) and by TEM-EDS in CO₂ saturated 1 wt.% NaCl electrolyte at 80°C and pH 8 on carbon steel. W. Li [23]

investigated the pseudo-passive layer formation in CO₂ corrosion on carbon steel. His study covered the range pH from 5.6 to 7.8 at 80°C and it was claimed that a pseudo-passive layer formed underneath the FeCO₃ layer at pH higher than 6 from a positive open circuit potential shift and a significantly reduced corrosion rate. Based on those experimental results, H. Li [24] proposed a CO₂ localized model on carbon steel which depicts three processes: pseudo-passivation /repassivation, pit initiation and pit propagation. The model postulates that a pseudo-passive layer formed due to a high pH underneath the protective FeCO₃ and, at some point, a small area of the FeCO₃ layer is dissolved or damaged, causing the passive layer to become compromised and then this small area of steel is exposed. Thus, a galvanic cell forms with the small layer-free area anode and the large coverage area as a cathode. Propagation of CO₂ localized corrosion has been previously studied by other researchers. Han developed an artificial pit cell, in which the current produced from localized corrosion propagation was monitored. In his research, several electrochemical models, including the active corrosion model, the spontaneous passivation model, localized galvanic cell model, and water chemistry model, were used to study propagation of CO₂ localized corrosion. This research is focused on the initiation of CO₂ localized corrosion and, therefore, propagation will not be within this dissertation's scope.

Under certain conditions (high temperature, high pH, and high supersaturation of FeCO₃), a protective iron carbonate layer can be formed on carbon steel [23], [25]–[27]. Based on previous studies [28] [29] [30], it has been reported that CO₂ localized

corrosion could initiate where the partially protective FeCO_3 layer on the metal surface is removed under certain extreme conditions.

Nyborg and Dugstad [31] proposed that a typical temperature range for localized corrosion initiation and propagation is 60°C-90°C. This temperature range is often seen in the field where the fluids being transported via mild steel pipelines enter the line at a temperature around 100°C or even higher and cool down to the environmental conditions.

Ruzic [7] proposed three mechanisms of protective layer removal in his work, namely, chemical, mechanical, and combination of chemical and mechanical mechanisms. Once the protective corrosion product layer was removed, the steel would be exposed to the environment without any protection. These exposed areas have lower corrosion potential compared to the areas that are still covered with the iron carbonate layer; therefore, the bare steel area would behave as the anode which loses electrons according to equation(1), and the protective area would behave as the cathode which consumes electrons according to several reactions in equation (2) and (3). The formation of a galvanic corrosion cell is a postulated mechanism for localized corrosion [30].

Yang, *et al.* conducted experiments to test a hypothesized mechanical removal mechanism by wall shear stress from fluid flow. The results show that the FeCO_3 layer cannot be removed under the studied flow conditions (1.3 m/s and 10.6 m/s) because the wall shear stress created by the jet fluid flow is much smaller than the adhesion strength of the layer on its steel substrate [7], [25].

Therefore, the focus of this research will be on evaluation of chemical influences, including chlorides, oxygen, and acetic acid, on localized corrosion. A key aspect of this

work is to investigate whether these species can help dissolve the FeCO₃ layer, either by chemical reactions or through changes in the ionic strength that affect equilibria relating to FeCO₃ formation/persistence.

1.2.1 Chloride Effect

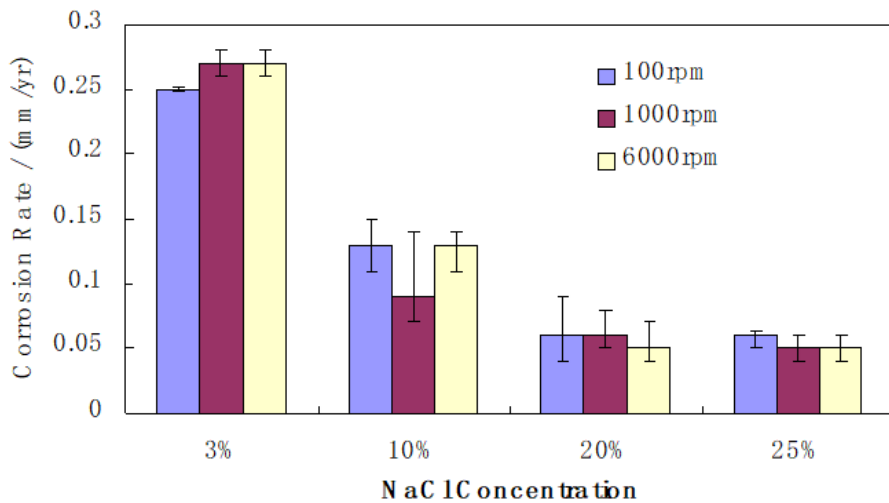
Chloride ion (Cl⁻) has long been reported to be aggressive to steel and cause corrosion. In much research, it has been concluded that localized corrosion, especially pitting, was related to chlorides.

Liu, *et al.* [32] studied the effect of chloride on CO₂ corrosion of carbon steel and determined that Cl⁻ does not alter the composition of the corrosion product but impacts its morphology.

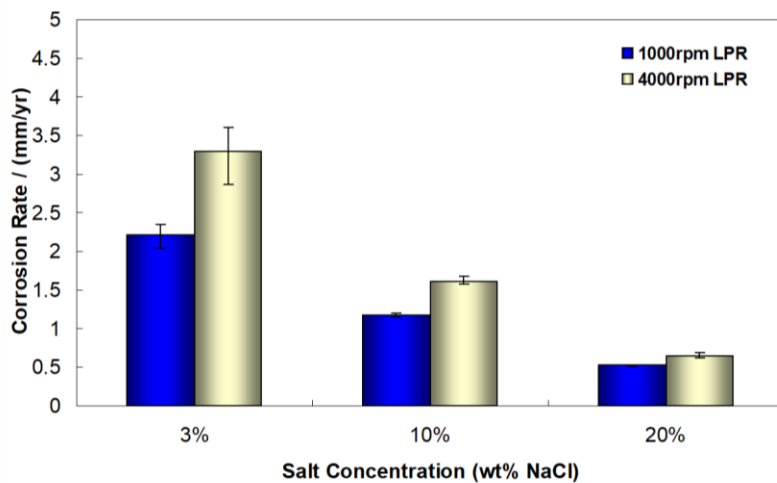
Fang[33], conducted short-term experiments with a high concentration of chloride (10 and 20 wt.%) at different temperatures (1°C-20°C). FeCO₃ formation was not observed under these conditions due to the very low saturation of iron carbonate, which suggested lack of localized corrosion. Some of his results are reproduced in Figure 1 and Figure 2. It was found that general corrosion rate decreased with the increase in NaCl concentration (from 3 wt.% to 25 wt.%) for both tested temperatures (5°C and 20°C). Overall, his research found that heterogeneous charge transfer reactions, homogeneous chemical reactions, and mass transfer reactions were all retarded by the increase in NaCl concentration [33].

Figure 1

Comparison of LPR corrosion rates measured at 5°C, pH 4.0 at 100 rpm (revolutions per minitue), 1000 rpm and 6000 rpm. Taken from Fang [33]

**Figure 2**

Salt effect on LPR corrosion rate in CO₂ sparged solutions (1000, 4000 rpm, pH 4, 20°C). Taken from Fang [33]



Schmitt and Feinen [34] proposed that, at low concentrations (the order of 10^{-4} M), chloride ions act as an inhibitor and bicarbonate ions are the main reason for CO₂ localized corrosion; at higher concentrations, they postulated that chloride ions help transfer negative charges to anodic sites, which affects localized corrosion.

Ma [35] [36] studied the precipitation kinetics of FeCO₃ from 1 wt.% NaCl to 9 wt.% NaCl at 80°C and 60°C and 0.53 bar CO₂. The results indicated that in 1 wt.% NaCl electrolyte, the predicted precipitation rate of FeCO₃ (PR_{FeCO_3}) was in a good agreement with the experimental precipitation rate. However, with the increase of the NaCl concentration, the predicted precipitation rate deviated from the experimental values. It was postulated that the most possible reason to cause the deviation was the solubility of FeCO₃, which is dependent on ionic strength at a fixed temperature.

Chloride concentration can indirectly affect CO₂ solubility. With the increase of ionic strength, CO₂ solubility decreases. In a paper by Madani Sani [37], three different models were reviewed regarding the effect of salinity on CO₂ solubility: the Oddo-Tomson model, Duan-Sun model, and Duan-Zhao model. The Oddo-Tomson model [38] uses ionic strength (ionic strength is mainly calculated by sodium chloride concentration) in the equations. Both the Duan-Sun model [39] and Zhao-Lvov [40] model use activity coefficients in their equations, they differ in that different empirical equations are used.

Sun [41] studied localized CO₂ corrosion on carbon steel in wet gas flow in Cl⁻ free and Cl⁻ containing (0.1 wt.% NaCl and 1 wt.% NaCl) electrolyte at 90°C, reporting localized corrosion in Cl⁻ free and Cl⁻ containing environments. It is noteworthy that the occurrence of localized corrosion is when saturation of FeCO₃ is between 1 and 3.

So far, it remains unclear how chloride initiates localized corrosion. Parameters relating to why, and how, FeCO_3 layers dissolve are unknown. Therefore, experiments will be conducted to study the chloride effect.

1.2.2 Oxygen Effect

Oxygen (O_2) is a strong oxidant, reacting with metals even when present in trace concentrations in a system. Therefore, in the oil and gas industry, its concentration is controlled to be as low as practically achievable. Oxygen is often found in wells or pipelines due to fluid injection, ingress through well annuli, or *via* faulty seals of pumps [42]. Since it is almost unavoidable, it is important to understand how oxygen affects corrosion in CO_2 environments.

It has been reported that oxygen ingress increases the corrosion rate of mild steel in both CO_2 and H_2S systems. In work reported by Jiang [43], after ingress of 1 ppm oxygen, the iron carbonate was not protective anymore and the general corrosion rate increased but no localized corrosion was found. Sherar, *et al.*[44], reported that introduction of a small amount of O_2 may initiate a transition in observed corrosion phenomena; the overall corrosion rate increased by a factor of four to five times and the properties of the corrosion product changed to ferric oxide type, as indicated by EIS and Raman spectroscopy analyses.

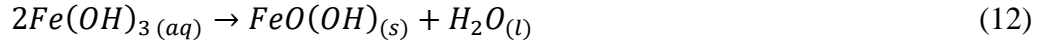
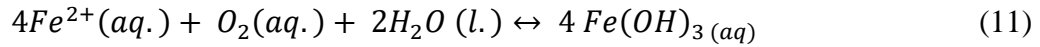
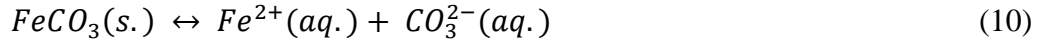
Wang [45] conducted a series of experiments for oxygen effect on CO_2 corrosion from 0 ppb to 3 ppm O_2 at 25°C and 1 bar total pressure. The results indicate that limiting current is affected by increasing O_2 concentration. When O_2 concentration was below 100 ppb, the dominant CO_2 corrosion is under control of charge transfer and only general

corrosion was observed. When O₂ concentration increased to 1 ppm and 3 ppm, CO₂ corrosion was not the dominant corrosion and the corrosion mechanism was under the control of mixed charge transfer and mass transfer. Pits were observed in high O₂ concentration conditions but did not propagate further.

Martin [42] studied the corrosion consequence of oxygen entry of carbon steel in CO₂ corrosion and H₂S corrosion system with and without inhibition at 90 °F (32°C). The results indicated that corrosion rate was increased in both sweet and sour corrosion when O₂ is present. Although O₂ is a stronger oxidant than carbon dioxide, oxygen was not selectively consumed, and the dissolved CO₂ still predominantly controlled the cathodic reaction. Therefore, iron carbonate should be still the main corrosion product. The results from Rosli's experiment at 80°C with CO₂/O₂ sparged indicated that the surface of carbon steel was mainly covered by iron carbonate. Martin's experiment had no particles observed in the CO₂/O₂ system. The effectiveness of all corrosion inhibitors used in Martin's research was found to be weakened to varying degrees by oxygen ingress. Song, *et al.* [46] did two types of experiments, at a given CO₂ partial pressure (0.2 atm) with changes in O₂ partial pressure and a given O₂ partial pressure (0.2 atm) with changes in CO₂ partial pressure. They found that the corrosion rate increased with the increase of O₂ partial pressure for a fixed CO₂ partial pressure. For a fixed O₂ partial pressure, the corrosion rate is controlled by O₂ diffusion, or charge transfer, or both, depending on the boundary layer thickness.

However, how oxygen reacts with the iron carbonate in such systems and how the breakdown of the iron carbonate layer can develop localized corrosion requires further

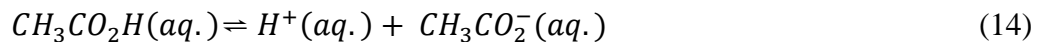
investigation. It is hypothesized that Fe^{2+} in FeCO_3 will be oxidized by dissolved oxygen to form Fe^{3+} [44], as depicted in the equations shown below:



The solution should have a reddish orange solid precipitate due to formation of ferric oxides.

1.2.3 Acetic Acid Effect

As the most prevalent organic acid found in oilfield environments, acetic acid (CH_3COOH or HAc) is reported to play an important role in CO_2 corrosion of mild steel. Acetic acid of pK_a 4.76 is a weak acid but it is still stronger than carbonic acid which has a pK_a 6.35 at 25°C [47]. When the CO_2 partial pressure is in the range of 0.1 bar to 1 bar and the concentration of HAc is between 0.1 to 1 mM, acetic acid has the potential to be the main source for supplying reducible hydrogen ions when it exists in aqueous CO_2 systems [48]; its dissociation reaction is shown in the following reaction:



Studies of the role of acetic acid in CO_2 corrosion have reported different phenomena occurring during the corrosion process. In research reported by Amri, *et al.* acetic acid caused an increase of E_{corr} (corrosion potential), which worked as a driving force to induce and propagate localized CO_2 corrosion [49]. Fajardo [50] conducted a series of experiments relating to the effect of acetic acid on iron carbonate corrosion

product layers, reporting that at 80°C and pH 6.3 undissociated acetic acid was observed to cause localized damage to FeCO₃ layers. Pletcher, *et al.* [51] compared the corrosion of carbon steel and 13Cr steels in environments with acetate and found that the corrosion rate of carbon steel increased when acetic acid was added but the corrosion rate of 13Cr steel remained low in the brine solution containing acetate. This would have been a better study if the solution pH would have been reported.

Crolet, *et al.* [48] reported that “acetic species actually act as a weak inhibitor of the anodic dissolution reaction”, this has the potential to interrupt localized corrosion. Amri [52] proposed that acetic acid molecules could selectively adsorb onto different regions of a metal surface; this causes a significant pH difference between anodic and cathodic sites, which could lead to an active potential gradient, inducing localized attack. These two mechanisms remain controversial. More investigation is needed to make it clear.

Chapter 2: Research Objectives

The objective of the research reported in this dissertation is to investigate the initiation mechanism of CO₂ localized corrosion of mild steel. To achieve this, it is necessary to state the following goals and associated hypotheses:

- Investigate the conditions leading to localized corrosion initiation in a CO₂ environment, with a concurrent focus on any effect associated with the presence of chlorides.
 - Hypothesis 1: Adding chlorides is a cause of localized corrosion initiation.
 - Hypothesis 2: Initiation of localized CO₂ corrosion can be caused by changing the solubility of iron carbonate through changes in the ionic strength of the solution.
- Validate the water chemistry calculations derived from the Oddo & Tomson model for a range of ionic strength (corresponding to NaCl concentrations from 0 to 25 wt.%) and range of temperatures (from 30 °C to 80 °C).
- Study the equilibrium of FeCO₃ dissolution and precipitation in non-ideal solutions by the electrochemical quartz crystal microbalance (EQCM).
- Study whether acetic acid causes localized FeCO₃ damage or works as a weak inhibitor.

- Hypothesis: Localized corrosion can be initiated with addition of acetic acid because the addition of acetic acid as a buffer solution increases the solution ionic strength.
- Investigate the effect of O₂ “intrusion” on iron carbonate corrosion product layer formation and degradation in CO₂ corrosion.
 - Hypothesis: Iron carbonate is partially dissolved by the ingress of O₂ and then localized corrosion is initiated.

Chapter 3: General CO₂ Corrosion in Non-Ideal Solutions

3.1 Introduction

Since 2003, the mechanistic model published by Nordsveen, *et al.*[53], has been used for water chemistry and electrochemical calculations associated with CO₂ corrosion. This model covers chemical, electrochemical and transport processes, drawing from Oddo and Tomson's 1982 paper [38], specifically the reported equilibrium reactions between water and CO₂ species therein, as well as utilizing the water dissociation constant published by Kharaka, *et al.* [54] and the hydration constant reported by Palmer and van Eldik [55] to complete calculations. ICMT's FREECORP™ software, released in 2008, is based on this model and works well for ideal solutions.

A review of research work associated with the above literature has illuminated shortcomings in calculations related to higher ionic strengths at various temperatures. In Madani Sani's research [37], experimental measurements coupled with calculations from activity-based water chemistry models (Li & Duan [56] and Harvie [57] models) are used in his review and data analysis. It is noteworthy that with increasing salt concentration, deviations between measured pH value and predicted pH value by the more simplified Oddo and Tomson Model became more and more significant. A study by Fang showed a similar result [33].

There is considerable complexity associated with the use of activity-based water chemistry models, so calculations related to CO₂ corrosion mechanisms often use the ideal solution equations of Oddo & Tomson without understanding the involved inherent

error. Therefore, the mechanistic model based on Oddo & Tomson's equations will be reviewed and modified, as necessary, to improve this limitation.

3.2 Water Chemistry

As mentioned in section 1.1, water chemistry can be determined using reactions (5) – (8). The following text shows all the equations used to calculate speciation associated with CO₂ corrosion water chemistry.

CO₂ is dissolved into water according to reaction (5) in section 1.1.

The bulk aqueous concentration of CO₂ can be calculated from:

$$c_{CO_2(aq)} = K_{sol} \times P_{CO_2} \quad (15)$$

Where the Henry's constant (K_{sol}) can be obtained from equation(16) for ideal solutions [58] and from equation (17) for non-ideal solutions [38]:

$$K_{sol} = 0.0454 \times (1.6616 - 5.736 \times 10^{-2}T_c + 1.031 \times 10^{-3}T_c^2 - 9.68 \times 10^{-6}T_c^3 + 4.471 \times 10^{-8}T_c^4 - 7.912 \times 10^{-11}T_c^5) \quad (16)$$

$$K_{sol} = 14.46 \times 10^{-(2.27 + 5.65 \times 10^{-3}T_f - 8.06 \times 10^{-6}T_f^2 + 0.075 \times I)} \quad (17)$$

Ionic strength, I , which can be calculated from equation (18), relates to salt concentration:

$$I = \frac{1}{2} \sum_i c_i z_i^2 \quad (18)$$

H₂CO₃ can form as the dissolved CO₂ reacts with H₂O [4] refers to reaction (6) in section 1.1. The equilibrium constant of H₂CO₃ is given in Equation (19).

$$K_{hyd} = \frac{c_{H_2CO_3}}{c_{CO_2}} \quad (19)$$

K_{hyd} , the equilibrium constant for the CO₂ hydration reaction, is 2.58×10^{-3} ; is treated as being the same value over the temperature range of 20-100°C[55].

Carbonic acid can dissociate into H⁺ and HCO₃⁻ according to reaction (7) in section 1.1. The equilibrium constant K_{ca} can be calculated from equation (20).

According to reaction (8) in section 1.1, HCO₃⁻ further dissociates into H⁺ and carbonate ion, CO₃²⁻. The equilibrium constant K_{bi} can be calculated from equation (21).

$$K_{ca} = \frac{c_H^+ c_{HCO_3^-}}{c_{H_2CO_3}} \quad (20)$$

$$K_{bi} = \frac{c_H^+ c_{CO_3^{2-}}}{c_{HCO_3^-}} \quad (21)$$

The equilibrium constants for dissociation of H₂CO₃ and HCO₃⁻ can be obtained from Oddo & Tomson's equations as shown below [38]:

$$K_{ca} = 387.6 \times 10^{-(6.41 - 1.594 \times 10^{-3}T_f + 8.52 \times 10^{-6}T_f^2 - 3.07 \times 10^{-5}p \times 14.7 - 0.4772I^{0.5} + 0.118I)} \quad (22)$$

$$K_{bi} = 10^{-(10.61 - 4.97 \times 10^{-3}T_f + 1.33 \times 10^{-5}T_f^2 - 2.624 \times 10^{-5}p \times 14.7 - 1.166I^{0.5} + 0.3466I)} \quad (23)$$

In this dissertation, K_x is also displayed as pK_x :

$$pK_x = -\log(K_x) \quad (24)$$

An equation to deal with the electroneutrality of the solution is needed:

$$c_{H^+} + c_{Na^+} = c_{HCO_3^-} + 2c_{CO_3^{2-}} + c_{Cl^-} + c_{OH^-} \quad (25)$$

If there are any other ions that exist in the system, the equation (25) is rewritten as:

$$c_{H^+} + c_{Na^+} + mc_{A^{m+}} = c_{HCO_3^-} + 2c_{CO_3^{2-}} + c_{Cl^-} + c_{OH^-} + nc_{C^{n-}} \quad (26)$$

where $c_{A^{m+}}$ denotes other anions and $c_{C^{n-}}$ denotes other cations.

The bulk solution pH and concentrations of all the aqueous species can be calculated from the above equations. The bulk solution pH can also be measured by a pH meter.

3.3 pH Measurement

In this work, an Oakton pH 150 meter (WD-35614-32) with a Cole-Parmer pH electrode (#UX-05991-81) was used to measure the solution pH. The pH probe offers resistance to Na^+ ion interference [59].

In order to get valid values, the pH was calibrated by a 3-point calibration method at the beginning of every experiment. At each temperature, crystalline NaCl was added into the solution gradually. Table 1 lists the mass of NaCl needed for different salt concentrations. For each salt concentration, pH was measured every 30 minutes. When the pH was stable (± 0.01 pH unit change), more salt was added into the system.

Table 1

Weight of NaCl added for different salt concentrations

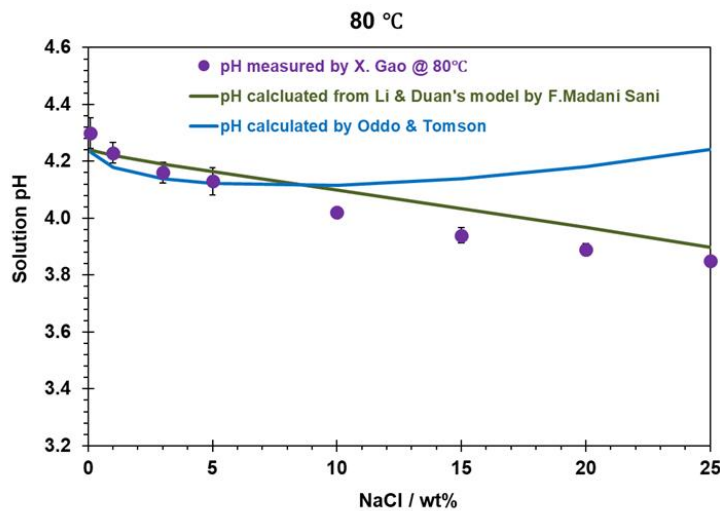
[NaCl] / wt.%	Total crystalline NaCl / g	Additional NaCl / g
1	20.20	
3	61.86	41.66
5	105.26	43.40
10	222.22	116.96
15	352.94	130.72
20	500.00	147.06
25	666.67	166.67

3.4 Does the Expected pH from the Model Match the Measured pH?

The pH comparisons are shown in Figure 3, Figure 4 and Figure 5 for 80°C, 50°C, and 30°C, respectively. In Figure 3, the purple dots signify pH measured at 80 °C. The blue line shows the pH predicted from Oddo & Tomson's model. The green line displays the pH calculated from Li & Duan's model by F. Madani Sani. Li & Duan's model was based on Pitzer's equation, relating to activity coefficients [56]. From 0.1 wt.% to 5 wt.% NaCl, both Oddo & Tomson's and Li & Duan's model outputs are similar to the experimentally measured values. However, with the increase of NaCl concentration, Oddo & Tomson's model has a large deviation from the measured pH, while output from Li & Duan's model is much closer to the measured values. The same observation can be made in terms of comparisons at 50 °C and 30°C. Therefore, the currently used water chemistry model needs to be revised.

Figure 3

The predicted and measured pH vs. NaCl concentrations at 80°C

**Figure 4**

The predicted and measured pH vs. NaCl concentrations at 50°C

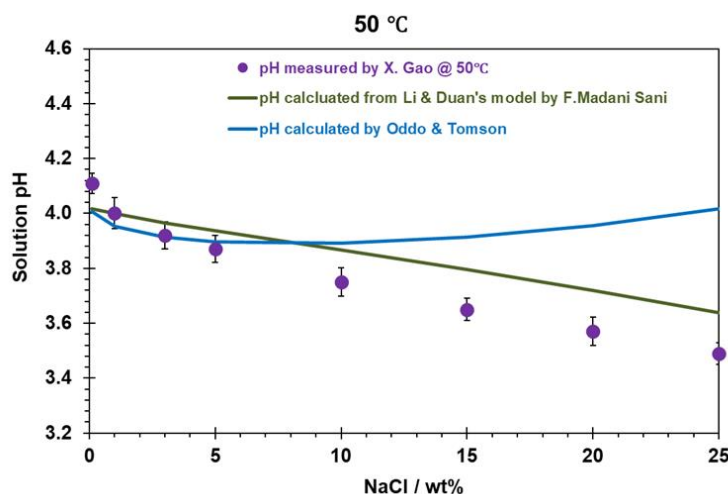
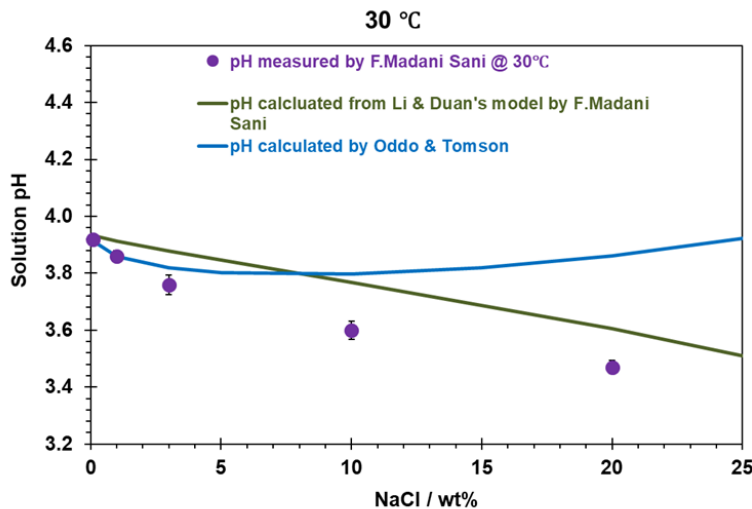


Figure 5

The predicted and measured pH vs. NaCl concentrations at 30°C



3.5 Revision of the Current Water Chemistry Model

Among the four equilibrium constants of K_{sol} , K_{hyd} , K_{ca} and K_{bi} , the hydration constant, K_{hyd} , is treated as not changing with ionic strength. Therefore, there is no need to revise K_{hyd} . However, it is impossible to revise all the other three constants of K_{sol} , K_{ca} and K_{bi} at the same time. Therefore, each of these three constants have to be individually checked.

Trends in CO₂ solubility in aqueous NaCl with increasing ionic strength calculated by the K_{sol} equation are shown in Figure 6 and Figure 7 for 25°C and 50°C, respectively. There is less than 15% error between [CO₂]_(aq.) predicted by Oddo & Tomson's model and the experimental data reported by Markham & Kobe[60] at 25°C. In addition, the difference between [CO₂]_(aq.) predicted by Li & Duan's model and the

experimental data is also less than 11%. At 50°C and 80°C, no experimental data was found but there is less than 7% error between the two models. Therefore, it is considered that $[CO_2]_{(aq.)}$ predicted by the Oddo & Tomson model matches the $[CO_2]_{(aq.)}$ predicted by Li & Duan's model, as shown in Figure 7 and Figure 8. Therefore, there is no need to modify K_{sol} .

Figure 6

CO₂ solubility in NaCl solution (Oddo & Tomson's model and Li & Duan's model (calculated by F. Madani Sani) vs. experimental data from ref. [60] at 25°C)

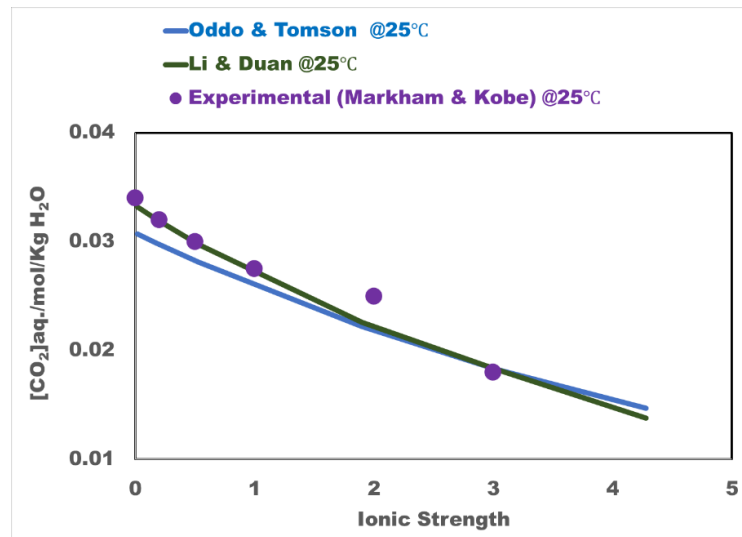
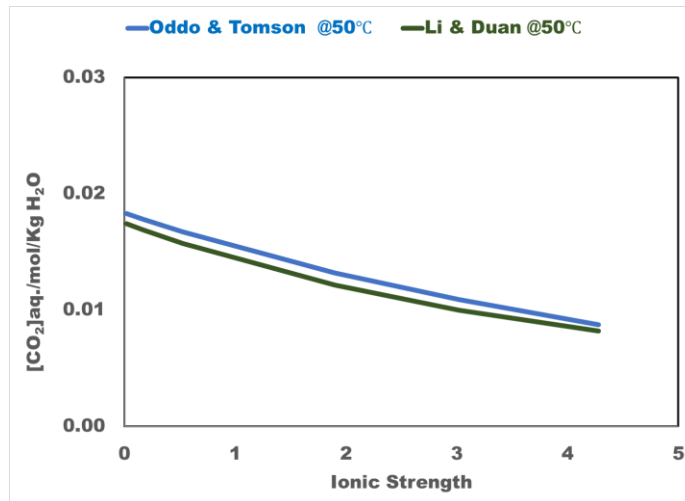
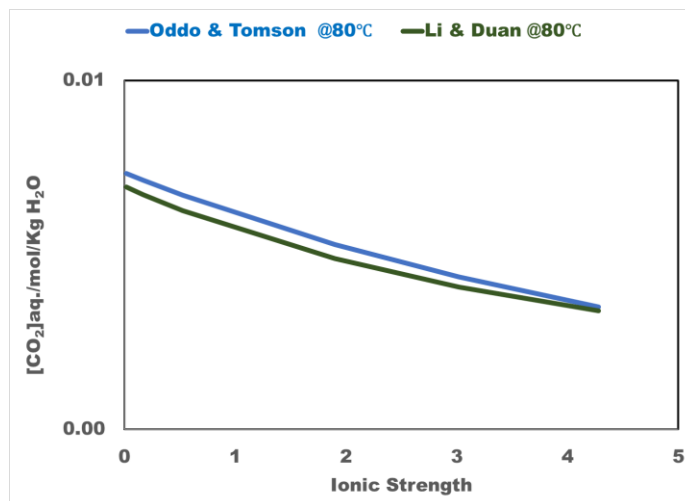


Figure 7

CO_2 solubility in $NaCl$ solution- the prediction of Oddo & Tomson's model vs. Li & Duan's model (calculated by F. Madani Sani) at $50^\circ C$

**Figure 8**

CO_2 solubility in $NaCl$ solution - the prediction of Oddo & Tomson's model vs. Li & Duan's model (calculated by F. Madani Sani) at $80^\circ C$



The hydration constant, K_{hyd} , is defined as 2.58e-3 [55], which is independent of ionic strength.

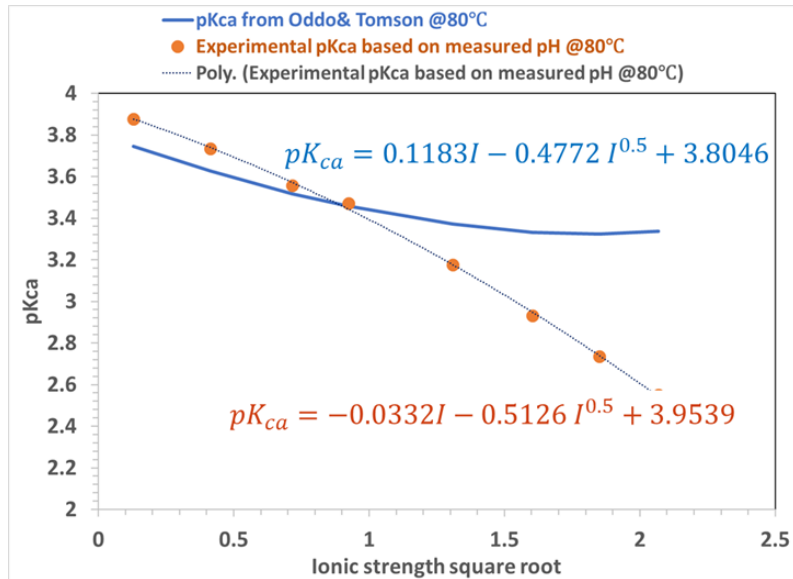
The ratio of $[HCO_3^-]$ formed by carbonic acid dissociation to $[CO_3^{2-}]$ formed by dissociation of bicarbonate is approximately 1e+5 at temperatures from 30°C to 80°C and for $[NaCl]$ from 0.1 wt.% to 25 wt. %. The ratio of $[HCO_3^-]/[CO_3^{2-}]$ reflects that there is a negligible amount of $[H^+]$ produced to $[H^+]$ produced by carbonic acid dissociation. Therefore, the pH is mainly affected by carbonic acid dissociation. There is no value in modifying K_{bi} .

Consequently, K_{ca} , the carbonic acid dissociation constant, is the one which requires modification. The best fit line for the K_{ca} equation at 80°C is shown in Figure 9. The blue line with the blue equation (the same as equation (22)) is the calculated pK_{ca} based on Oddo & Tomson's equation. The orange dots are calculated pK_{ca} values based on experimental pH. The black dotted line with the orange equation is a fitting line. By using the newly fit line, the new K_{ca} equation is as follows:

$$pK_{ca} = -(6.41 - 1.4 \times 10^{-3}T_f + 8.52 \times 10^{-6}T_f^2 - 3.07 \times 10^{-5}p - 0.5126I^{0.5} - 0.0332I) \quad (27)$$

Figure 9

The best fit line (the black dot-line and the orange equation) for the K_{ca} equation

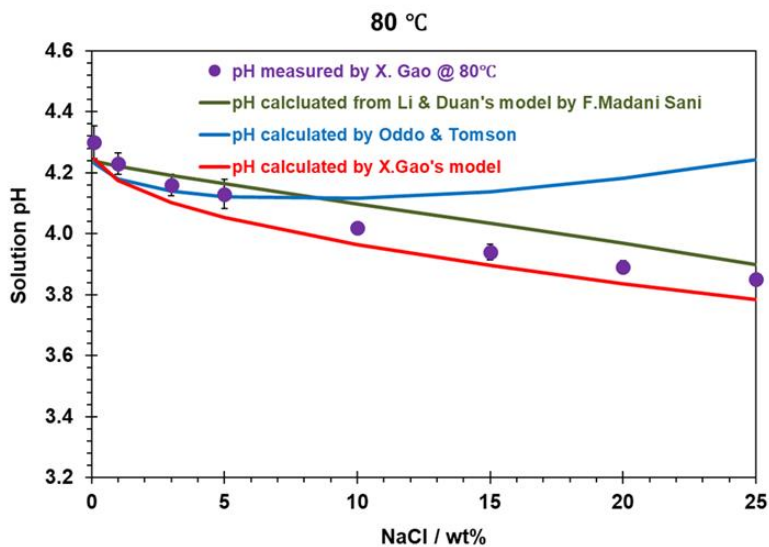


3.6 Validation of the New Model

After the K_{ca} equation was modified, the measured and the predicted pH changes with NaCl concentration at 80°C, 50°C and 30°C are shown in Figure 10, Figure 11 and Figure 12, respectively. Although at 80°C, both Li & Duan model and the current model (red lines) have a less than 2% error from the measured data, the error for the Li & Duan model at 30°C increases to almost 5% while the current model is still much less than 2%.

Figure 10

The predicted and measured pH vs. NaCl concentrations at 80°C

**Figure 11**

The predicted and measured pH vs. NaCl concentrations at 50°C

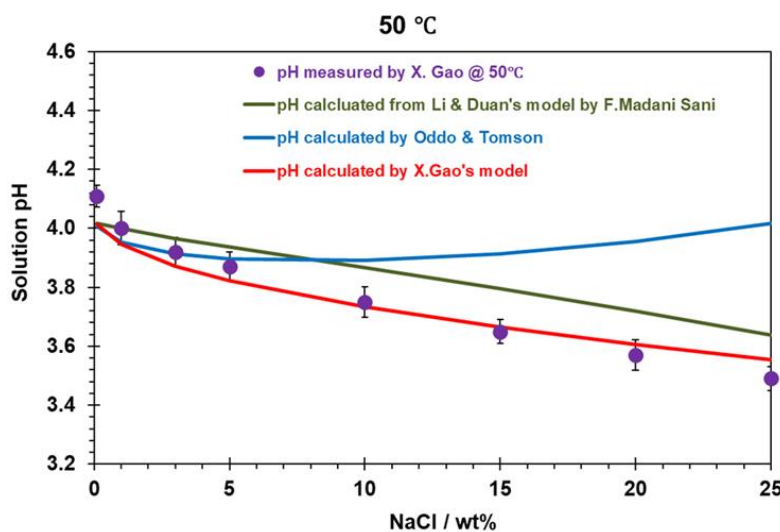
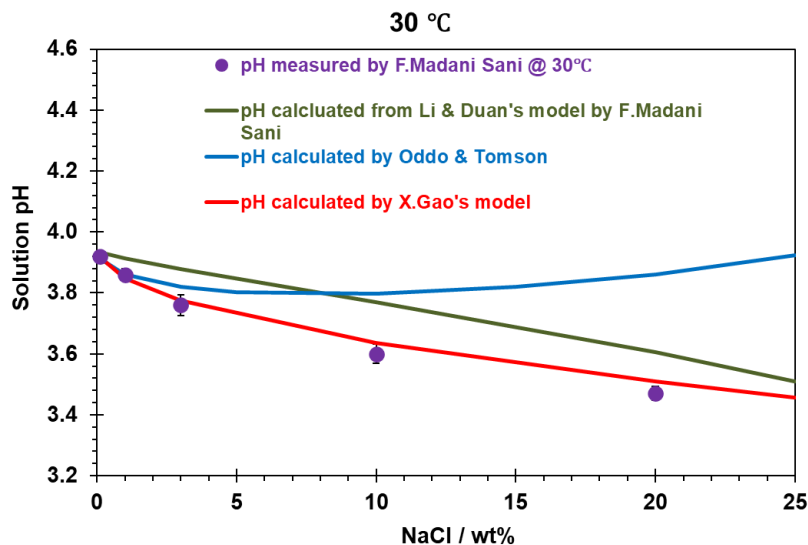


Figure 12

The predicted and measured pH vs. NaCl concentrations at 30°C



3.7 Summary

Predicted pH values by the new proposed model are in better agreement with measured values over the temperature range from 30°C to 80°C and with changes in ionic strength from 1 wt.% to 25 wt.% aqueous NaCl solution.

Chapter 4: Effect of Chloride on Initiation of CO₂ Localized Corrosion of Carbon Steel

4.1 Introduction

In the oil and gas industry, high concentrations of aqueous chlorides are often found where localized corrosion occurred [2] [3] [4]. Therefore, most researchers believe that chlorides are the cause of localized corrosion. However, it is still unknown exactly how or if chlorides initiate localized corrosion in CO₂ environments.

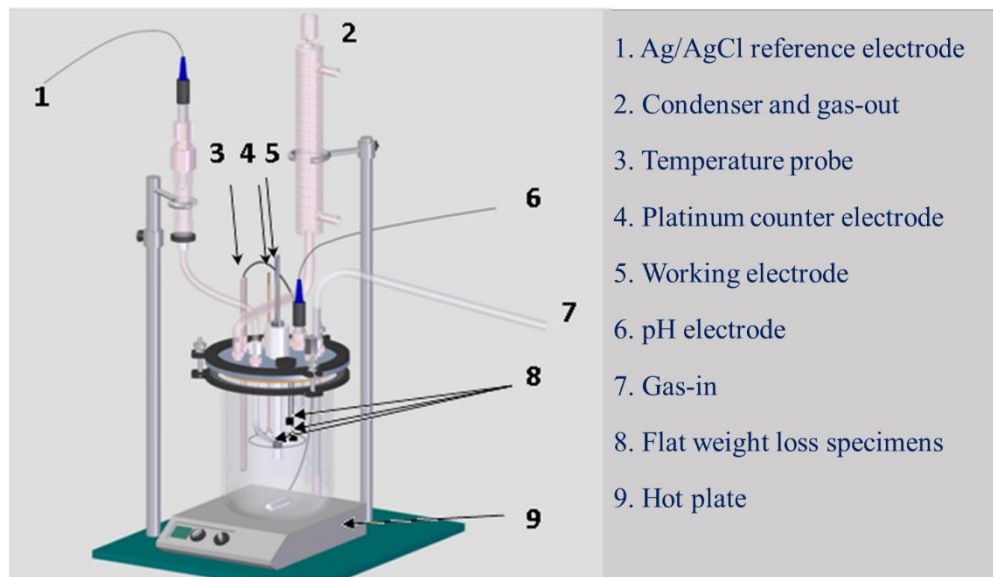
4.2 Hypotheses

- Hypothesis 1: Adding chlorides is a cause of localized corrosion initiation.
- Hypothesis 2: Initiation of localized CO₂ corrosion can be caused by changing the solubility of iron carbonate through changes in the ionic strength of the solution.

4.3 Experimental Method

4.3.1 Experimental Setup

A 2-liter glass cell and 3-electrode system was used as shown in Figure 13. In each test, six X65 mild steel specimens were exposed to NaCl or NaClO₄ electrolytes and were removed periodically for analysis.

Figure 13*Glass cell setup*

4.3.2 Experimental Procedure

The test matrix for experiments conducted in NaCl electrolytes is shown in Table 3, the matrix for tests in aqueous NaClO₄ solutions is shown in Table 4. Prior to each experiment, the solution was sparged with CO₂ to facilitate deoxygenation and ensure saturation, the temperature was set, and then the solution pH was adjusted using 1 M NaHCO₃. The specimens were polished with 150, 400 and 600 grit abrasive paper, rinsed with isopropanol, and then dried by a cool air blower before insertion into the glass cell. LPR (linear polarization resistance), measured using a Gamry Reference 600 potentiostat, was used to determine general corrosion rate every one to two hours during the test. A Thermo Scientific GENESYS 10vis Spectrophotometer was used to measure Fe²⁺ concentration from a 10ml aqueous sample daily (the detailed procedure refers to

Appendix I Procedure of Iron Ion Measurement). Scanning electron microscopy (SEM) and profilometry by Infinite Focus Microscopy (IFM) were used to analyze the corrosion product layer, as well as layer-free corroded specimens, and X-ray diffraction (XRD) was used to determine corrosion product composition.

In this dissertation, four types of specimens were used. The details are shown in Table 2.

Table 2

Types of specimens used in this dissertation

Types of Specimens	Schematic	Effective working area / cm ²	Application
Electrochemical specimens		1.0	LPR
Cylinder specimen		5.4	LPR
Flat weight loss specimen		1.0	SEM, cross-section, XRD, IFM, weight loss
Iron-coated or gold-coated quartz crystal		1.37	EQCM, SEM

Table 3

Test matrix for experiments in NaCl electrolyte

	Test 1		Test 2		Test 3		Test 4	
NaCl (wt.%)	0.1	1	0.1	3	1	10	1	15
Days	2.5	13.5	2	21	3	6	1.5	12.5
Temperature (°C)	80		80		80		80	
pH (initial)	6.6		6.6		6.6		6.6	
CO ₂ partial pressure (bar)	0.53		0.53		0.53		0.53	
Total pressure (bar)	1		1		1		1	
Fe ²⁺ added (ppm)	100		100		100		100	
Test time (days)	16		23		9		14	
Specimens	2 electrochemical and 4 flat specimens		2 electrochemical, 4 flat specimens		2 electrochemical, 1 cylinder, and 3 flat specimens		2 electrochemical, 1 cylinder, and 3 flat specimens	

Table 4

Test conditions for experiments in NaClO₄ electrolyte

Electrolyte	1 wt.% NaClO ₄ (initially), after protective FeCO ₃ forms (2 days) more salt added until 21 wt.% NaClO ₄ (same ionic strength of 1.75 as 10 wt.% NaCl) was achieved.
Temperature (°C)	80
pH (initial)	6.6
Total pressure (bar)	1
Supersaturation of [FeCO ₃] _{initial}	745 (100 ppm Fe ²⁺)
Total time (days)	14
Material	X65
Numbers of specimens	2 electrochemical specimens for LPR 4 flat specimens for surface analysis (SEM, XRD, and IFM) and weight loss

Each test had two stages: 1) an FeCO₃ layer building procedure to develop a repeatable starting point; 2) an abrupt change in the NaCl or NaClO₄ concentration causing a drop in the saturation value of FeCO₃ which is expected to lead to the breakdown of the FeCO₃ layer. During the first stage, 100 ppm Fe²⁺ (as deoxygenated aqueous FeCl₂) was injected into the glass cell to accelerate the precipitation of FeCO₃ by increasing the supersaturation (SS) of FeCO₃ much higher than 1. The excess precipitation of FeCO₃ covers the mild steel surface causing the general corrosion rate obtained from LPR to decrease to around 0.1 mm/yr. A decrease in mass transfer of the corroding species also occurs as a consequence of a pseudo-passivation of the mild steel surface, which is indicated by an increase in the open circuit potential (OCP). At this

point, stage 1 is completed, and the iron carbonate layer is fully covering the specimen surface. Then, deoxygenated crystalline salt (NaCl or NaClO₄) was added into the system. For this second stage, the saturation of FeCO₃ was decreased to near 1 and a partial breakdown of the FeCO₃ layer should occur.

4.4 Tests in NaCl Electrolyte

4.4.1 Results and Discussion

In CO₂ corrosion of mild steel, when the product of the ferrous and carbonate ions concentration become larger than the equilibrium solubility product constant of FeCO₃, FeCO₃ can be formed on the mild steel surface, as depicted in the reactions and equations shown below :



The solubility constant, K_{sp} can be calculated by Sun & Nesic model [62]:

$$K_{sp(FeCO_3)} = 10^{-59.3498 - 0.041377 \times T_K - \frac{2.1963}{T_K} + 24.5724 \times \log(T_K) + 2.518 \times I^{0.5} - 0.657 \times I} \quad (28)$$

The saturation of FeCO₃, S_{FeCO_3} , is expressed as:

$$S_{FeCO_3} = \frac{C_{Fe^{2+}} C_{CO_3^{2-}}}{K_{sp(FeCO_3)}} \quad (29)$$

When $S_{FeCO_3} \gg 1$, FeCO₃ precipitates. When $S_{FeCO_3} = 1$, the FeCO₃ precipitation rate is equal to the dissolution rate and the system is in equilibrium. At equilibrium, the mass of a precipitated layer should not change over time. When $S_{FeCO_3} < 1$, FeCO₃ is supposed to dissolve.

Initial FeCO₃ layer. Figure 14 shows the comparison of the layer topography developed from both Test 1 (final [NaCl]=1 wt.%) and Test 2 (final [NaCl]=3 wt.%) in the conditions of 0.1 wt.% NaCl electrolyte, 80°C, initial pH 6.6, pCO₂ 0.53 bar. Figure 14a shows morphological features after the layer building for 2.5 days in 0.1 wt.% NaCl in Test 1, which consist primarily of plate and prism type crystal morphologies. Figure 14b shows the topography after the layer building for 2 days in 0.1 wt.% NaCl in Test 2, exhibiting similar surface morphologies to Test 1. Figure 15 is the cross-section morphology of the layer formed in Test 2 after the layer building for 2 days, which is the same specimen as in Figure 14b. From the cross-section, it is indicated that the layer was dense, thick, and protective.

XRD results in Figure 16 indicate a mixture of chukanovite (Fe₂(OH)₂CO₃) and iron carbonate was found on the surface where the plates were considered to be chukanovite and the prisms were considered to be iron carbonate. However, in Fajardo's research [50], the Raman spectroscopy, XPS (X-ray photoelectron spectroscopy and FIB/TEM/EDS (focused ion beam/ transmission electron microscopy/ energy-dispersive X-ray spectroscopy) results showed only iron carbonate was detected in the plates. Tanupabrungsun's [63] study proved that Fe₂(OH)₂CO₃ was an intermediate phase, converting to FeCO₃ finally according to equation (30).

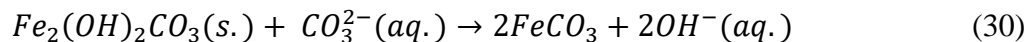
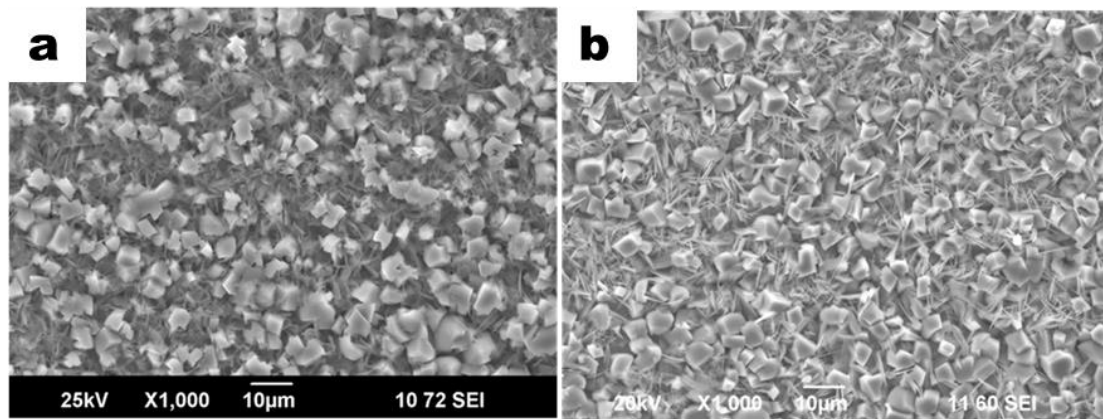


Figure 14

Surface morphology after the layer building process (0.1 wt.% NaCl electrolyte, 80 °C, initial pH 6.6, pCO₂ 0.53 bar): (a): Test 1; (b):Test 2

**Figure 15**

Cross-section analysis after the layer building process (0.1 wt.% NaCl solution, 80°C, initial pH 6.6, pCO₂ 0.53 bar) for Test 2

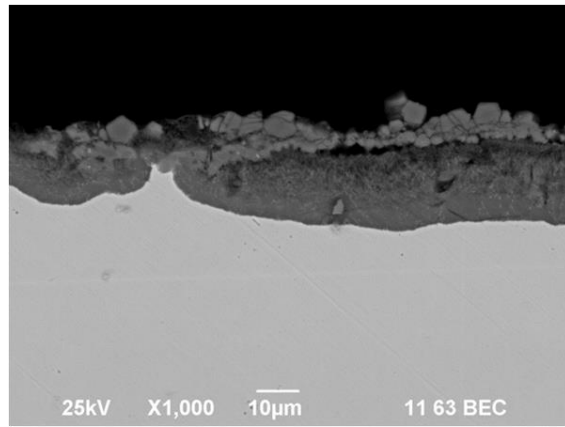


Figure 16

XRD results comparison for corrosion product formed in 1wt.% NaCl electrolyte at 80°C

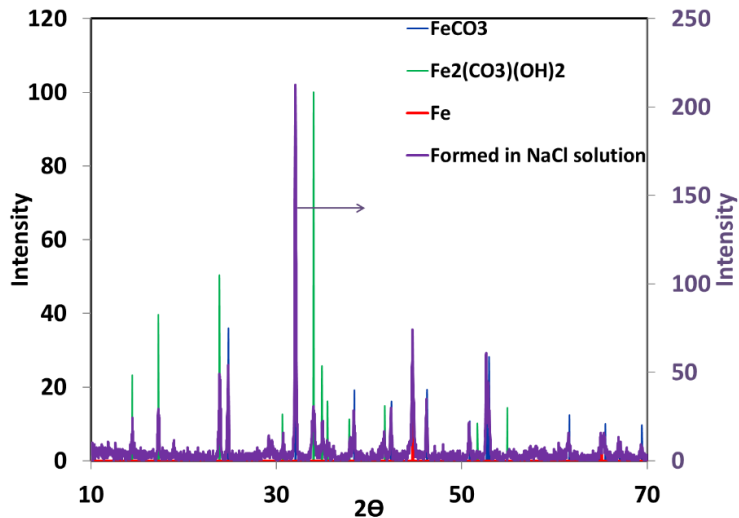


Figure 17 shows the comparison of the layer topography developed from both Test 3 (final $[\text{NaCl}] = 10 \text{ wt.\%}$) and Test 4 (final $[\text{NaCl}] = 15 \text{ wt.\%}$) in the conditions of 1 wt.% NaCl solution, 80°C, initial pH 6.6, pCO_2 0.53 bar. Figure 17a shows the topography after FeCO_3 building for 3 days in 1 wt.% NaCl in Test 3, which consists of a dense layer of prisms; a morphology consistent with FeCO_3 . Figure 17b shows the topography after FeCO_3 building for 1.5 days in 1 wt.% NaCl in Test 4, which shows similar surface morphology to Test 3.

Figure 18 shows the comparison of FeCO_3 layer cross-sections from Test 3 and Test 4. Figure 18a shows the cross-section morphology of the layer formed in 1 wt.% NaCl in Test 3 after FeCO_3 building for 3 days, which is the same specimen as Figure 17a. The cross-section shows that the layer was dense and adhered to the metal with a thickness of around $7\mu\text{m}$. Figure 18b is the cross-section morphology of the layer formed

in 1 wt. % NaCl in Test 4 after FeCO_3 building for 1.5 days, which is the same specimen as Figure 17b. The cross-section shows that the layer was also dense and adhered to the metal, with a thickness of around 9 μm .

Figure 17

Surface morphology after FeCO_3 building process: (a): Test 3 (1 wt.% NaCl); (b): Test 4 (1 wt.% NaCl)

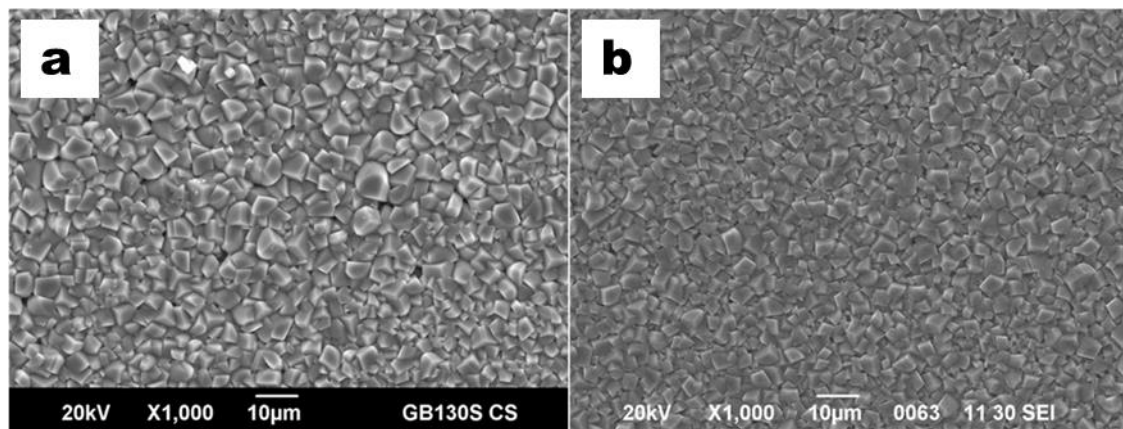
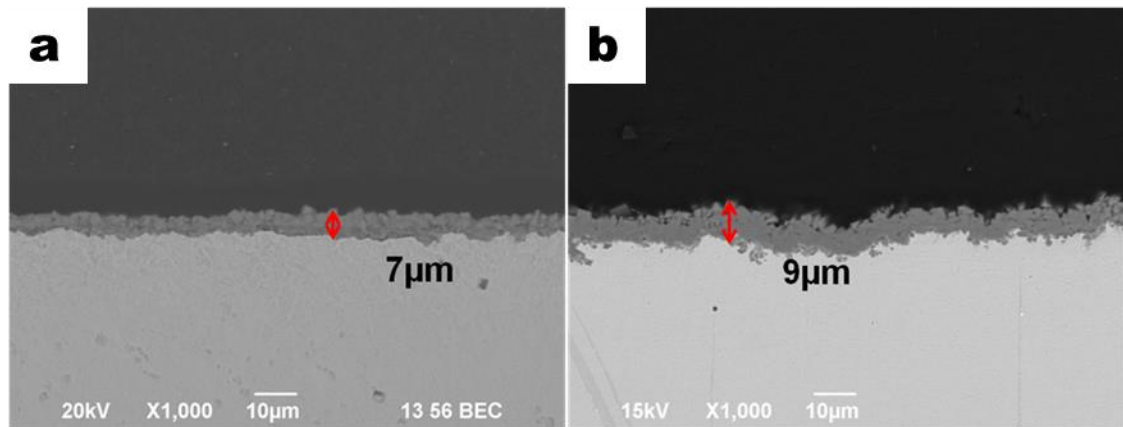


Figure 18

Cross-section analysis after FeCO₃ building a): Test 3 (1 wt.% NaCl); (b): Test 4 (1 wt.% NaCl)



These SEM images of the initial FeCO₃ layer precipitated in each test show there was very good repeatability in forming the beginning layer that would be challenged by the increased chloride concentration in stage 2.

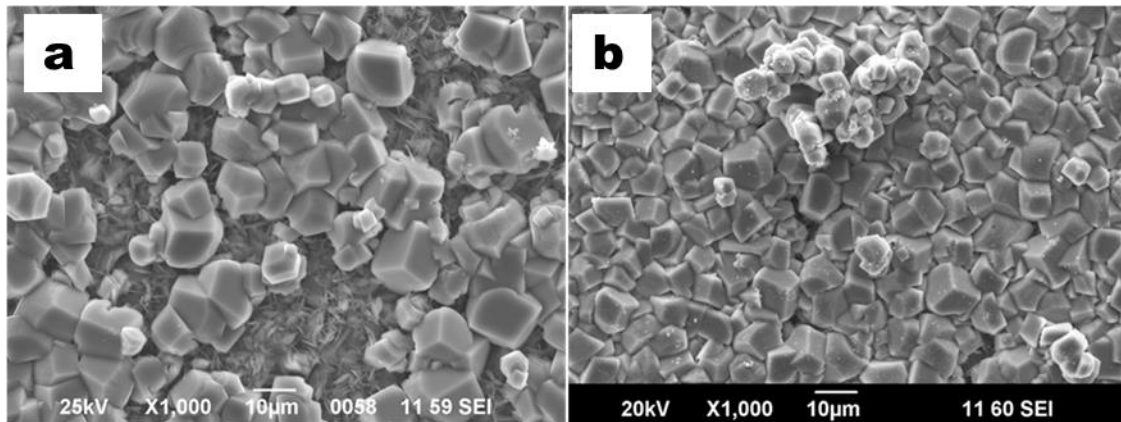
Adding More NaCl. The surface morphologies at the end of the Tests 1 & 2 are shown in Figure 19. Figure 19a is for Test 1 after the generated layer was exposed to 1 wt.% NaCl for 13.5 days; it indicates that the plates were the first to dissolve back into solution due to the decrease in bulk FeCO₃ saturation. Figure 19b is from Test 2 after the generated layer was exposed to the 3 wt. % NaCl for 21 days and shows only prisms, consistent with FeCO₃, remaining. Compared to Figure 14, the FeCO₃ prisms grew bigger. Figure 19a is the cross-section morphology of the layer formed in Test 1, which is the same specimen as that shown in Figure 19a; the layer was still dense with a thickness of 21 μm with no general corrosion or pitting located.

Figure 20b is the cross-section morphology of the layer formed in Test 2, which is the same specimen as in Figure 19b; in this case the layer was generally attacked with areas of crystals missing and corrosion proceeding into the metal substrate, but no pitting was found.

The surface morphologies at the end of Test 3 from two different specimens are shown in Figure 21 after the generated layer was exposed to 10 wt.% NaCl for 6 days. Figure 21a shows part of the FeCO₃ layer was degraded. In Figure 21b, some gaps appeared between iron carbonate crystals. The steel surface was exposed and the EDS result, Figure 22, proved it. Figure 23 shows the surface morphologies at the end of Test 4 after FeCO₃ was exposed to the 15 wt.% NaCl for 12.5 days. Part of the steel surface was exposed as shown in Figure 23b. It is noteworthy that the iron carbonate crystals (in Figure 21 and Figure 23) continued to grow with time even after adding additional salt in both tests (compared to Figure 17).

Figure 19

Surface morphology after adding more NaCl for: (a): Test 1 (1 wt.% NaCl); (b): Test 2 (3 wt.% NaCl)

**Figure 20**

Cross-section after adding more NaCl for: Test 1 (1 wt.% NaCl); (b): Test 2 (3 wt.% NaCl)

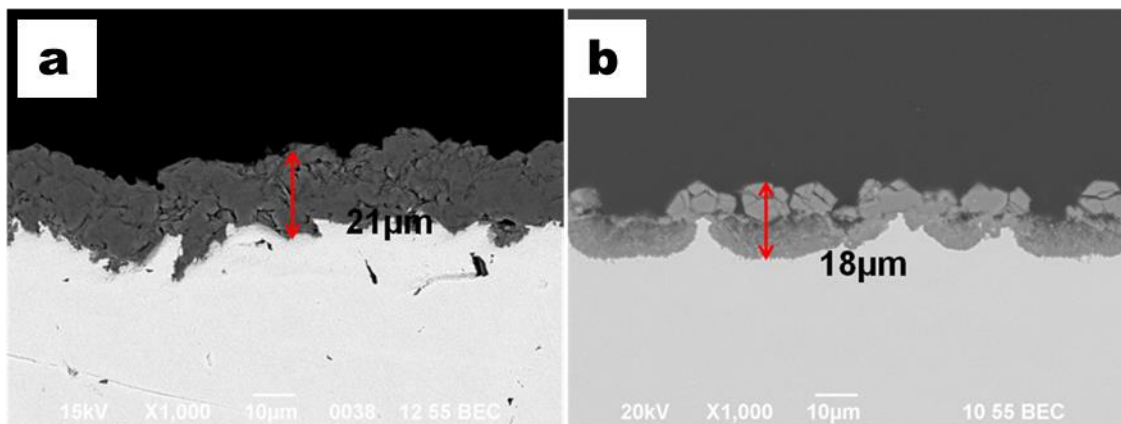
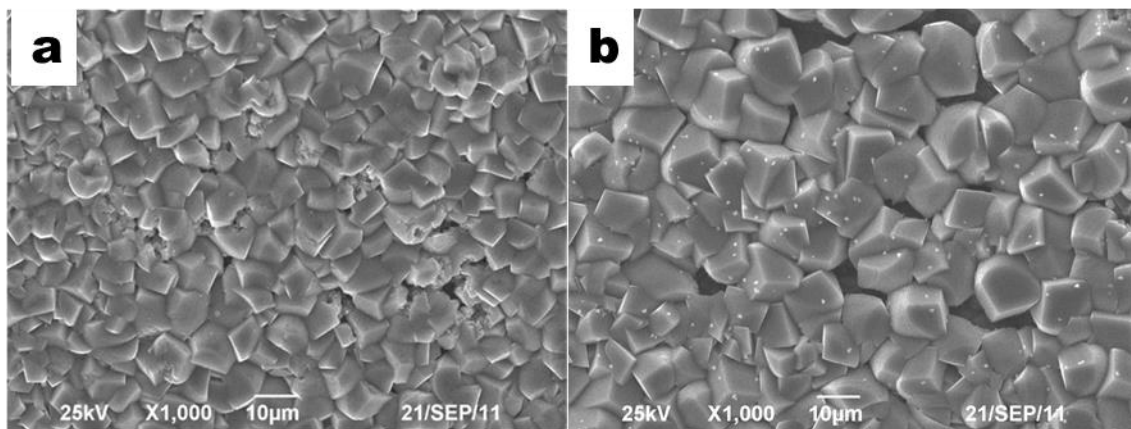


Figure 21

Surface morphology of specimens in Test 3 (10 wt.% NaCl) at the end of the experiment ,

(a) and (b) from two different specimens

**Figure 22**

Composition analysis of the corrosion layer by EDS of specimen in Test 3 (10 wt.%

NaCl) at the end of the experiment

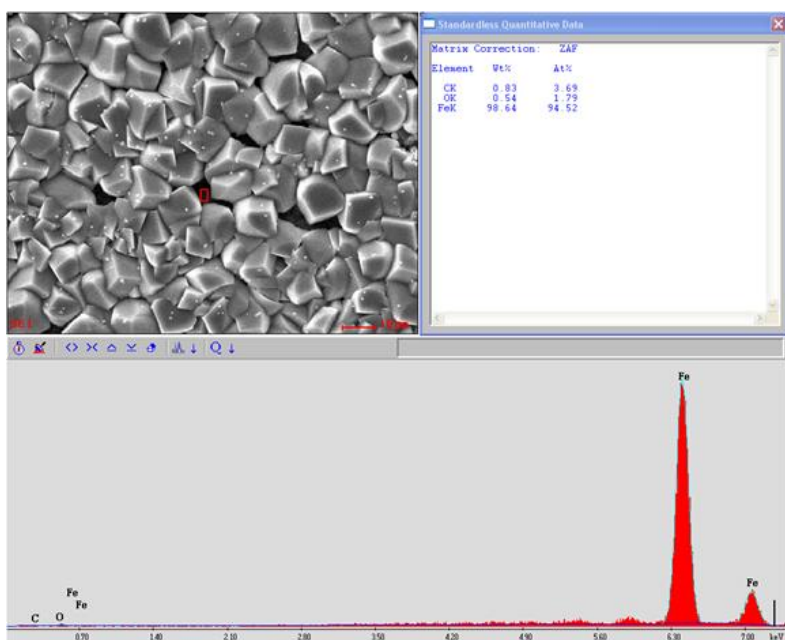


Figure 23

Surface morphology of specimens in Test 4 (15 wt.% NaCl) at the end of the experiment

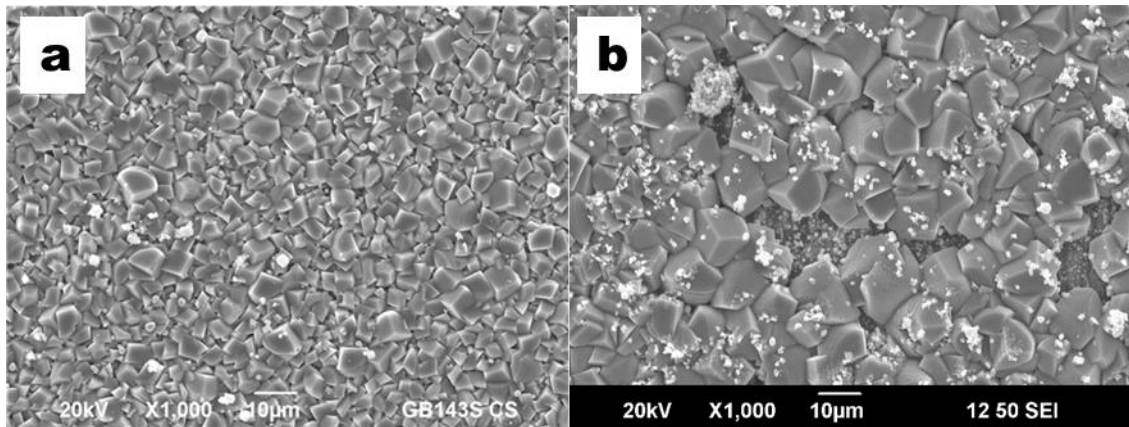
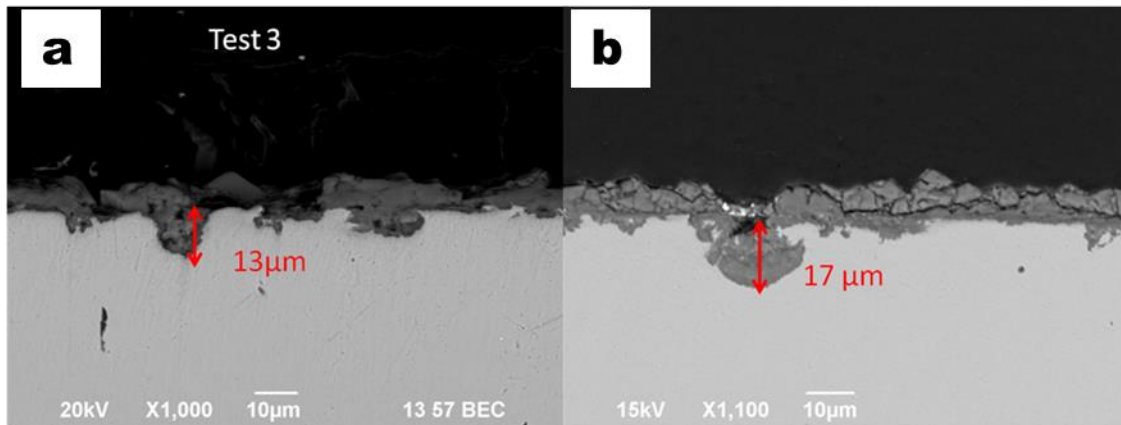


Figure 24a is the cross-section morphology of the layer at the end of Test 3, which is the same specimen as in Figure 21a; it indicates a pit with a depth of 13 µm was detected. Figure 24b is the cross-section morphology of the FeCO₃ layer at the end of Test 4, which is the same specimen as Figure 23a; it also indicates a pit with a depth of 17 µm was detected.

Figure 24

Cross-section for: (a) Test 3 (10 wt.% NaCl); (b) Test 4 (15 wt.% NaCl)



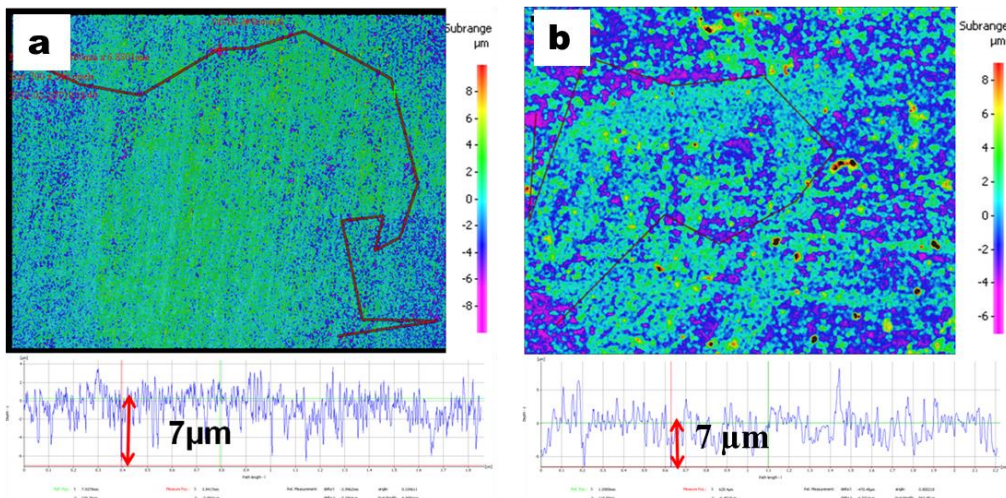
Profilometry Analysis. A 3-D profilometer, specifically an infinite focus microscope (IFM), was used to measure the pit depth and observe the surface morphologies after corrosion product removal using Clarke solution [64] for Tests 1 & 2, which are shown in Figure 25. Several locations were analyzed, and the maximum depth of pitting found for both tests was 7 μm . Based on the distance from the corroded specimen surface to the bottom of the deepest pit measured, the pit penetration rate (mm/yr) was calculated and compared with the general corrosion rates obtained from weight loss (Table 5). Pitting ratio, defined as part of the Corrosion Center Joint Industry Project consortium at the ICMT [65] based on ASTM G46 [66] and years of experimental experience, was used as a method to qualify pitting corrosion; it is calculated as the pit penetration rate divided by the weight loss corrosion rate (see Appendix B). If the pitting ratio is less than 3, the observed pits are not considered localized corrosion, just initiation of general corrosion. If the pitting ratio is greater than 5, the observed pits are considered

to be localized corrosion. If the pitting ratio is between 3 and 5, localized corrosion is possible, but a description of the pit shape and pit density must be included if the final result is to indicate it is localized corrosion. The pitting ratio calculated for Test 1 was 0.3 and for Test 2 was 0.4; both were less than 3 and, therefore, no localized corrosion was found for those two tests.

The surface morphologies after corrosion product removal using Clarke solution [64] for Tests 3 and 4 are shown in Figure 26. After scanning several locations, the deepest pits observed for both tests were 11 μm . Based on this depth and the general corrosion rates obtained from weight loss (Table 5), the pitting ratio for Test 3 and for Test 4 were both 3.3; and therefore, it cannot be stated with certainty that localized corrosion was initiated. Therefore hypothesis 1 was not confirmed. The profilometry results agree with the results obtained from SEM cross-section analysis.

Figure 25

IFM images and analysis of the corrosion product layer after layer removal for: (a): Test 3 (1 wt.% NaCl); (b): Test 4 (3 wt.% NaCl).

**Figure 26**

IFM images and analysis of the corrosion product layer after layer removal: (a): Test 3 (10 wt.% NaCl); (b): Test 4 (15 wt.% NaCl)

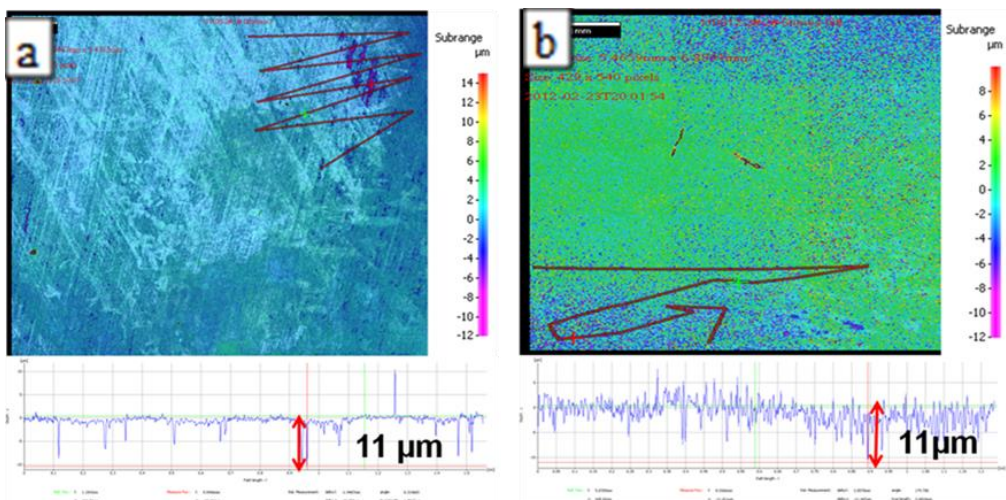


Table 5

Weight loss results for the four tests

Test number	Weight before experiment (g)	Weight after experiment (g)	Weight after Clarke solution [64] (g)
1	2.1833	2.1821	2.1749
2	2.2565	2.2526	2.2393
3	1.7439	1.7481	1.7396
4	2.1583	2.1612	2.1547

Corrosion Rates Comparison. The comparison of the general corrosion rates integrated from LPR curves and calculated from weight loss for those four tests is shown in Figure 27. Increasing the concentration of the NaCl solution decreased the general corrosion rate. This observation was also reported in experiments conducted by Fang [33] and Madani Sani [67]. This can be postulated to be due to the reduction of CO₂ solubility and decrease of the diffusivity of species. In Section 3.5, Figure 6, Figure 7, Figure 8 show that both predicted CO₂ solubility in aqueous NaCl by models and experimental CO₂ solubility decrease with increasing ionic strength. Madani Sani's study indicated that [H⁺] decreased as the [NaCl] increased from 1 wt.% to 20 wt.% due to reduction of CO₂ solubility. Kestin, *et al.*[68] measured the viscosity of aqueous NaCl solutions in the conditions of 20-150°C, 0.1-30 MPa and 0-5.4 M NaCl and found that the viscosity increases with the increase of [NaCl], which could decrease the diffusivity of species.

Figure 27

General corrosion rate comparison for the four tests defined in Table 3

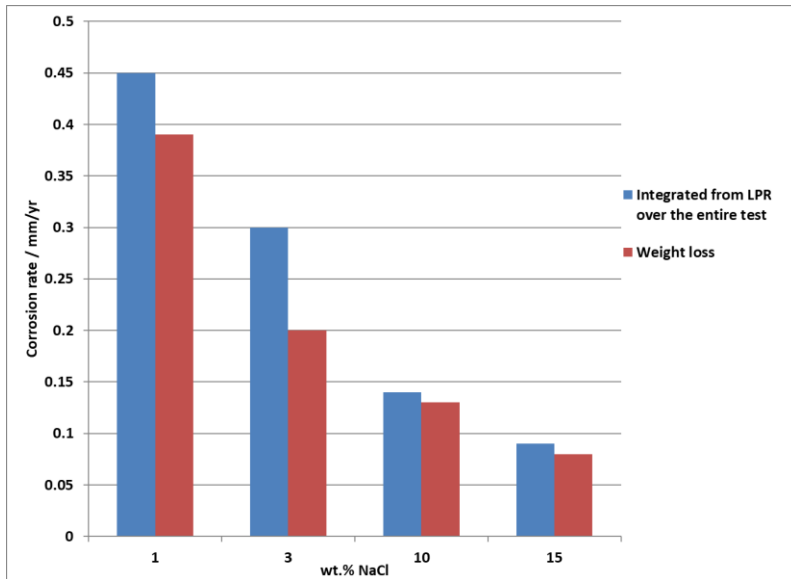
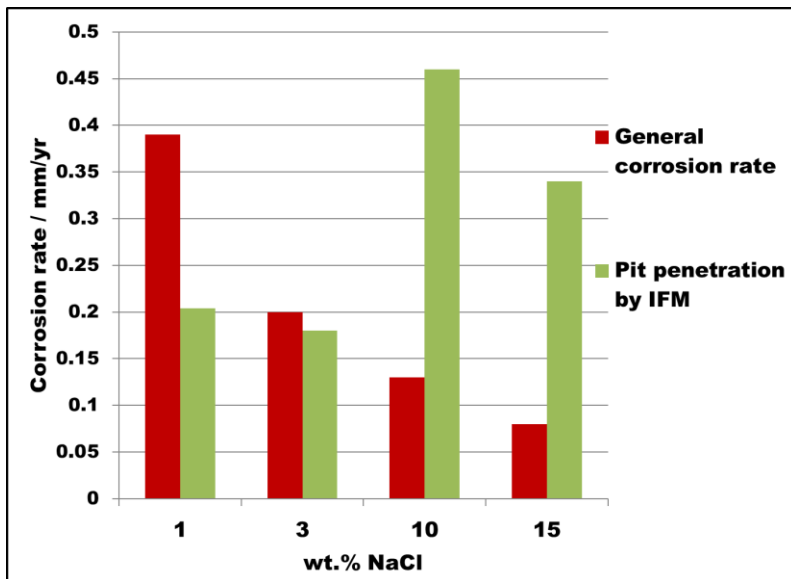


Figure 28 shows the pit penetration rates with respect to the general corrosion rates from weight loss after adding addition salts for those four tests. For Test 1 and Test 2, the pit penetration rate was lower than the general corrosion rate, which means no localized corrosion occurred for Tests 3 & 4, the pit penetration rates were higher than the general corrosion rate but were not higher enough to confirm for localized corrosion initiation. Here again, hypothesis 1 was not confirmed.

Figure 28

Pit penetration rate with respect to the general corrosion rate for those four tests



4.4.2 Summary I

SEM cross-section and IFM analysis results indicate no localized corrosion was initiated by adding more salts.

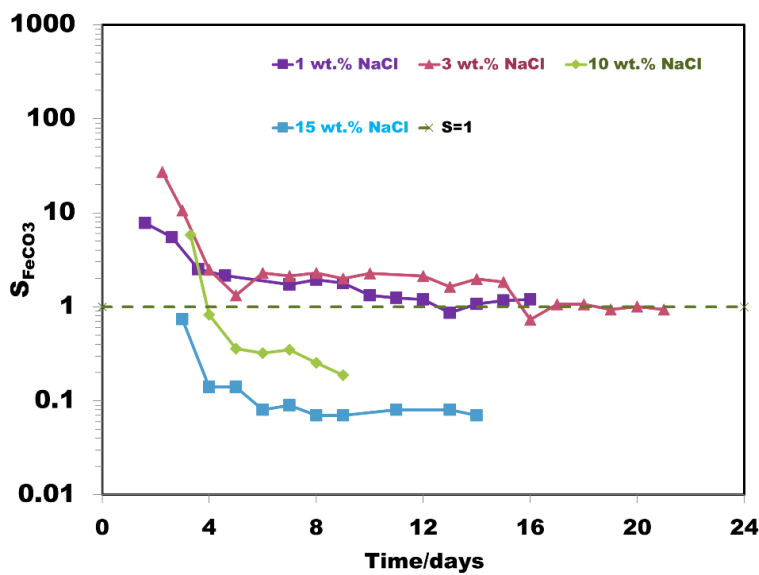
4.5 Tests in NaClO₄ solution

4.5.1 Why Change the Salt?

From Part I tests, when comparing the supersaturation of FeCO₃ as shown in Figure 29, it was found that at 1 wt.% and 3 wt.% NaCl solution, the FeCO₃ saturation was mostly above 1; and at 10 wt.% and 15 wt.% NaCl solution, the FeCO₃ saturation was much less than 1.

Figure 29

Comparison of the calculated FeCO_3 saturation values after adding chloride for the four tests (first points were before adding more salt)



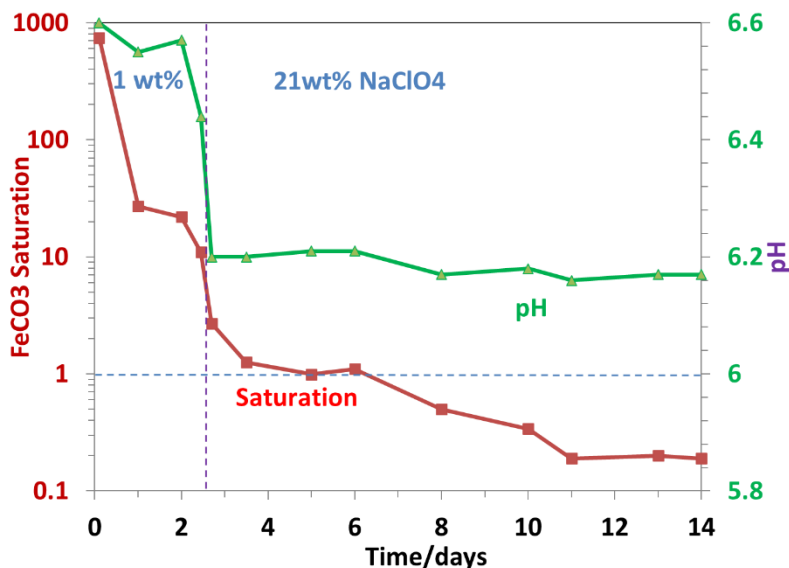
As is known, FeCO_3 saturation is directly related to the FeCO_3 solubility, K_{sp} , which is a function of ionic strength. According to equation(18), high concentration of NaCl increases the ionic strength which can increase K_{sp} (equation (28)). In section 3.5, it has been discussed that CO_2 solubility will reduce with the increase of [NaCl], leading to the reduction of $[\text{CO}_3^{2-}]$. Consequently, the bulk FeCO_3 saturation decreases according to equation (29). Adding any type of salt can increase the ionic strength. Therefore, using NaClO_4 to replace NaCl should also lead to the bulk FeCO_3 saturation decrease. NaClO_4 was chosen because it will not reduce or be involved in the chemical reactions; the perchlorate ion is stable under the test conditions.

4.5.2 Results and Discussion

Corrosion Behavior. The variances of the saturation of FeCO_3 and the solution pH with the concentration of NaClO_4 is shown in Figure 30. During the first two days of the FeCO_3 layer building process, the saturation decreased from 745 to around 10, which means that iron was consumed to form FeCO_3 . The solution pH decreased from 6.60 to 6.44, which means equations (6) and (7) had reacted forwards due to carbonate ion consumption. After additional NaClO_4 was added into the system, the saturation of FeCO_3 decreased significantly to much less than 1.

Figure 30

Variance of S_{FeCO_3} and pH of the solution with time (NaClO_4 , 80 °C)



SEM Analysis. Figure 31 shows the surface morphology of the FeCO₃ layer after 2 days of the layer building process under conditions of 1 wt.% NaClO₄ solution, 80 °C, initial pH 6.6, pCO₂ 0.53 bar. The FeCO₃ layer appears dense. Figure 32 shows the cross-section of the same specimen as Figure 31. The layer was dense and uniform with a thickness of 6μm. Compared to the FeCO₃ formed in the test for 1 wt.% NaCl as shown in Figure 18 (the thickness was 7μm), the FeCO₃ layer appeared similar.

Figure 31

Surface morphology after FeCO₃ layer building process (1 wt.% NaClO₄ solution, 80 °C)

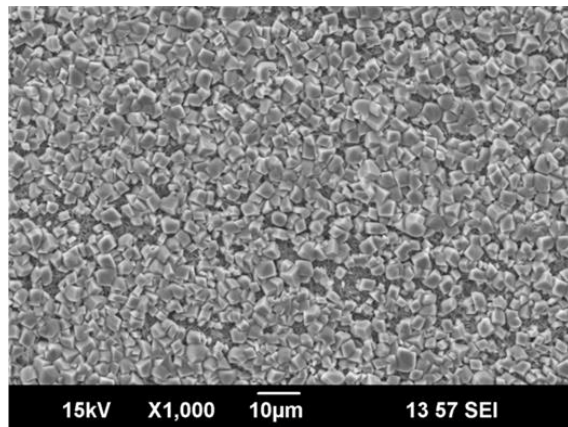


Figure 32

Cross-section analysis after FeCO₃ building process (1 wt.% NaClO₄ solution, 80°C)

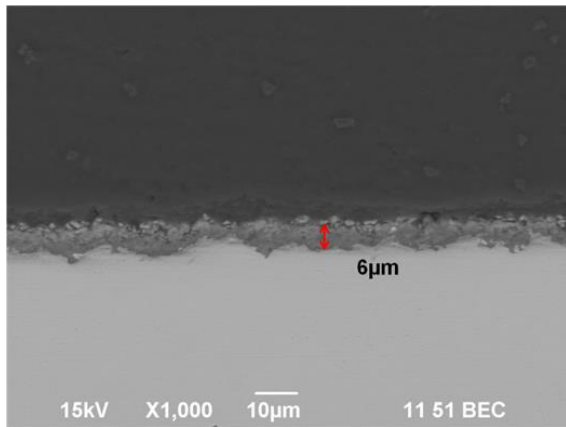
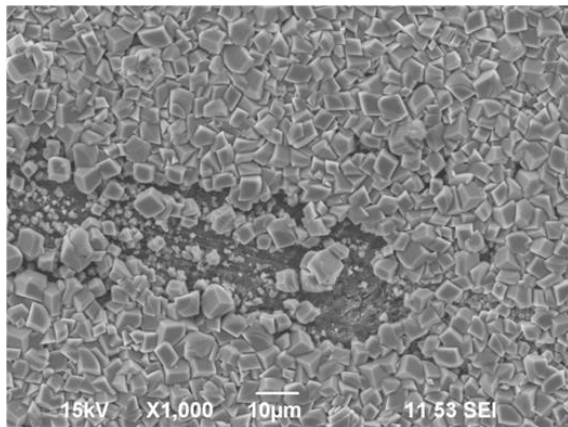


Figure 33 shows the surface morphology of the layer after adding additional NaClO₄ for 6 days. Some gaps appeared in the layer, which means that some crystals selectively dissolved. The reason for this remains clear and needs more investigation. FeCO₃ prisms crystals grew bigger compared to the ones on Figure 31.

Figure 34 shows the cross-section of the same specimen as shown in Figure 33. It indicates a pit with a depth of 12 μm was detected.

Figure 33

Surface morphology after adding more NaClO₄ (6 days in 21 wt.% NaClO₄, 80°C)

**Figure 34**

Cross-section analysis after adding more NaClO₄ (6 days at 21 wt.% NaClO₄)

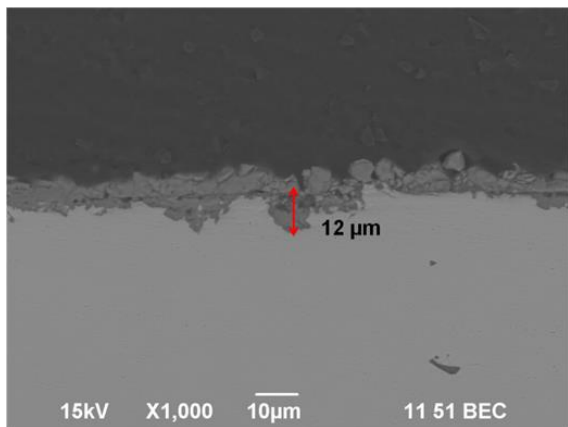


Figure 35 shows the surface morphology of the layer after adding additional NaClO₄ for 12 days. It was similar to the surface morphology in Figure 33 (6 days at 21 wt.% NaClO₄). Figure 36 shows the cross-section of the same specimen as Figure 35; it

shows pitting with a deeper depth of 19 μm was found. Compared to the pit depth of 12 μm after introduction of additional NaClO_4 for 6 days, pits had barely grown.

Figure 35

Surface morphology after adding more NaClO_4 (12 days at 21 wt.% NaClO_4)

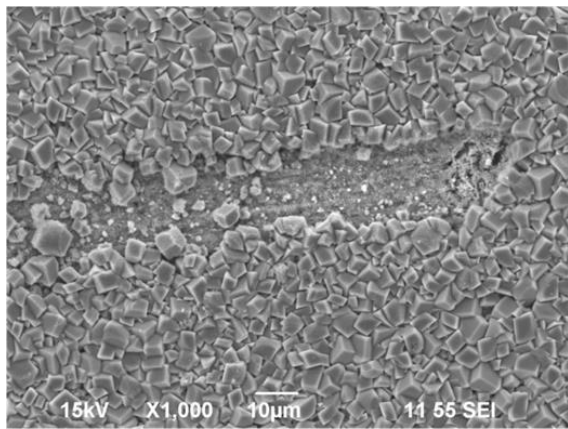
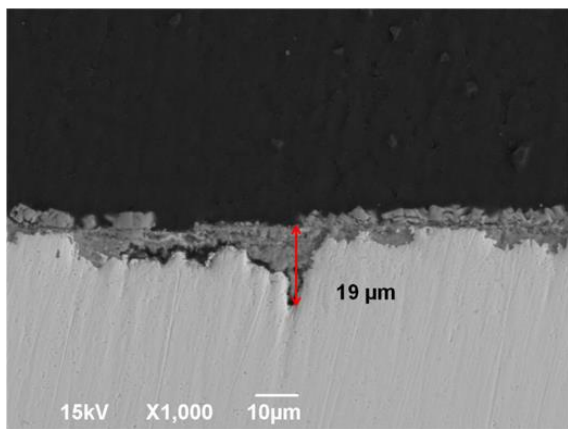


Figure 36

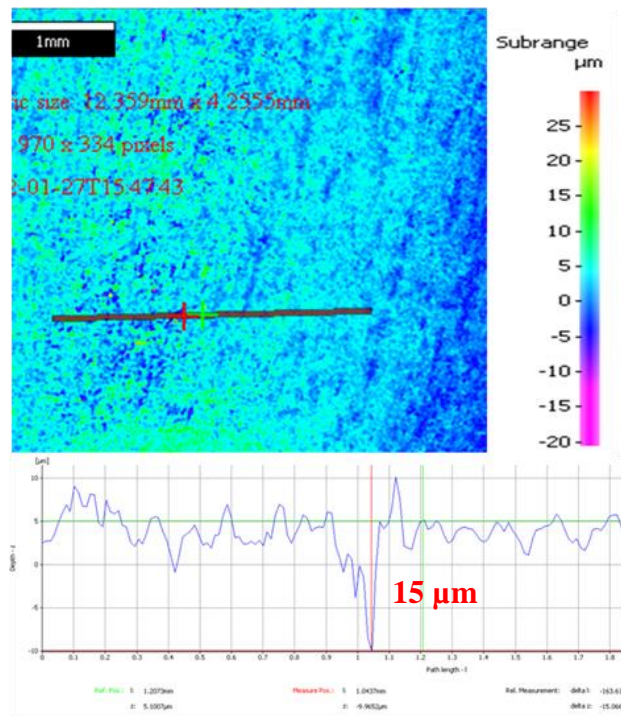
Cross-Section analysis after adding more NaClO_4 (12 days at 21 wt.% NaClO_4)



Profilometry Analysis. Figure 37 shows the surface morphologies after corrosion product removal using Clarke solution [64] at the end of the test. The whole surface was scanned, and the deepest pit observed was 15 μm . Based on this depth, the pit penetration rate was 0.45 mm/yr; the general corrosion rate calculated from weight loss was 0.17 mm/yr. The pitting ratio was 2.7, smaller than 3. Therefore, it was not considered as localized corrosion. This result was consistent with that obtained from SEM cross-section analysis.

Figure 37

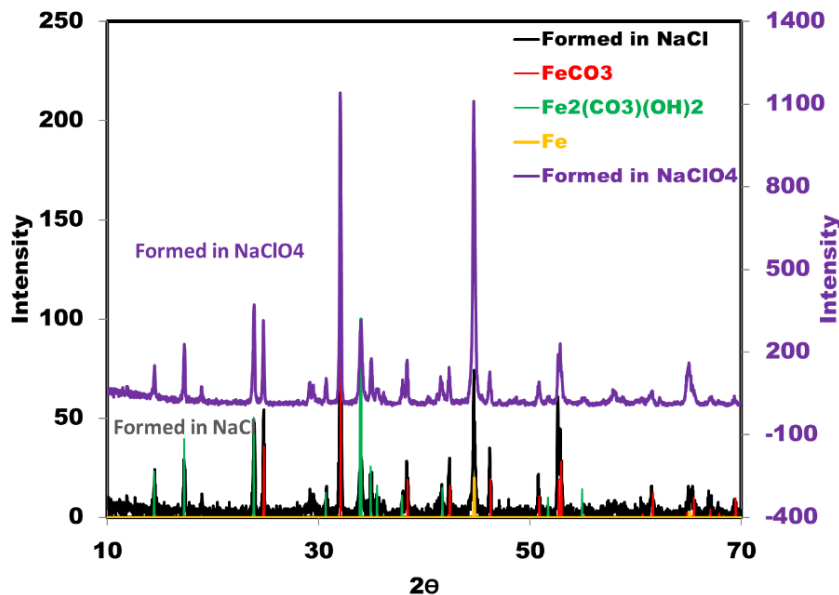
IFM images and analysis of the corrosion product layer after layer removal (12 days at 21 wt.% NaClO₄)



XRD Results. In order to check if the same corrosion products were formed at NaCl and NaClO₄ solutions, XRD analysis was conducted. The detected XRD results of the specimen at NaClO₄ solution (the purple line) indicated that the surface layer was composed of FeCO₃ and Fe₂(CO₃)(OH)₂, on a primarily α-Fe substrate (the mild steel). These results agree with the one obtained in NaCl electrolytes (the black line), as shown in Figure 38.

Figure 38

XRD results comparison for corrosion product formed at NaClO₄ and NaCl (Test 3, 10 wt. % NaCl) solutions

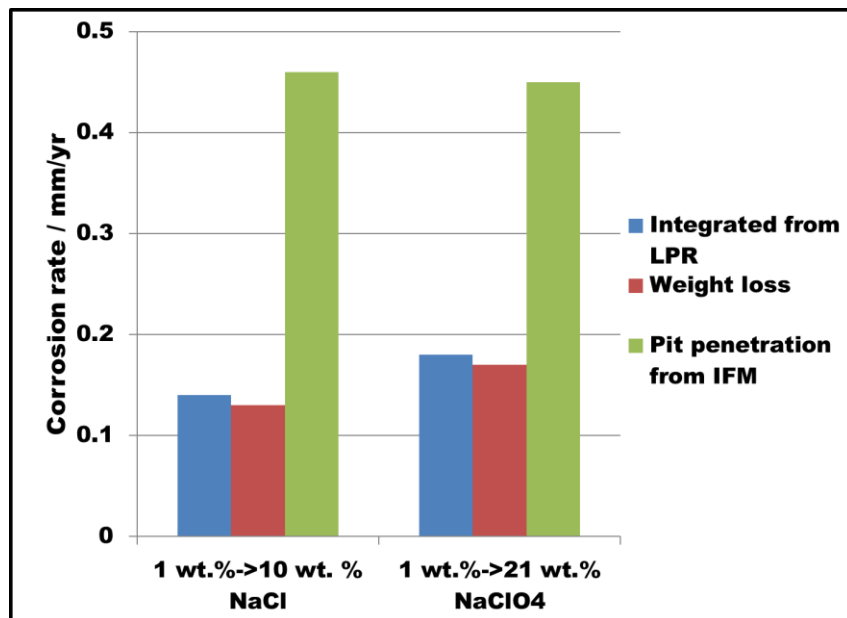


Corrosion Rates Comparison. Figure 39 shows the comparison of corrosion rates for NaClO₄ and NaCl tests. The general corrosion rates integrated from LPR were consistent with those calculated from weight loss. For both tests, the pit penetration rates

were higher than the general corrosion rates; but were not high enough to confirm for localized corrosion initiation.

Figure 39

Corrosion rate comparison between NaCl and NaClO₄



4.6 Summary

- Saturation of FeCO₃ was decreased by increasing the ionic strength by adding either NaCl or NaClO₄.
- Localized corrosion was not initiated by adding more salts.

Chapter 5: Qualitative Study of the Equilibrium of FeCO₃ Precipitation in Non-ideal Solutions

5.1 Introduction

In Chapter 4, it was observed that although the calculated value for S_{FeCO_3} was much less than 1 after the change in salt concentration (Figure 29 and Figure 30), the FeCO₃ layer remained mostly intact while it would have been expected to dissolve to reach the equilibrium state where $S_{FeCO_3}=1$. In Chapter 3, the model for calculation of water chemistry was revised. In this chapter, the revised model will be used to recalculate the saturation of FeCO₃ in Chapter 3. An *in situ* mass change measurement device known as the Electrochemical Quartz Crystal Microbalance (EQCM) was used to study the equilibrium of FeCO₃ precipitation in non-ideal solutions. A new model for the equilibrium of FeCO₃ precipitation is then proposed.

Iron-coated and gold-coated quartz crystals were used in the research. The iron-coated quartz crystals would corrode similar to pure iron and lose mass due to corrosion. Therefore, iron-coated crystals were used at the beginning to learn how iron carbonate precipitated on the crystal and how long it would take to reach equilibrium. Gold is inert in the experimental conditions and FeCO₃ precipitation is the only process to stimulate the frequency change of EQCM measurements. Therefore, Au-coated quartz crystals were used in the study to exclude any other effect.

5.2 Objective

- Validate the water chemistry calculations provided by Oddo & Tomson for a range of ionic strengths (corresponding to NaCl concentrations from 0 to 25 wt.%) and range of temperatures (from 25°C to 80°C).
- Study the equilibrium of FeCO₃ dissolution and precipitation in non-ideal solutions by the electrochemical quartz crystal microbalance (EQCM).
- Verify the previous model for iron carbonate saturation through testing and develop a model to compensate for changes in ionic strength if needed.

5.3 Equilibrium of Iron Carbonate on an Iron Coated Quartz Crystal in High Concentration Salt Solution (without pH Adjustment)

5.3.1 Experimental Method

Experimental Setup. In order to study the effect of salt concentration on a generated FeCO₃ layer, an *in situ* mass measurement device known as the Electrochemical Quartz Crystal Microbalance (EQCM), designed and manufactured by Stanford Research Systems, was used (Figure 40). Mass change on the quartz crystal surface is reflected by changes in its oscillation frequency based on the Sauerbrey equation [69] (equation (31)).

$$\Delta f = -C_f \cdot \Delta m \quad (31)$$

where

Δf = frequency change in Hz,

Δm = the mass change per unit area in g/cm²

C_f = the sensitivity factor for the crystal (56.6 Hz·cm²/μg for the current work)

An iron coated EQCM crystal was used in the experiment. The experiments were carried out in a 2-liter glass cell with three electrodes as shown in Figure 41. In order to exclude a possible oxygen effect on corrosion, a special container (Figure 42) was implemented to remove O₂ when adding extra NaCl needed during the experiment.

Figure 40

Complete QCM setup consisting of Digital Controller, Crystal Oscillator, and Crystal Holder. Taken from [25]

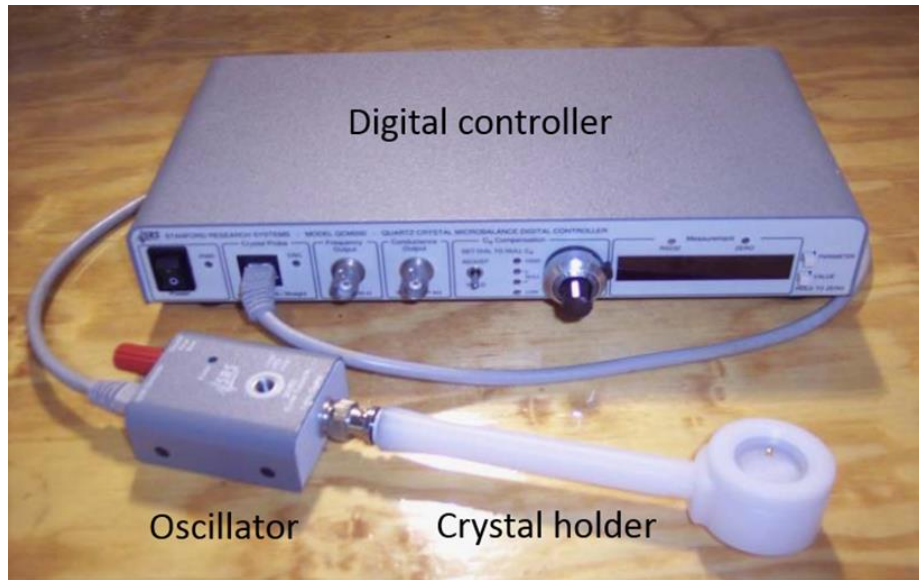
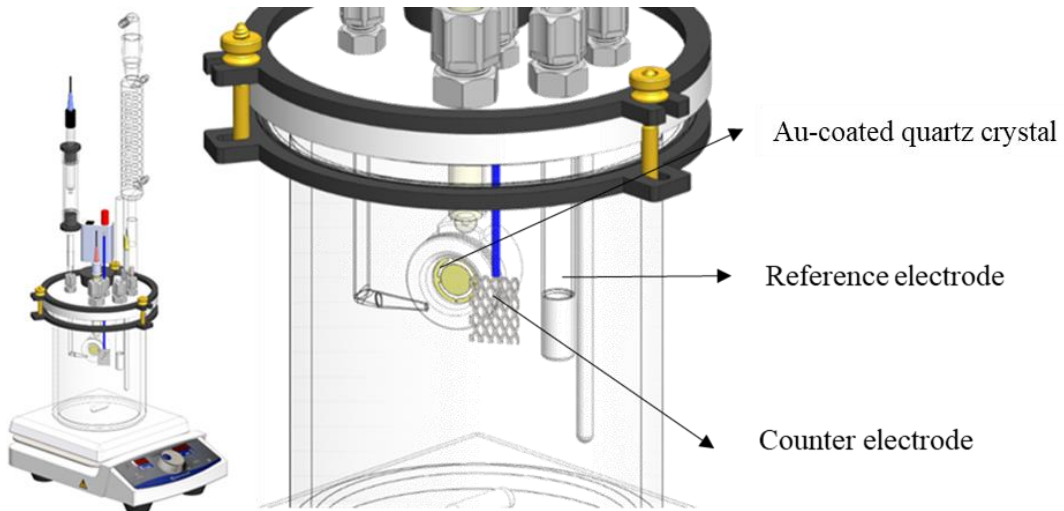
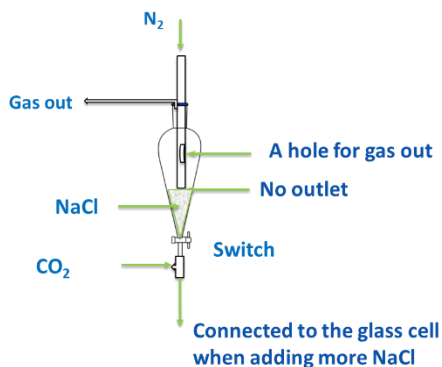


Figure 41

Experimental setup with EQCM (Image courtesy of Cody Shafer, ICMT)[61]

**Figure 42**

Specially designed container for adding extra NaCl into the glass cell



Experimental Conditions. The test conditions for experiments associated with aqueous equilibrium of FeCO_3 on iron-coated crystals is shown in Table 6.

Table 6

Test conditions for experiments associated with aqueous equilibrium of FeCO_3 on iron-coated quartz crystal

Total pressure/bar	1
Sparge gas	CO_2
Temperature/ $^{\circ}\text{C}$	80
Initial solution pH	6.6
Materials	Polished Fe-coated quartz crystal
Stir bar speed/rpm	50
Initial $[\text{Fe}^{2+}]$ /ppm	~ 100
Initial NaCl Solution	1 wt%
Final NaCl Solution	10 wt.%

Experimental Procedure. The detailed test procedure is as follows:

- 1) Set up glass cell with 2L deionized (DI) water with 20.2g NaCl and 3.8g NaHCO_3 .
- 2) Sparge with CO_2 for at least 2 hours.
- 3) Heat to 80°C .
- 4) Check Ag/AgCl reference electrode and ensure it is -45mV *vs.* SCE.

- 5) Calibrate pH probe at 80°C (using buffers at pH 4.16 and 7.04).
- 6) Check the pH of the electrolyte in the glass cell and adjust to pH 6.6 by adding 1M NaHCO₃ (should be purged with N₂ before adding to facilitate deoxygenation).
- 7) Wait for the pH measurement to be stable for at least 30 minutes before proceeding.
- 8) Clean the crystal with compressed N₂.
- 9) Prepare 100ml DI H₂O in a flask and purge using N₂, for use later in this procedure.
- 10) Check the conductivity of the metal surface of the crystal through the holder to the connector pins.
- 11) Put the crystal into its holder and connect with the EQCM system; In the air, the frequency should be around 5MHz.
- 12) Run the EQCM and start to record the data while the probe is still in the air.
- 13) Put the crystal holder into the glass cell solution (the frequency should be 5 MHz).
- 14) Connect the potentiostat (Gamry Reference 600TM) to the crystal holder and measure the open circuit potential (OCP) and linear polarization resistance (LPR) of the crystal in the solution.
- 15) Weigh 7.1g FeCl₂.4H₂O and add into the 100ml deaerated DI H₂O
- 16) Take 10ml from the above FeCl₂ solution and add into the glass cell for 100 ppm [Fe²⁺].

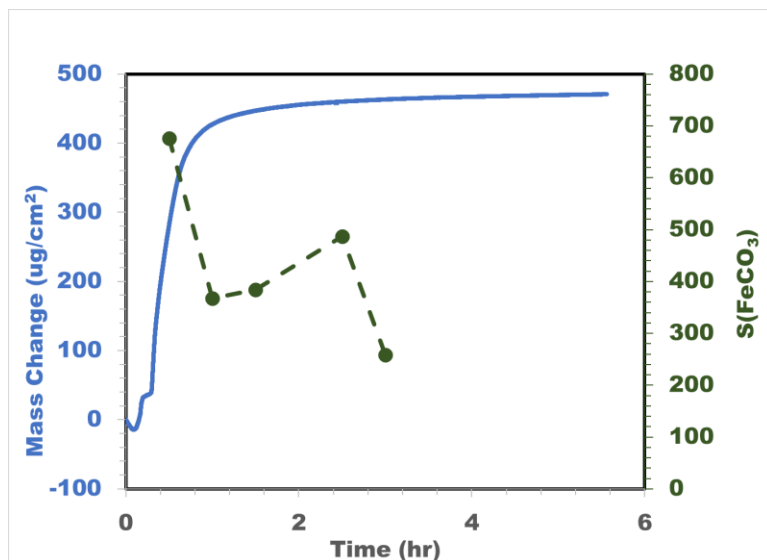
- 17) Take out specimens of solution periodically from the system and measure $[Fe^{2+}]$ by a HACH DR 3000 spectrophotometer (see Appendix I Procedure of Iron Ion Measurement for the detailed method refers to Method 8146 [70]). Record pH at the same time.
- 18) Weigh 202g NaCl, put it into the adapted separatory funnel (as shown in Figure 42), and purge with N_2 for at least 2 hours.
- 19) Add above deaerated 202g NaCl into the glass cell when no mass change (less than $1 \mu\text{g}/\text{cm}^2$ per hour) for FeCO_3 building.
- 20) Take out some amount of solution (1 ml, 2 ml or 5 ml, depending on the Fe^{2+} concentrations) periodically from the system and measure $[Fe^{2+}]$ using the HACH spectrophotometer. Record pH at the same time.
- 21) Stop the experiment.

5.3.2 Results and Discussion

Iron Carbonate Layer Formation. The mass change monitored by EQCM is shown in Figure 43. In the first two hours, the mass increased quickly from 0 to around $450 \mu\text{g}/\text{cm}^2$ due to precipitation of FeCO_3 on the quartz crystal. Some solution (around 2 ml) was taken out of the glass cell for measuring ferrous iron concentration and pH was recorded at the same time. Then, equations (9) and (28) are used to calculate S_{FeCO_3} . As shown in Figure 43, S_{FeCO_3} decreased from 600 to around 380 with FeCO_3 formation in the first two hours. In this figure, the measurements of S_{FeCO_3} seems to be erroneous for reasons that were not determined.

Figure 43

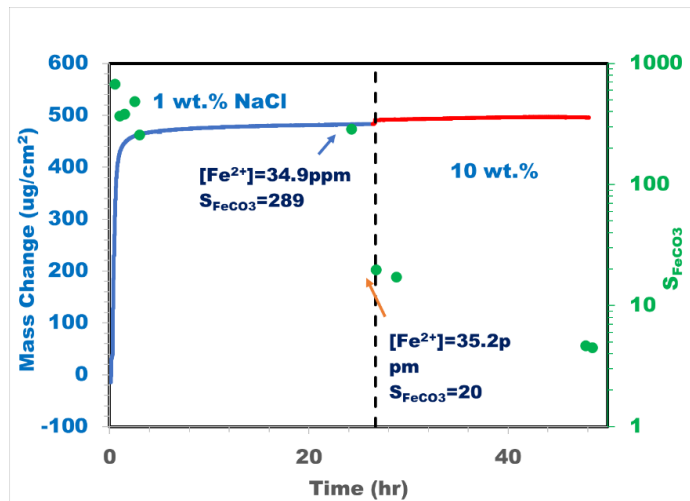
Mass change (left y-axis) and S_{FeCO_3} (right y-axis) obtained on Fe-coated quartz crystal in $FeCO_3$ layer formation test at 80°C



Adding more NaCl (10 wt.%). When the mass uptake reached a steady state, extra deaerated NaCl was added into the glass cell to increase the NaCl concentration to 10 wt.%. The mass increased from 480 to 490 $\mu\text{g}/\text{cm}^2$. $[\text{Fe}^{2+}]$ had only a slight increase (from 34.9 ppm to 35.2 ppm) and pH decreased from 6.67 to 6.38. Thus, S_{FeCO_3} decreased from 289 to 20. At the end of the experiment, S_{FeCO_3} remained above 1.

Figure 44

Mass change (left) and S_{FeCO_3} (right) obtained on a Fe-coated quartz crystal at 80°C

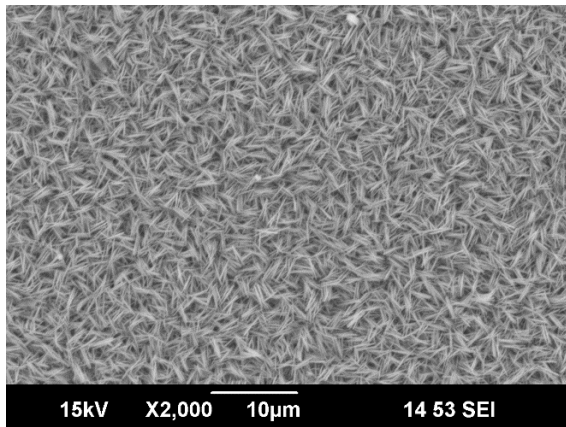


Surface Morphology. An SEM image of the layer formed on the iron-coated quartz crystal is shown in Figure 45. Only plates shaped products were formed.

In the previous experiment where pH was not adjusted, S_{FeCO_3} remained above 1 during the test indicating that the system never reached equilibrium. Ideally, S_{FeCO_3} would get to 1 eventually, however, it may take an unrealistically long duration. Therefore, in order to accelerate this process, 1N HCl was added to adjust the pH for the purpose of dissolving the surplus carbonate.

Figure 45

SEM image of iron carbonate layer formed on iron-coated quartz crystal at the end of the experiment



5.4 Equilibrium of Iron Carbonate on an Iron Coated Quartz Crystal in High Salt Solution with pH Adjustment

5.4.1 Experimental Method

Experimental Setup. The same test setup was used as the previous test in 5.2.

Experimental Procedure. Steps 1)– 17) were the same as steps 1) – 17) in the previous section 5.3.1, then::

18) Add 1N HCl to adjust pH to make the solution significantly undersaturated.

19) Add 202g deaerated NaCl into the glass cell when the mass reaches a steady state and saturation returns to 1.

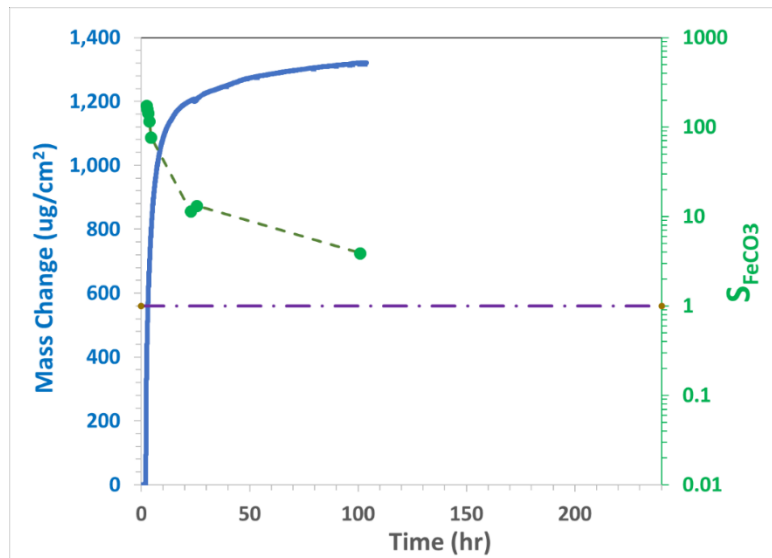
- 20) Take out some amount of solution (1 ml, 2 ml or 5 ml, depending on the Fe^{2+} concentrations) periodically from the system and measure $[\text{Fe}^{2+}]$ using the HACH spectrophotometer. Record pH at the same time.
- 21) Stop the test.

5.4.2 Results and Discussion

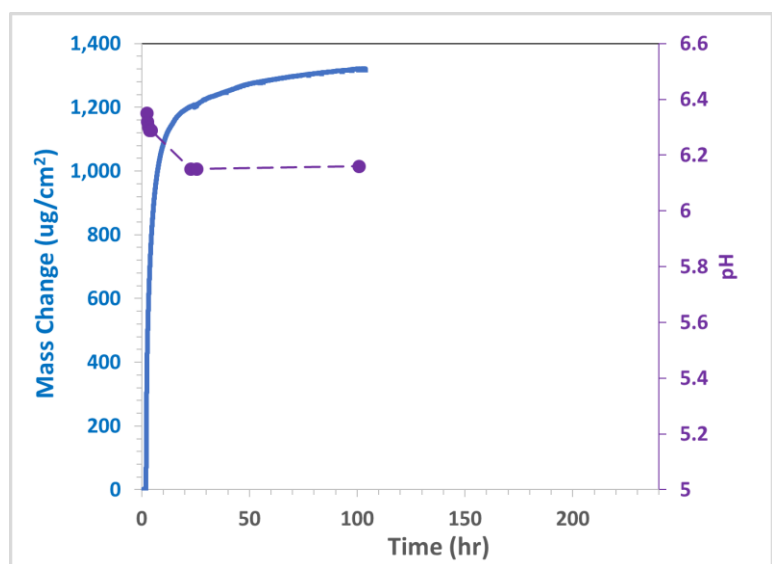
FeCO₃ Layer Formation. The mass change monitored by EQCM is shown in Figure 46. In the first 10 hours, the mass increased quickly from 0 to around 1200 $\mu\text{g}/\text{cm}^2$ due to precipitation of FeCO₃ on the quartz crystal. Some solution (2ml) was taken out of the glass cell for measuring ferrous iron concentration and pH was recorded at the same time. Then, equations (28) and (29) are used to calculate S_{FeCO₃}. As shown in Figure 46, S_{FeCO₃} decreased dramatically from 600 to around 12 in the first 10 hours. Figure 47 shows that pH decreased from 6.4 to 6.2 after FeCO₃ formed.

Figure 46

Mass change (left) and S_{FeCO_3} (right) obtained on Fe-coated quartz crystal in $FeCO_3$ layer formation test at 80°C and 1 wt.% NaCl

**Figure 47**

The pH variation in $FeCO_3$ layer formation test at 80°C and 1 wt.% NaCl



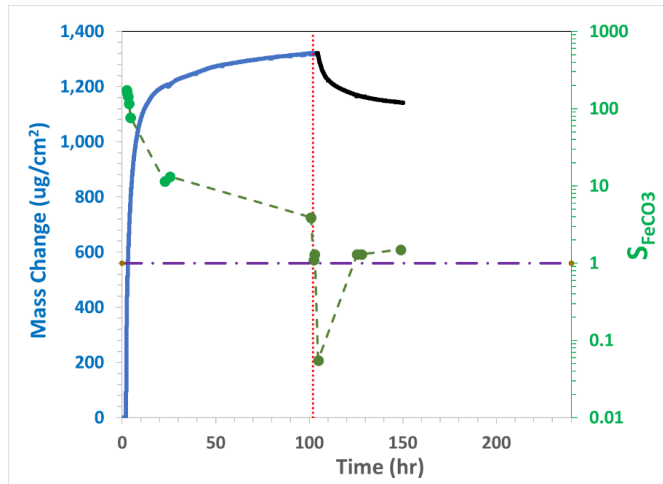
pH Adjustment. As shown in Figure 48, after 100 hours FeCO_3 building, S_{FeCO_3} decreased to 3.9, which is still above 1. Therefore, deoxygenated 1 N HCl was added to the system gradually. The pH and $[\text{Fe}^{2+}]$ was monitored. The mass decreased with adding HCl. Finally, S_{FeCO_3} decreased to 0.055 and no more HCl was added. Meanwhile, as shown in Figure 49, pH dropped from 6.2 to 5.2. When $[\text{H}^+]$ increased, equation (8) switched backwards and carbonate ions were consumed to form bicarbonate ions, and equation (9) also reversed which means FeCO_3 dissolved to produce more carbonate ions to maintain equilibrium of species.

Adding More NaCl. After 24 hours, the mass and pH were stable and S_{FeCO_3} returned to around 1, which means that the system was in near equilibrium condition. Then, more NaCl was added into the system to increase the $[\text{NaCl}]$ up to 10 wt.%. The change of mass and S_{FeCO_3} are shown in Figure 50. The pH decreased from 5.6 to 5.3 immediately, as shown in Figure 51. Mass uptake on the quartz crystal decreased from 1140 to 1070 $\mu\text{g}/\text{cm}^2$ within the first 5 hours, whilst S_{FeCO_3} decreased from 1.5 to 0.1 immediately. After 10 hours, the mass reached a stable value of 1050 $\mu\text{g}/\text{cm}^2$. The pH increased slightly back to 5.4 and S_{FeCO_3} reached a steady value at 0.2. In the following hours until the end of the experiment, the mass, pH and S_{FeCO_3} were all stable, which means the system reached equilibrium.

Surface Morphology. Morphology was characterized by SEM at the end of the experiment. As shown in Figure 52, only prismatic iron carbonate was found.

Figure 48

Mass change and S_{FeCO_3} obtained on Fe-coated quartz crystal with pH adjustment by adding 1N HCl at 80°C. (pH adjusted from pH 6.2 to pH 5.2 at ~100 hours)

**Figure 49**

The pH variation after adding 1N HCl. (pH adjusted from pH 6.2 to pH 5.2 at ~100 hours)

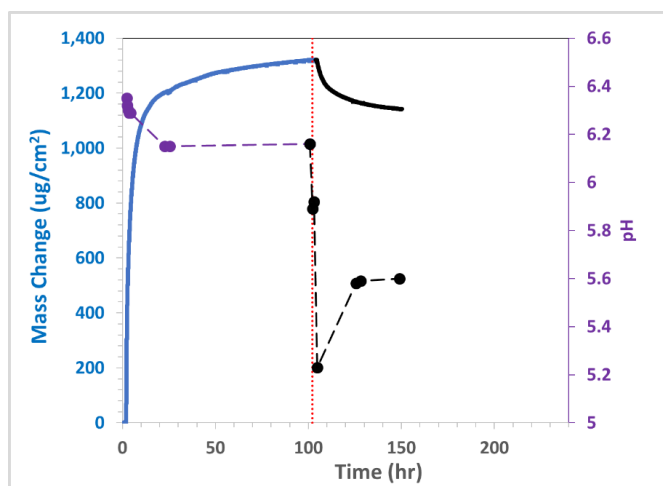


Figure 50

Mass change (left) and S_{FeCO_3} (right) obtained on Fe-coated quartz crystal with adding more NaCl (from 1 wt.% to 10 wt.%) at 80°C. (pH adjusted from pH 6.2 to pH 5.2 at ~100 hours, [NaCl] increased at 150 hours)

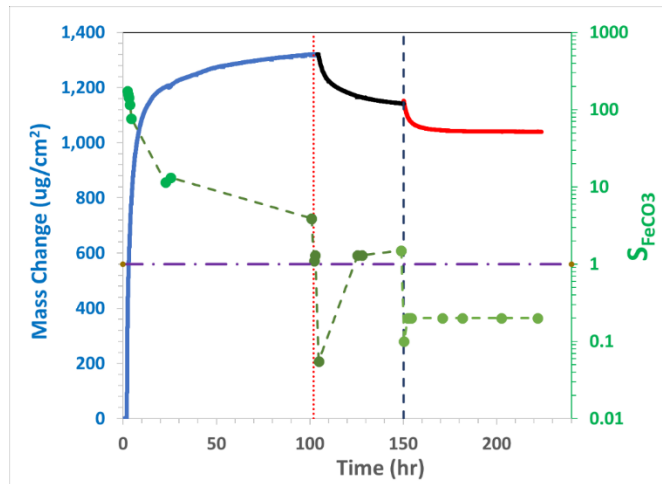
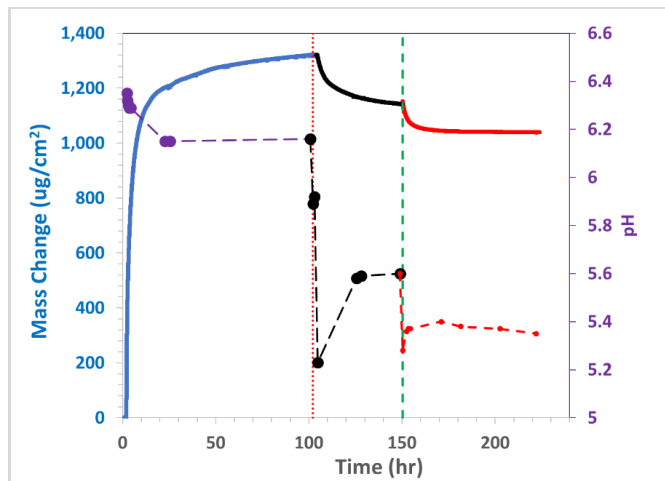
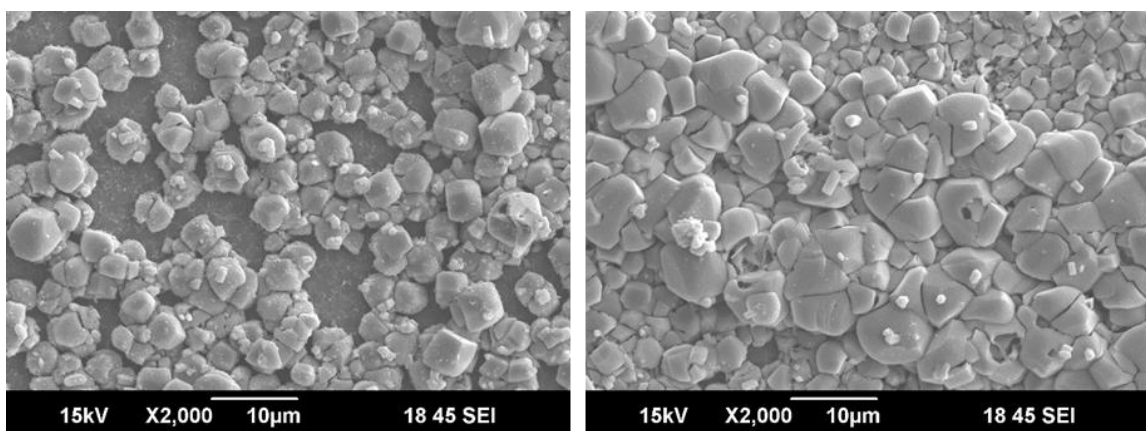


Figure 51

The pH variation on Fe-coated quartz crystal with adding more NaCl (from 1 wt.% to 10 wt.%) at 80°C. (pH adjusted from pH 6.2 to pH 5.2 at ~100 hours, [NaCl] increased at 150 hours)

**Figure 52**

SEM image iron coated quartz crystal at the end of the experiment



5.5 Equilibrium of Iron Carbonate on a Gold Coated Quartz Crystal in High Concentration Salt Solution (with pH Adjustment and Adding NaCl Gradually From 1 wt.% to 25 wt.%)

The previous experiments conducted on iron-coated quartz crystals demonstrated that adding NaCl influenced equilibria associated with CO₂ corrosion. However, since it was an iron-coated crystal, iron also corroded during the experiment. Therefore, when it was in equilibrium, it is difficult to interpret whether iron carbonate formation/dissolution was at steady state or iron corrosion contributed to the observed phenomena. So, in this experiment, a gold-coated quartz crystal was used and NaCl concentration was increased gradually.

In order to simulate iron carbonate precipitation on carbon steel, the gold coated quartz crystal was polarized cathodically to -700 mV. The potential of -700 mV was used because it was close to the corrosion potential of mild steel in CO₂ environments.

5.5.1 Experimental Method

Experimental Setup. The same test setup was used as the previous test in section 5.2.

Experimental Conditions. The experimental conditions for the test of equilibrium of FeCO₃ on Au-coated crystal is shown in Table 7.

Table 7

Experimental conditions for the test of equilibrium of FeCO₃ on Au-coated crystal

Total pressure/bar	1
Sparge gas	CO ₂
Temperature/°C	80
Initial solution pH	6.6
Materials	Polished Au-coated quartz crystal
Stir bar speed/rpm	50
Initial [Fe ²⁺]/ppm	~100
Initial NaCl solution	1 wt.%
NaCl solution	3, 5, 10, 15, 20 and 25 wt.%
Polarization /V vs. Ag/AgCl	-700mV

Experimental Procedure. The detailed test procedure is listed as below.

Steps 1)– 17) were the same as steps 1)-17) in the *Test procedure of Section 5.3.1*,

then:

- 1) Polarize the crystal to -700mV vs. the Ag/AgCl reference electrode.
- 2) Add 1N HCl to adjust pH to make the solution undersaturated with respect to FeCO₃.
- 3) Add 41.60g deaerated NaCl into the glass cell to increase [NaCl] to 3 wt.%, record data until there are no mass changes and FeCO₃ saturation returns to 1.

- 4) Take out specimens of solution periodically from the system and measure $[Fe^{2+}]$ using the HACH spectrophotometer. Record pH at the same time.
- 5) Repeat the procedures of 20) (the quantity of NaCl added refer to Table 1) and 21) for the concentration of 5 wt.% to 25 wt.%.
- 6) Stop the test.

5.5.2 Results and Discussion

Iron carbonate Layer Formation. The mass change monitored by EQCM is shown in Figure 53. In the first two hours, the mass increased quickly from 0 to around $450 \mu\text{g}/\text{cm}^2$ due to precipitation of FeCO_3 on the quartz crystal. Some solution (2ml) was taken out of the glass cell for measuring ferrous iron concentration and pH was recorded at the same time. Then equations (28) and (29) were used to calculate S_{FeCO_3} . As shown in Figure 53, S_{FeCO_3} decreased dramatically from 600 to around 380 with FeCO_3 formation in the first two hours. According to equation (9), CO_3^{2-} was consumed to form FeCO_3 , then reactions (6), (7) and (8) all forwards reacted; thus more H^+ was produced and therefore, pH decreased, as shown in Figure 54.

Figure 53

Mass change (left) and S_{FeCO_3} (right) obtained on a polarized Au-coated quartz crystal in $FeCO_3$ layer formation test at 80°C and 1 wt.% NaCl

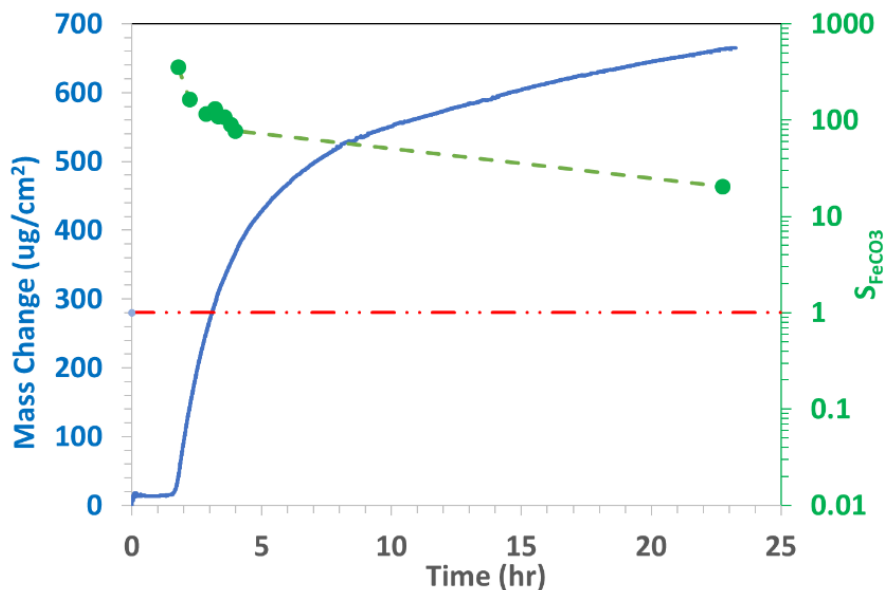
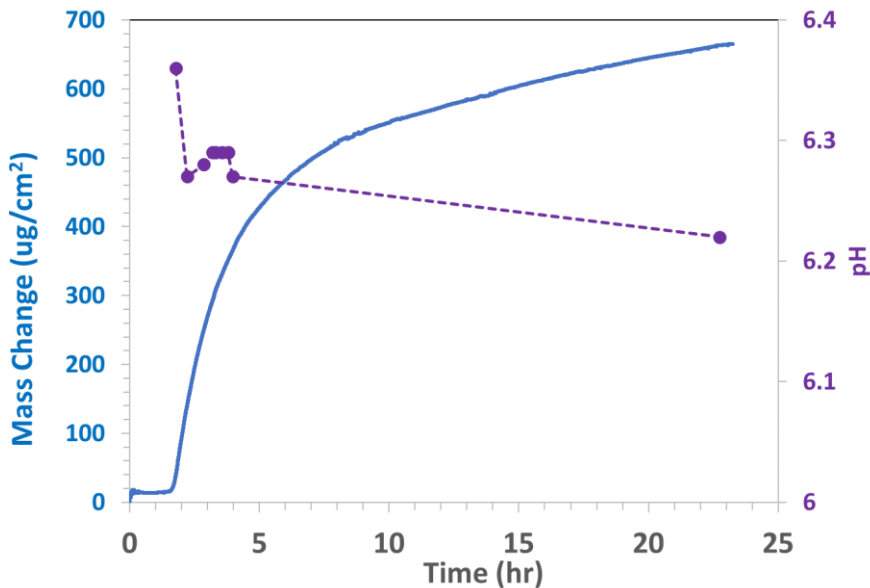


Figure 54

The pH change in FeCO_3 layer formation test at 80°C and 1 wt.% NaCl



pH Adjustment. As shown in Figure 53, after 24 hours FeCO_3 building, S_{FeCO_3} decreased from around 600 to 20, but this value is still much greater than 1. Therefore, in order to make S_{FeCO_3} less than 1, deoxygenated 1 N HCl was added to the system to adjust the bulk pH. The HCl solution was added dropwise. As shown in Figure 55, with addition of HCl solution, the pH decreased immediately, and mass change decreased because part of the iron carbonate dissolved leading to $[\text{Fe}^{2+}]$ increasing. Therefore, S_{FeCO_3} increased slightly, then more HCl solution needed to be added. Finally, when the pH was adjusted to 5.0, S_{FeCO_3} was 0.2, much less than 1. At this point, iron carbonate partially dissolved and produced more $[\text{Fe}^{2+}]$. Then S_{FeCO_3} increased and was stable at 1 after 18 hours. The same phenomenon was observed in Yang's research [25].

Figure 55

Mass change (left) and S_{FeCO_3} (right) obtained on a polarized Au-coated quartz crystal with pH adjustment by adding 1N HCl at 80°C and 1 wt.% NaCl. (pH adjusted from pH 6.3 to pH 5.0 at 22 hours)

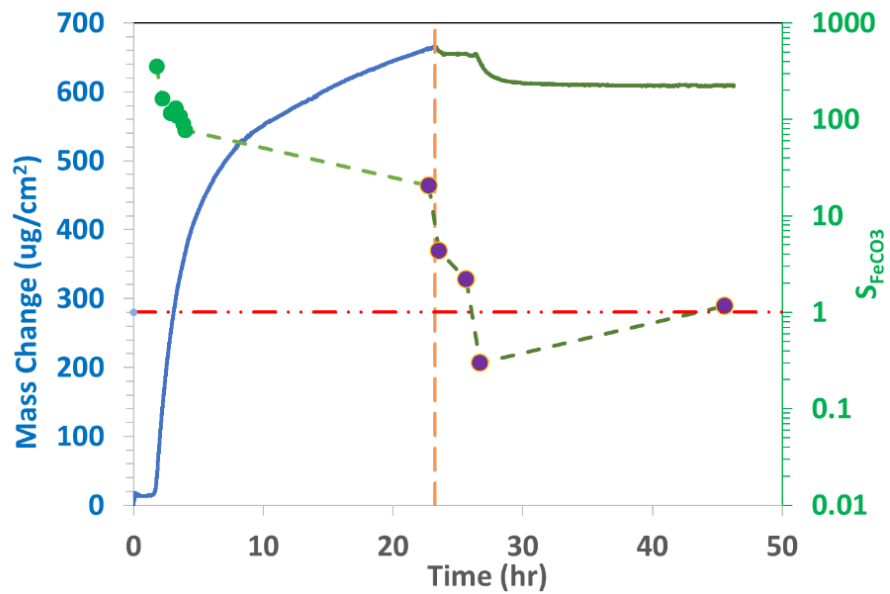
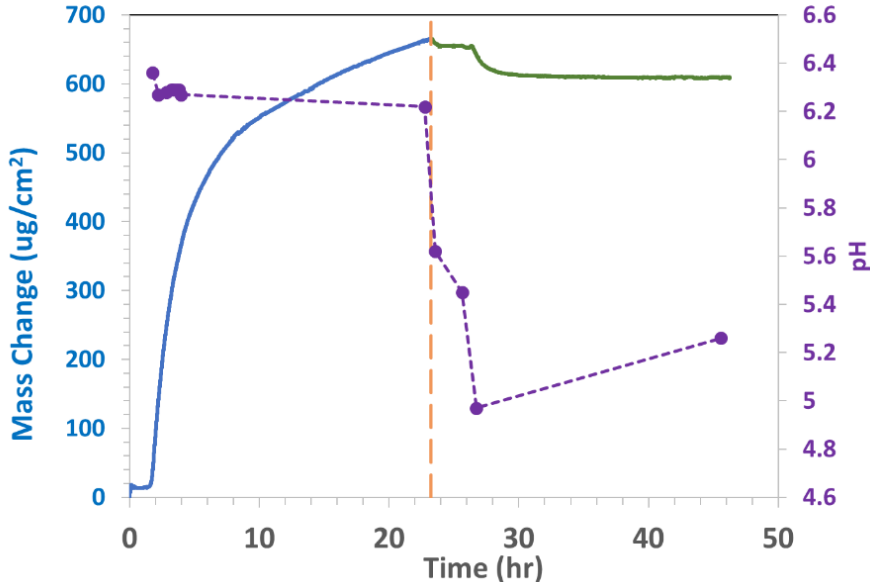


Figure 56

The pH variation on a polarized Au-coated quartz crystal with pH adjustment by adding 1N HCl at 80°C and 1 wt.% NaCl. (pH adjusted from pH 6.3 to pH 5.0 at 22 hours)



Adding More NaCl. After 24 hours, the mass and pH were stable and S_{FeCO_3} returned to 1, which meant that the system reached equilibrium for the previous condition. Then, additional NaCl was added into the system to increase the accumulated [NaCl] to 3 wt.%. The change of mass and S_{FeCO_3} after changing [NaCl] are shown in Figure 57 while the change of mass and bulk solution pH is shown in Figure 58. Upon adding NaCl, the first measurement taken after one hour showed that the EQCM mass decreased only slightly from 608 to 603 $\mu\text{g}/\text{cm}^2$ while the solution pH decreased from 5.26 to 5.18, and S_{FeCO_3} decreased from 1.1 to 0.5. After 5 hours, the EQCM mass remained stable at 603 $\mu\text{g}/\text{cm}^2$. The pH increased slightly to 5.24, which is similar to the

pH value of 5.26 before adding the NaCl; S_{FeCO_3} stayed around 0.6. During the 5 hours after adding NaCl, the EQCM mass, pH and S_{FeCO_3} appeared to be steady, which meant the system reached equilibrium again; not dramatically different from the previous state.

Figure 57

Mass change and S_{FeCO_3} obtained on a polarized Au-coated quartz crystal with adding more NaCl (from 1 wt.% to 3 wt.%). The right graph is the enlarged detail of the left one

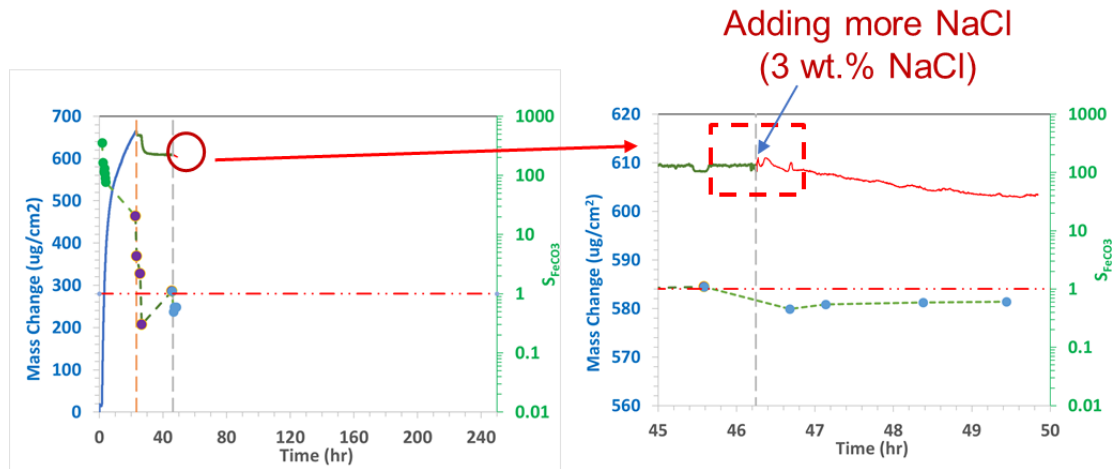
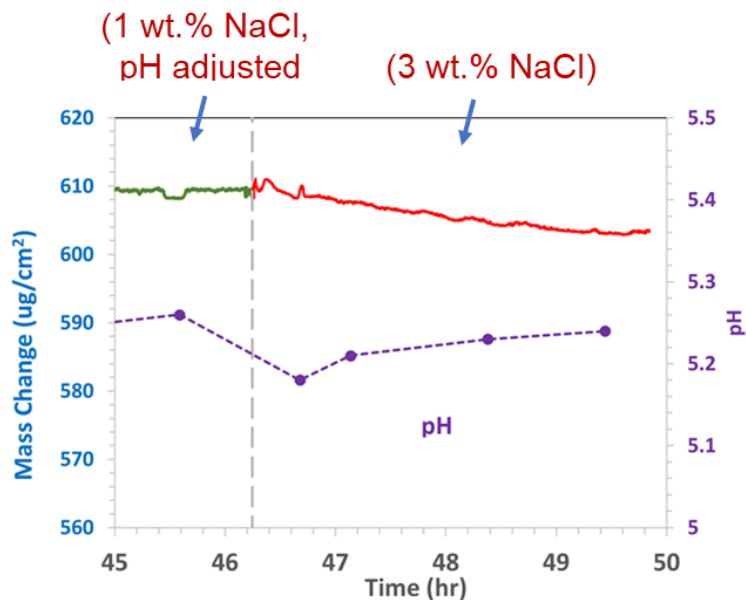


Figure 58

Mass change (left) and S_{FeCO_3} (right) obtained on a polarized Au-coated quartz crystal with adding more NaCl (3 wt.%)



Then, another batch of NaCl was added into the system which increased the accumulated NaCl concentration to 5 wt.%. The subsequent change of mass and S_{FeCO_3} are shown in Figure 59. Mass decreased from 603 to 592 $\mu\text{g}/\text{cm}^2$ (a change of 11 $\mu\text{g}/\text{cm}^2$). S_{FeCO_3} changed from 0.6 to 0.4. The pH barely changed, as shown in Figure 60. After 22 hours, the system appeared to reach equilibrium with the stable mass, pH and S_{FeCO_3} .

Figure 59

Mass change (left) and S_{FeCO_3} (right) obtained on a polarized Au-coated quartz crystal with adding more NaCl (from 3 wt.% to 5 wt.%)

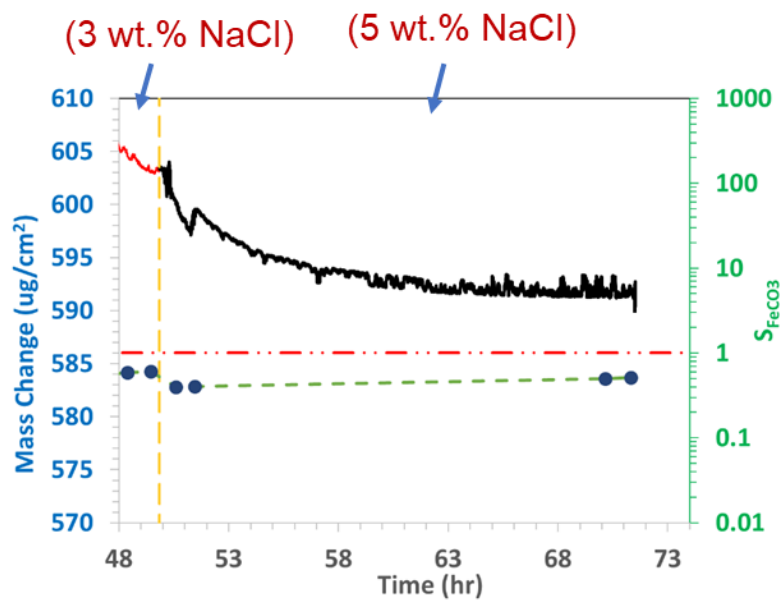
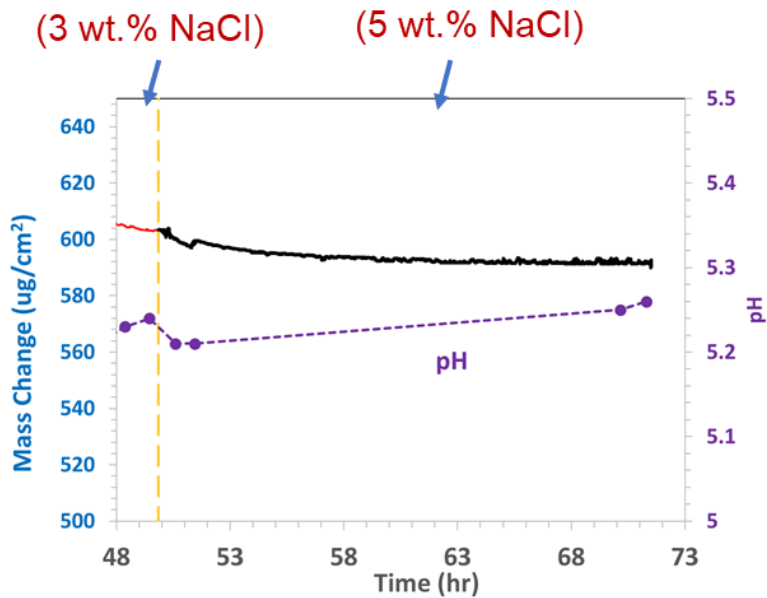


Figure 60

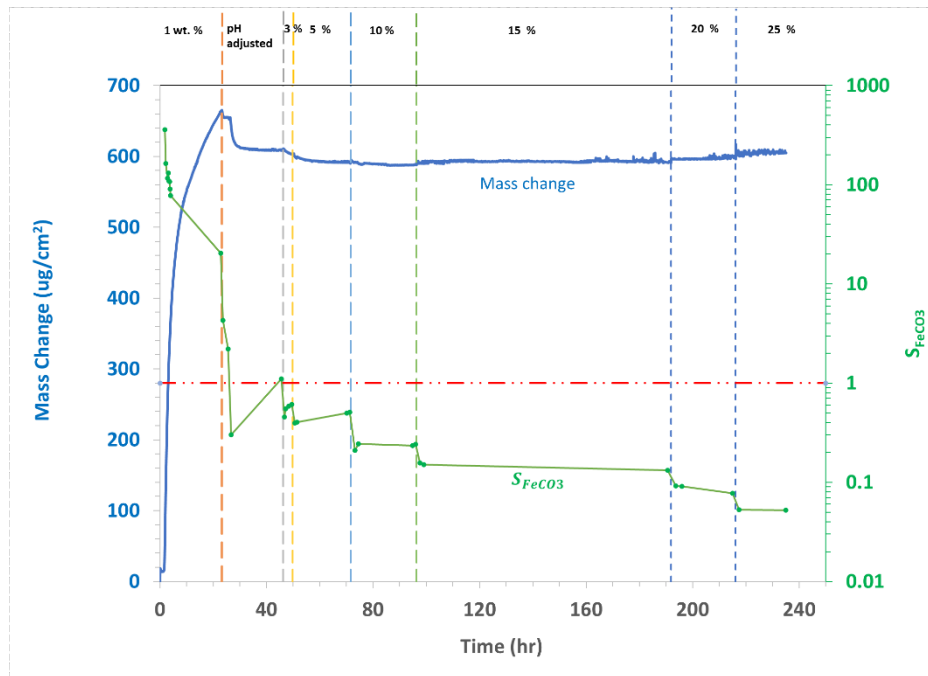
Mass change (left) and the pH variation (right) on a polarized Au-coated quartz crystal with adding more NaCl (from 3 wt.% to 5 wt.%)



The mass change, pH and S_{FeCO_3} change at various accumulated NaCl concentrations are shown in Table 8 and Figure 127 to Figure 134 in Appendix IV. The system recovered to an equilibrium condition for each NaCl concentration. The mass change, pH and S_{FeCO_3} change on a polarized Au-coated quartz crystal for the whole complete experiment are displayed in Figure 61 and Figure 62. It is indicated that mass change had only 0.6% change ($4 \mu\text{g}/\text{cm}^2$ within around 200 hours) from the end of pH adjustment to 25 wt.% NaCl. The pH change shows a downward trend in Figure 62. The possible reason is due to the increase of the activity coefficient of H^+ , leading to higher $[\text{H}^+]$ [71]. This is proven in Chapter 3 that both measured pH and predicted pH from the new model or Li & Duan model reduce with increase of [NaCl].

Figure 61

Mass change (left) and S_{FeCO_3} (right) on a polarized Au-coated quartz crystal for the whole complete experiment

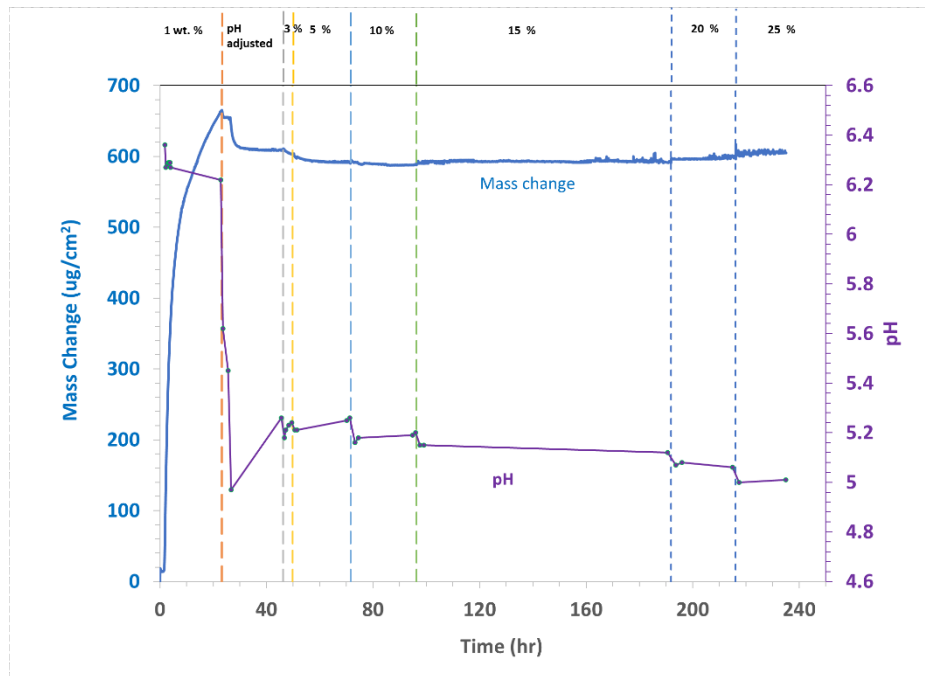
**Table 8**

The mass, pH and S_{FeCO_3} change with more NaCl addition.

[NaCl] wt.%	pH		Mass ($\mu\text{g}/\text{cm}^2$)		S_{FeCO_3}	
	Initial	Final	Initial	Final	Initial	Final
1	6.6	6.2	0	655.8	600	20.4
pH adjustment	4.97	5.26	652.7	608.6	0.3	1.1
3	5.18	5.24	608.6	603.4	0.5	0.6
5	5.21	5.25	603.4	590.4	0.4	0.6
10	5.16	5.20	590.4	589.2	0.2	0.2
15	5.15	5.12	589.2	594.4	0.1	0.1
20	5.07	5.06	594.4	599.6	0.1	0.1
25	5.00	5.01	599.6	604.9	0.04	0.04

Figure 62

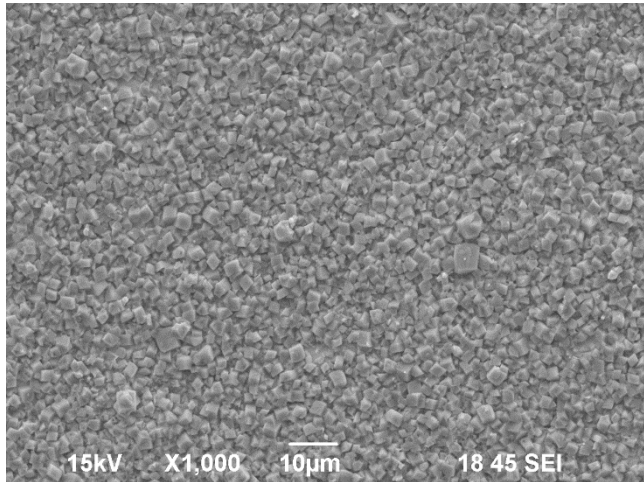
Mass change (left) and the pH variation (right) on a polarized Au-coated quartz crystal for the whole complete experiment



Surface morphology. Morphology was characterized by SEM at the end of the experiment. As shown in Figure 63, only prismatic iron carbonate was found. The iron carbonate still looked dense.

Figure 63

SEM image of iron carbonate layer formed on polarized (-700mV) Au-coated quartz crystal at the end of the experiment



5.6 Modelling

5.6.1 New Model Proposed

The tests on a polarized Au-coated quartz crystal in non-ideal solution showed the calculation of saturation value, S_{FeCO_3} , to be much less than 1 (highly undersaturated). However, there was no significant change in the mass of precipitated $FeCO_3$ on EQCM which should have occurred in an undersaturated solution. Therefore, it was hypothesized that calculation of saturation value was incorrect.

In section 4.5.1, it is discussed that when $S_{FeCO_3} = 1$, the $FeCO_3$ precipitation rate is equal to the dissolution rate and the system is in equilibrium. Therefore, when the system is under the equilibrium conditions, equation(29) can be changed to:

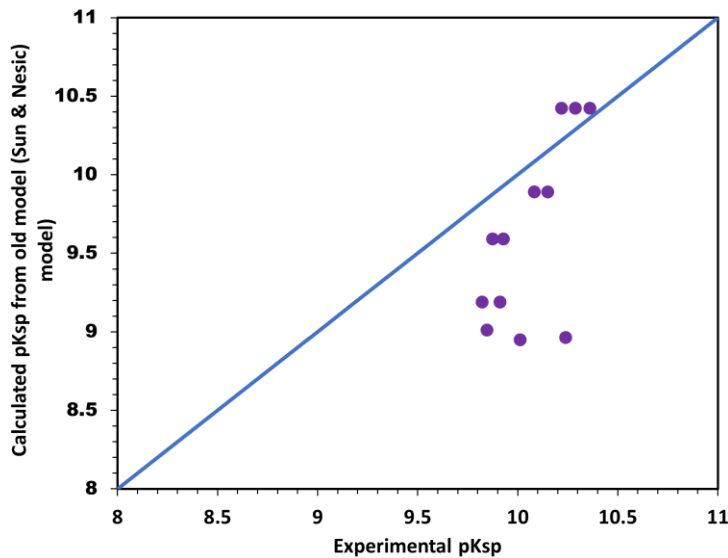
$$K_{sp(FeCO_3)} = C_{Fe^{2+}}C_{CO_3^{2-}} \quad (32)$$

$C_{Fe^{2+}}$ can be measured as described in Appendix I. As discussed in section 3.2 Water Chemistry, pH can be calculated. Since pH can be measured by pH meter, $C_{CO_3^{2-}}$ can be backcalculated by using equations (15) –(23). Then, $K_{sp(FeCO_3)}$ can be calculated by equation 32. This calculated $K_{sp(FeCO_3)}$ is named experimental $K_{sp(FeCO_3)}$.

In all the experimental analysis discussed above, K_{sp} for iron carbonate was calculated according to Sun & Nesic model (equation (28)). When no mass change was observed, the system was in equilibrium and then K_{sp} was calculated according to equation (32). Calculated pK_{sp} from Sun & Nesic model (equation (28), the blue diagonal line) and experimental pK_{sp} (the purple dots) are plotted in Figure 64. Ideally, all the experimental data should fall onto the blue diagonal line. However, the data points deviate from the diagonal line. Therefore, without any changes that have been described in this paper, the model pK_{sp} function does not fit experimental pK_{sp} values.

Figure 64

Parity plot comparison of experimental pK_{sp} vs. calculated pK_{sp} from Sun & Nesic model at 80°C



As part of this research the K_{ca} (equation (27)) from Oddo & Tomson's work was modified to provide a more accurate experimental data fitting for the model and a second water chemistry model based on chemical activity. Therefore, experimental pK_{sp} values were recalculated using equation (28) with $[CO_3^{2-}]$ determined using the new K_{ca} (equation (27)). The modeled pK_{sp} was still calculated according to equation (28). Both recalculated experimental and modeled pK_{sp} are plotted in Figure 65. The modeled pK_{sp} now fits the recalculated experimental pK_{sp} better but can still be improved further. By making slight changes to the constant and the coefficients for ionic strength from equation (28), the best fit line for experimental pK_{sp} was determined to be defined by equation (33) and is shown in Figure 66.

$$pK_{sp} = 59.08 + 0.041377T_K + \frac{2.1963}{T_K} - 24.5724 \log T_K - 2.01I^{0.5} + 0.59I \quad (33)$$

Figure 65

Parity plot comparison of experimental pK_{sp} vs. calculated pK_{sp} from the new model with the new K_{ca} at 80°C

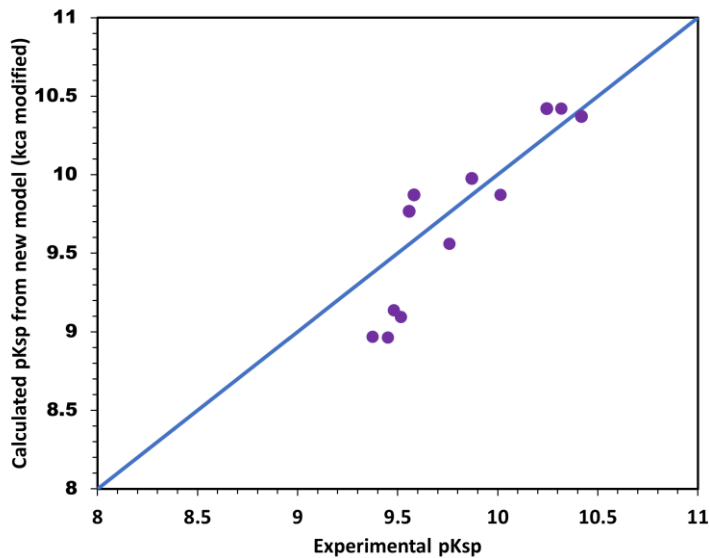
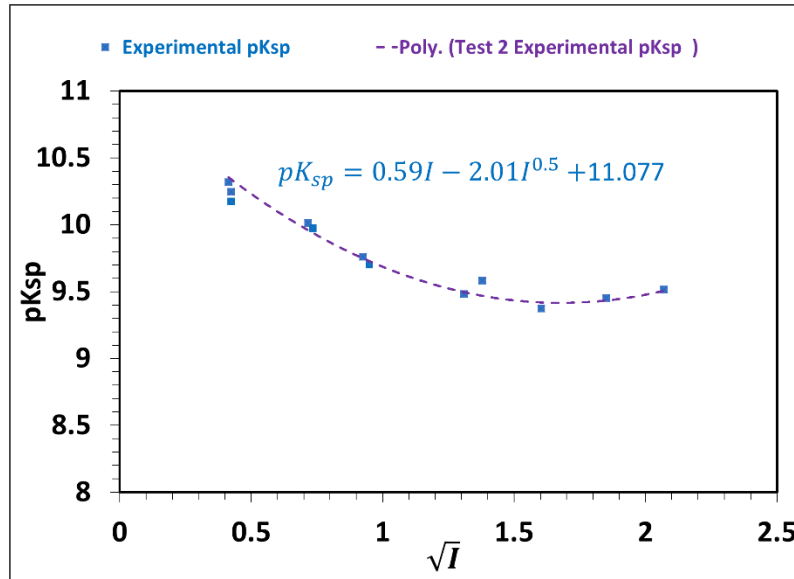


Figure 66

The best fit line for the modified pK_{sp} equation at 80°C

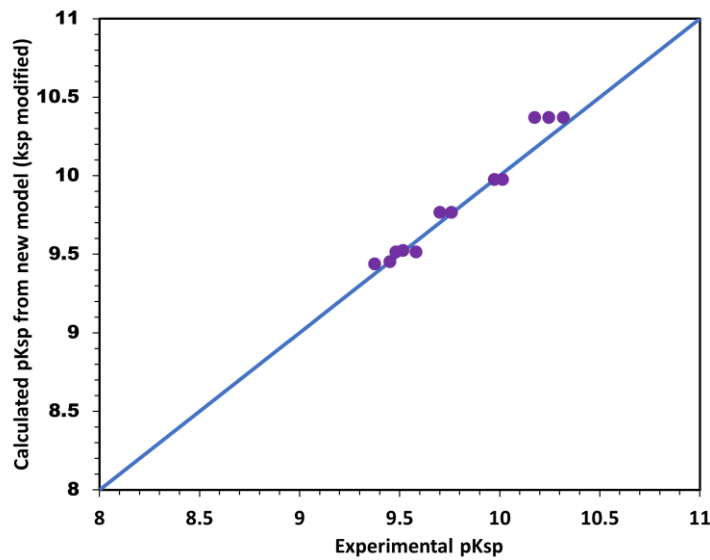


5.6.2 Verification of the New Proposed Model

The experimental pK_{sp} were still calculated using equation (32) with $[CO_3^{2-}]$ determined using the new K_{ca} (equation 27). The model pK_{sp} was recalculated according to equation (33). Both experimental and recalculated model pK_{sp} are plotted in Figure 67. The recalculated model pK_{sp} now fits the experimental pK_{sp} much better.

Figure 67

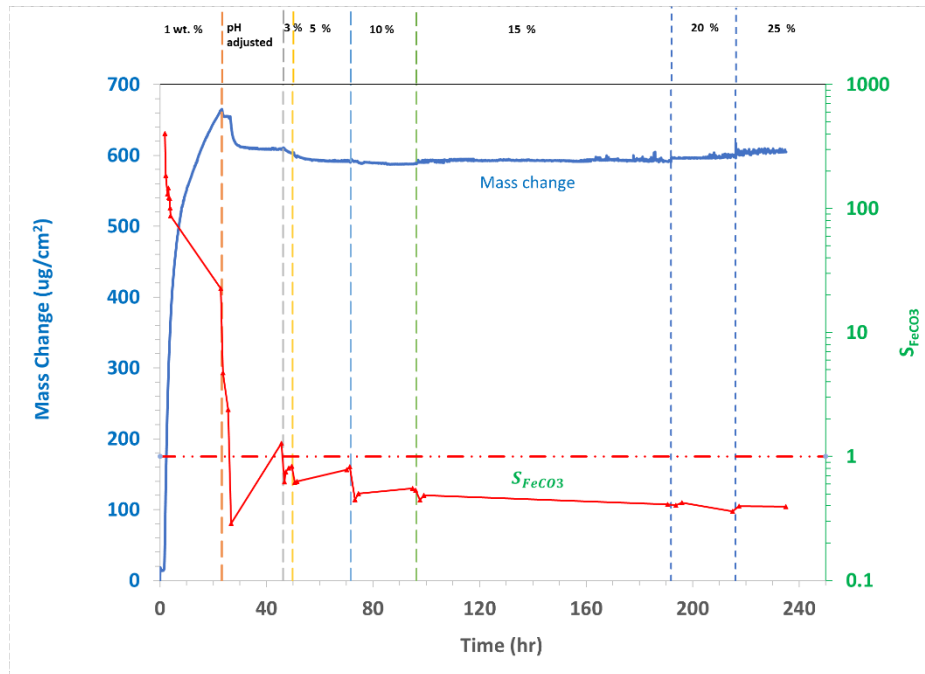
Parity plot comparison of experimental pK_{sp} vs. calculated pK_{sp} from the new model with the new K_{ca} and new K_{sp} at 80°C



Based on the experimental results of the iron carbonate equilibrium in non-ideal electrolytes, the saturation value was plotted in Figure 61. When the system reached the equilibrium condition, the solution's saturation was around 1 at lower [NaCl] (1 wt.%). With the increase of the salt concentration, the solution became more and more unsaturated with respect to FeCO_3 . Based on the K_{ca} modified model (equation (27)), S_{FeCO_3} was recalculated and is shown in Figure 68. Compared to the saturation value calculated by Sun & Nesic model, the recalculated S_{FeCO_3} values were higher but still unsaturated.

Figure 68

Mass change (left) and S_{FeCO_3} (right, recalculated based on K_{ca} adjusted model, equation(27)) on a polarized Au-coated quartz crystal for the whole complete experiment at 80°C

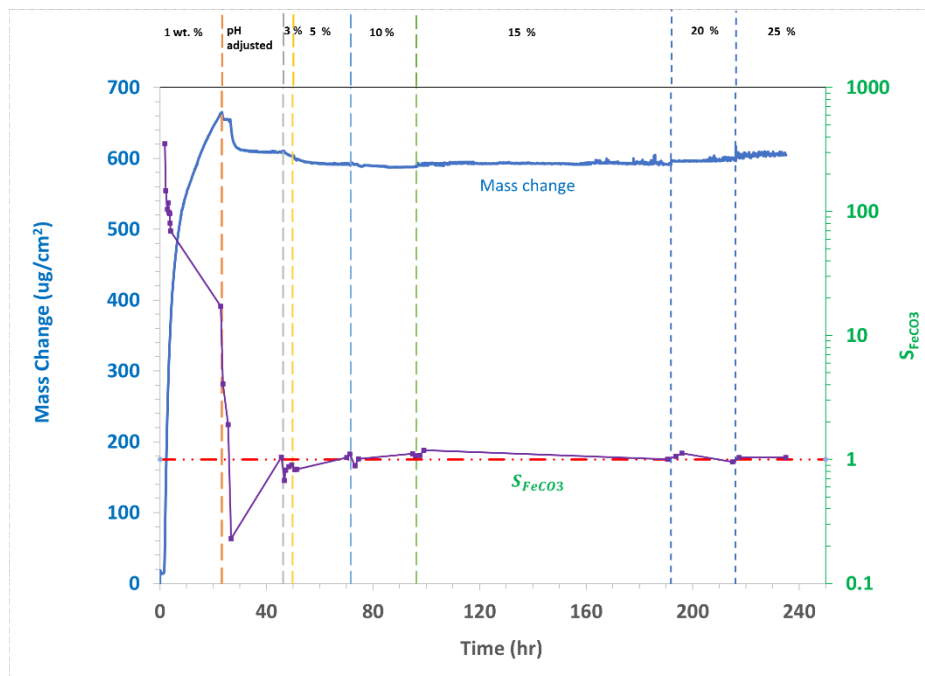


Recalculated S_{FeCO_3} based on the new proposed model (equation(33)) are plotted in Figure 69. First, pH adjustment was made by adding 1N HCl. This caused S_{FeCO_3} to decrease initially, and then go up towards 1 (saturation). Once S_{FeCO_3} reached 1, multiple additions of salt were made to increase the accumulated [NaCl] to 3, 5, 10, 15, 20 and 25 wt.% sequentially. It can be observed that increase of [NaCl] to 3 and 5 wt.% resulted in a small drop in S_{FeCO_3} below 1 (saturation), however, the S_{FeCO_3} went back to 1 within an hour or two. Additional increase in [NaCl] to 10, 15, 20 and 25 wt.% did not result in

a measurable change in S_{FeCO_3} . This is reflected in the very small changes in mass observed from EQCM measurements at 3 and 5 wt.% NaCl.

Figure 69

Mass change (left) and S_{FeCO_3} (right, recalculated based on K_{ca} and K_{sp} adjusted model, equation (33)) on a polarized Au-coated quartz crystal for the whole complete experiment at 80°C



5.6.3 Application of the New Model

In Chapter 3, the effect of salinity on protective $FeCO_3$ layer formation was discussed. Table 9 summarizes the experimental parameters used in those tests. The comparison of the original calculated S_{FeCO_3} (K_{ca} based on equation (22) and K_{sp} based on equation (28) values after adding additional NaCl or NaClO₄ is shown in Figure 70.

For lower concentration of NaCl solution (1 wt.% and 3 wt.%), the FeCO₃ saturation was around 1 for the last several days. But for higher concentrations of salt solutions (10 wt.% and 15 wt.% NaCl, and 21 wt.% NaClO₄), the FeCO₃ saturation was less than 1.

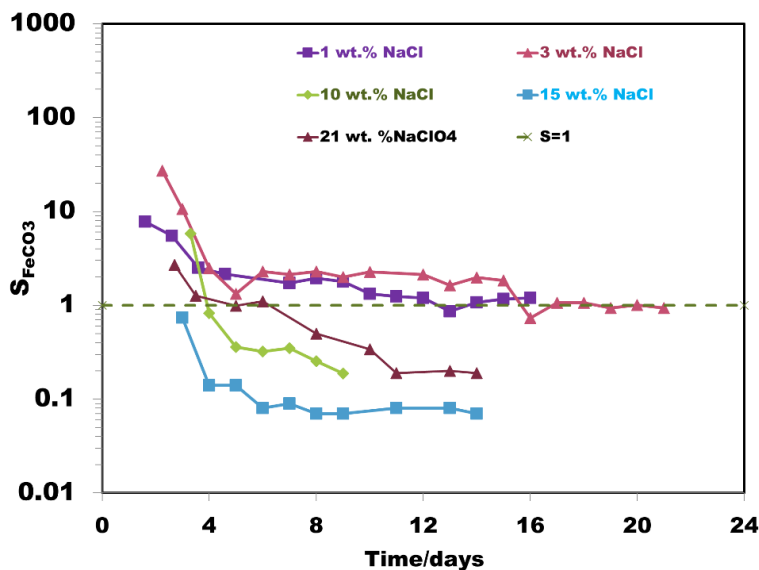
Table 9

The key experimental parameters for tests in Chapter 4

Test name	Salt	Original concentration (wt.%)	Final concentration (wt.%)	Ionic strength
110627	NaCl	0.1	1	0.18
110502	NaCl	0.1	3	0.52
110912	NaCl	1	10	1.74
111105	NaCl	1	15	2.58
111219	NaClO ₄	1	21	1.74

Figure 70

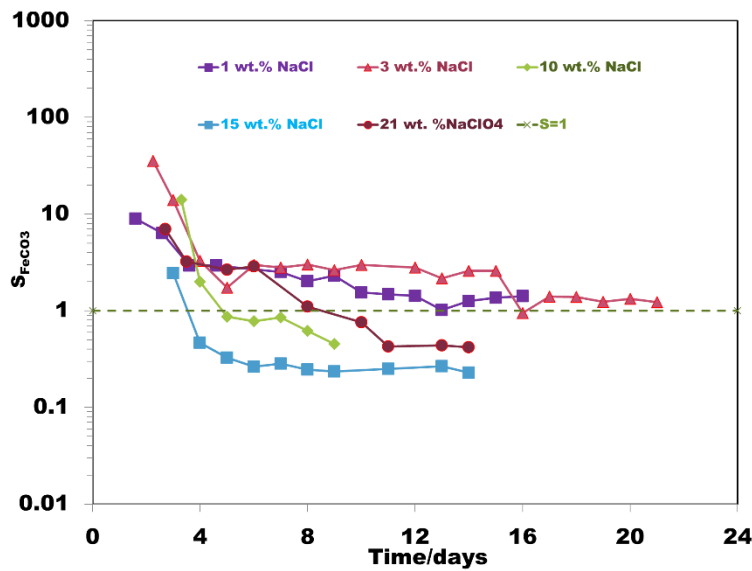
Comparison of the calculated S_{FeCO_3} (K_{ca} based on equation (22) and K_{sp} based on equation (28)) values after adding more salt



Comparison of the recalculated S_{FeCO_3} (K_{ca} based on equation (27) and K_{sp} based on equation (28)) values after adding additional NaCl or NaClO₄ is shown in Figure 71. All the S_{FeCO_3} values were increased.

Figure 71

Comparison of the calculated S_{FeCO_3} (K_{ca} based on equation (27) and K_{sp} based on equation (28)) values after adding more

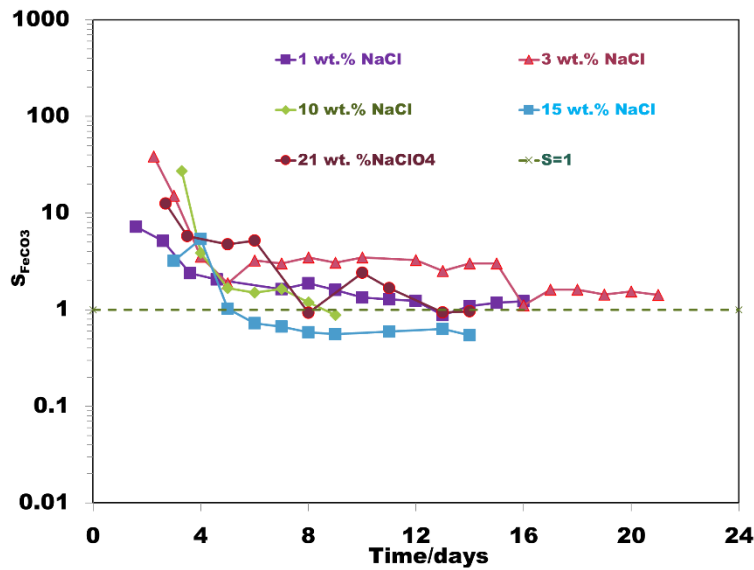


Comparison of the recalculated S_{FeCO_3} (K_{ca} based on equation (27) and K_{sp} based on equation (33)) values after adding additional NaCl or NaClO₄ is shown in Figure 72.

All the S_{FeCO_3} values were increased compared with the calculated S_{FeCO_3} (K_{ca} based on equation (22) and K_{sp} based on equation (28)). It was noticed that all the S_{FeCO_3} values (except for the test with 15 wt.% NaCl) were above 1 at the conclusion of all experiments. And as mentioned in Chapter 4, at the end of the experiments, iron carbonate crystals' size became bigger, indicating that iron carbonate continued growing even after adding more salt. Therefore, S_{FeCO_3} values from the new model coincide with the experiments results.

Figure 72

Comparison of the calculated S_{FeCO_3} (K_{ca} based on equation (27) and K_{sp} based on equation (28)) values after adding more salt at 80°C



5.7 Conclusions

- Added 1N HCl was able to help the system reach equilibrium conditions by dropping the iron carbonate saturation level to below $S_{FeCO_3} = 1$ and so there would be dissolution of iron carbonate to help it achieve equilibrium at $S_{FeCO_3} = 1$ quickly.
- S_{FeCO_3} from the new proposed model reflects the experimental values from EQCM and the previous experiments in Chapter 4 with better accuracy.

Chapter 6: Effect of Acetic Acid on Localized Corrosion Initiation in CO₂ Environments

6.1 Objective

To investigate the influence of the presence of acetic acid (CH₃COOH or shortened to HAc) on localized corrosion in a CO₂ environment and to check whether the initiation could be related to changing the ionic strength of the solution.

6.2 Introduction

As the most prevalent organic acid found in oilfield environments, acetic acid is an important species affecting CO₂ corrosion of carbon steel [2], [4], [47], [72], [73]. As a weak acid, it has a lower pK_a and therefore is stronger than carbonic acid (4.76 vs. 6.35 at 25°C) [47]. When the CO₂ partial pressure is between 0.1 and 1 bar and the concentration of HAc is in the range of 0.1 to 1 mM, acetic acid has the potential to be the main source for supplying reducible hydrogen ions when it is present in aqueous CO₂ systems [48], its dissociation reaction is shown in Equation (14).

Studies relating the role of HAc to an increased corrosion rate in CO₂ environments report different phenomena occurring during the corrosion process. In research reported by Dugstad [72], it was pointed out that corrosion rate and the attack morphology could be dramatically changed by the presence of acetic acid in CO₂ environments. Crolet, *et al.* found that the presence of HAc retarded the anodic reaction [73]. Crolet also stated that FeCO₃ could be dissolved by acetate ions to form more soluble Fe(Ac)₂, which would lead to an increase in general corrosion rate [73].

In studies at the Institute of Corrosion Multiphase and Technology, Fajardo [50] conducted a series of experiments relating to the effect of acetic acid at 80°C and pH 6.3. Her work focused on the effect that HAc had on the iron carbonate layer but did not explore reasons or possibilities for localized corrosion that would occur after the layer was damaged. She did observe and report that partial iron carbonate dissolution occurred due to the injection of acetic acid but did not calculate whether the addition of sodium acetate had a significant influence on the ionic strength of the solution. Under her studied conditions, no localized corrosion was detected. These reported phenomena require some more investigative research and therefore the current set of tests focused on whether HAc can be linked directly with localized corrosion in a CO₂ environment or if a change in ionic strength by the laboratory procedures is a larger contributing factor.

6.3 Hypotheses

- Localized corrosion can be initiated with addition of acetic acid.
- The addition of acetic acid as a buffer solution increases the solution ionic strength, which is the reason for initiation of localized corrosion.

6.4 Experimental Method

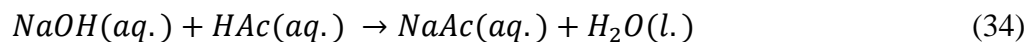
6.4.1 Experimental Setup

A 2-liter glass cell and 3-electrode system was used for each of the experiments, as shown in Figure 13.

6.4.2 Experimental Procedure

The test matrix for the test without HAc is shown in Table 10. The same procedure was used as described in section 4.4.2.

The conditions for the test with HAc are given in Table 11. A buffered HAc solution was prepared in advance. For pH 6.42, 76.8 g NaOH and 96 ml DI H₂O was until the caustic had fully dissolved, this being done in a fume hood. Then, 114 ml glacial HAc was mixed with the above NaOH solution little by little and the solution got warm because of the heat released from the reaction of HAc and NaOH according to equation (34). When the mixed solution got cooler, it was purged with N₂ for 10 minutes. After the protective FeCO₃ layer formed, the mixed solution of undissociated HAc as the buffered solution was injected into the system.



In each test, 3 electrochemical specimens and 5 flat specimens were exposed to the NaCl electrolyte with or without HAc. Flat specimens were removed periodically for surface analysis (shown in Figure 73 and Figure 74).

Table 10

Test conditions without HAc

Electrolyte	1 wt.%NaCl
Temperature (°C)	80
pH (initial)	6.6
CO ₂ partial pressure (bar)	0.53
Fe ²⁺ Added (ppm)	100
Total time (days)	14

Table 11*Test Conditions with HAc*

Solution	1 wt.% NaCl
Temperature (°C)	80
pH (initial)	6.6
CO ₂ partial pressure (bar)	0.53
Undissociated HAc (ppm)	600
Total acetate added	30470 ppm (0.52 M)
Fe ²⁺ Added (ppm)	100
Total time (days)	14

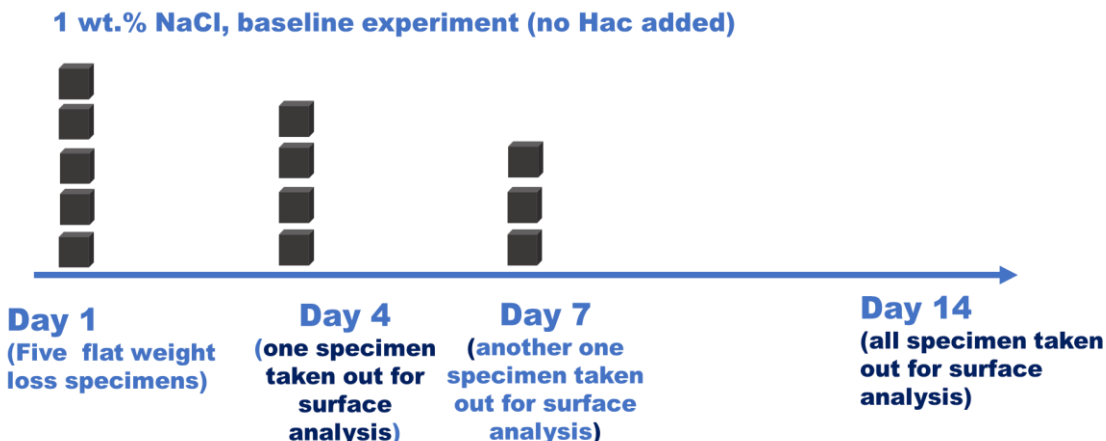
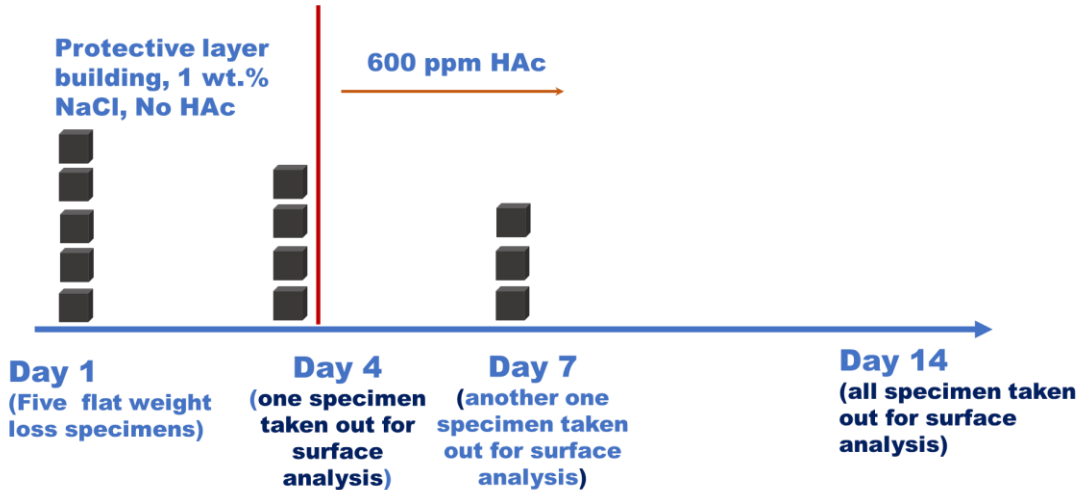
Figure 73*Schematic of periodic removal of flat weight loss specimens for the baseline experiment*

Figure 74

Schematic of periodic removal of flat weight loss specimens for the experiment with 600 ppm HAc added



6.5 Results

6.5.1 The Baseline Test in NaCl Electrolyte Without HAc

Corrosion Behavior. Figure 75 shows the variation of ferrous ion concentration, pH and FeCO_3 saturation of the test environment with time. The purple line is the S_{FeCO_3} calculated from Sun & Nesic model and the blue line is the S_{FeCO_3} calculated from the new model proposed in Chapter 5. For 1 wt.% NaCl electrolyte, the S_{FeCO_3} calculated from the new model is almost the same as the S_{FeCO_3} calculated from Sun & Nesic model (less than 9% difference). $[\text{Fe}^{2+}]$ decreased from 100 ppm to 4.3 ppm, pH decreased from 6.6 to 6.51, and S_{FeCO_3} decreased from 600 to 17.4 (Sun & Nesic model) within one day.

Figure 76 shows the corrosion rate and corrosion potential changing with time. The corrosion rate decreased from 1.3 mm/yr to less than 0.1 mm/yr due to a protective

layer formed on the surface within two days. Over approximately two days, the corrosion potential increased quickly from -680 mV at the beginning to the maximum value of -606 mV after 40 hours. The corrosion potential started to decrease afterwards and reached -640 mV after 14 days, which was 40mV higher than the bare steel potential. A pseudo-passive layer probably formed on the surface over the initial two days.

Figure 75

Change of bulk pH, ferrous ions concentration (measured) and iron carbonate saturation (calculated) with time (1 wt.% NaCl and 80°C)

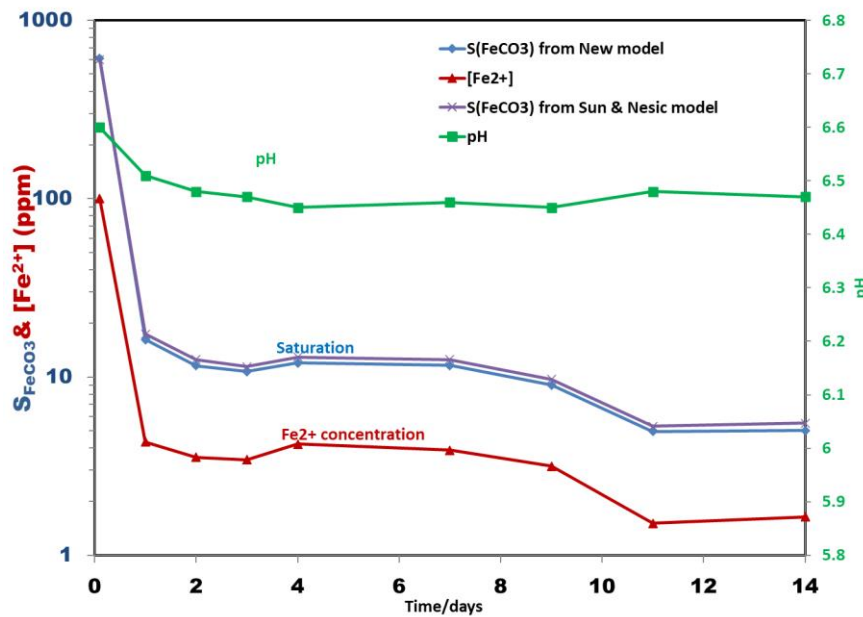
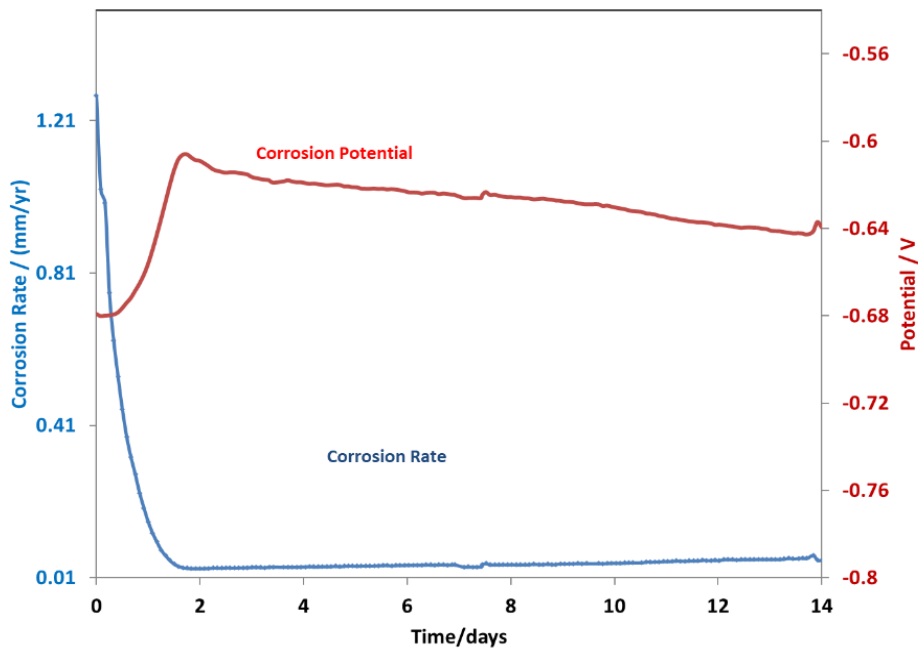


Figure 76

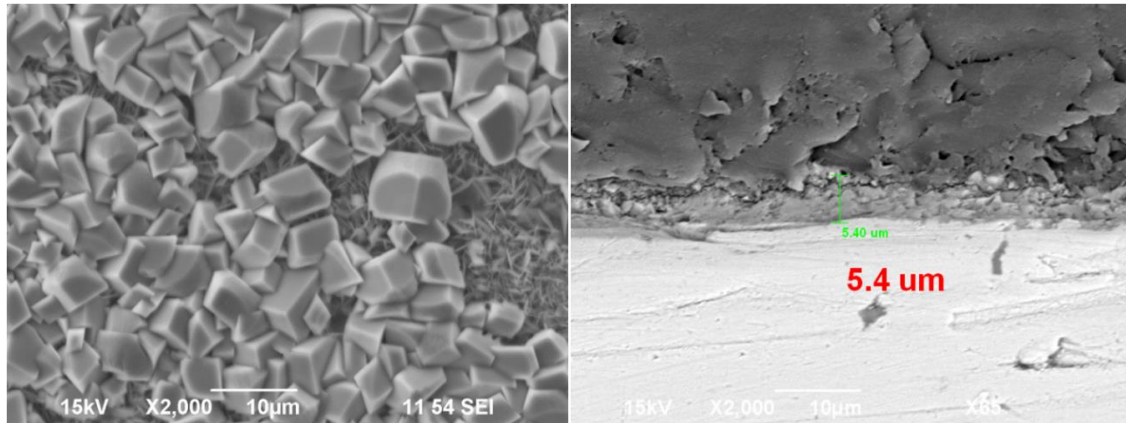
Variation of corrosion rate and potential with test time (1 wt.% NaCl and 80 °C)



Surface Analysis by SEM and XRD. The FeCO₃ morphology after 4 days of the layer building process is shown in Figure 77. Both plate and prism shaped crystals can be observed, although, the prism shaped crystals seem to dominate the surface area covered. The related cross-section of the same specimen indicated that the layer was around 5 µm thick. The XRD analysis, Figure 78, revealed that both FeCO₃ and Fe₂(CO₃)(OH)₂ were detected on the surface.

Figure 77

Surface and cross-section morphologies after iron carbonate layer formation process on day 4 (1 wt.% NaCl and 80°C)

**Figure 78**

XRD results comparison for corrosion product on day 4 and day 14 (1 wt.% NaCl and 80 °C)

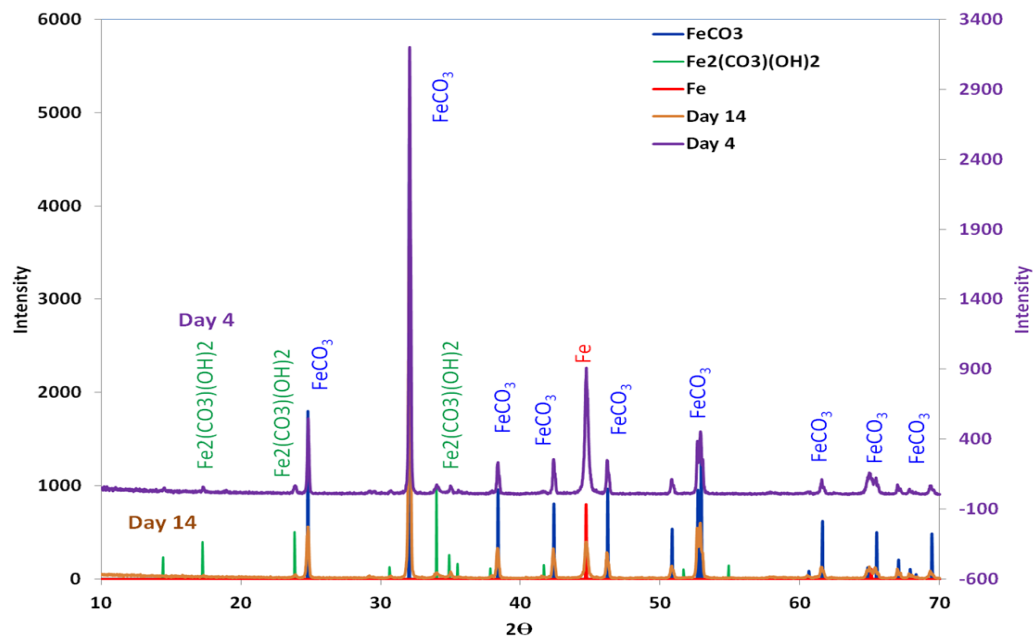
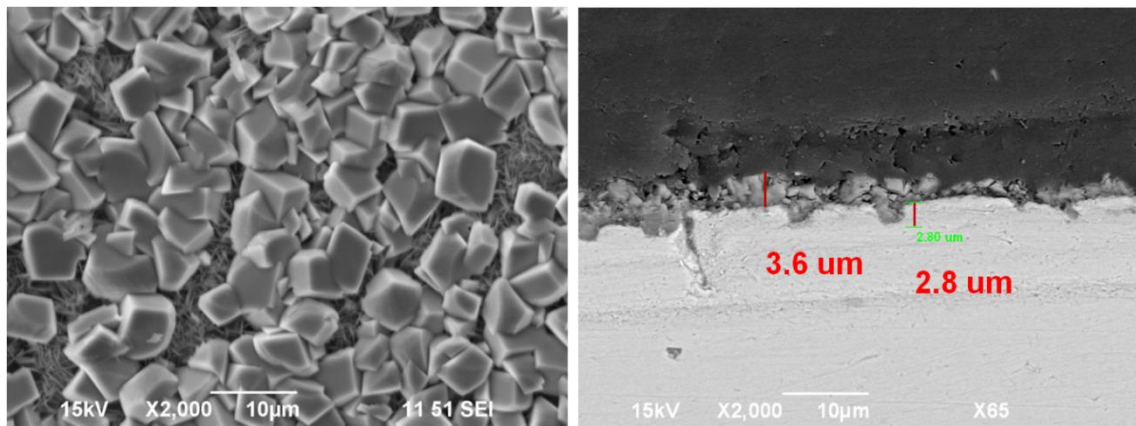


Figure 79 shows the surface morphology after 7 days, which was almost identical to that observed after 4 days. The cross-section shows that the FeCO₃ layer was around 4μm thick.

Figure 79

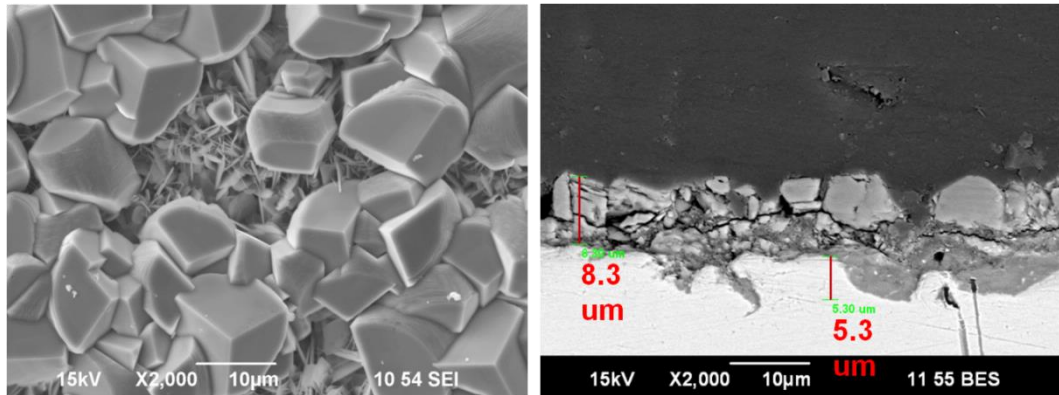
Surface and cross-section morphologies on day 7 (1 wt.% NaCl and 80°C)



On the last day (14 days), all the specimens were removed from the solution, the surface morphology is shown in Figure 80. Both prisms and plates were still observed. Compared what was observed on day 4 and day 7, the crystal size appeared to be larger. The cross-section in Figure 80 shows that the corrosion product layer exhibits a thickness of 8 μm and the shallow pits exhibited a depth of 5 μm. The equivalent pit penetration rate was 0.14 mm/yr. The general corrosion rate was 0.07 mm/yr by weight loss measurement. Therefore, the pitting ratio was 2, less than 3, which indicated that it was still general corrosion. Both FeCO₃ and Fe₂(CO₃)(OH)₂ were still detected on the surface by XRD analysis, see Figure 78.

Figure 80

Surface and cross-section morphologies on day 14 (1 wt.% NaCl and 80 °C)

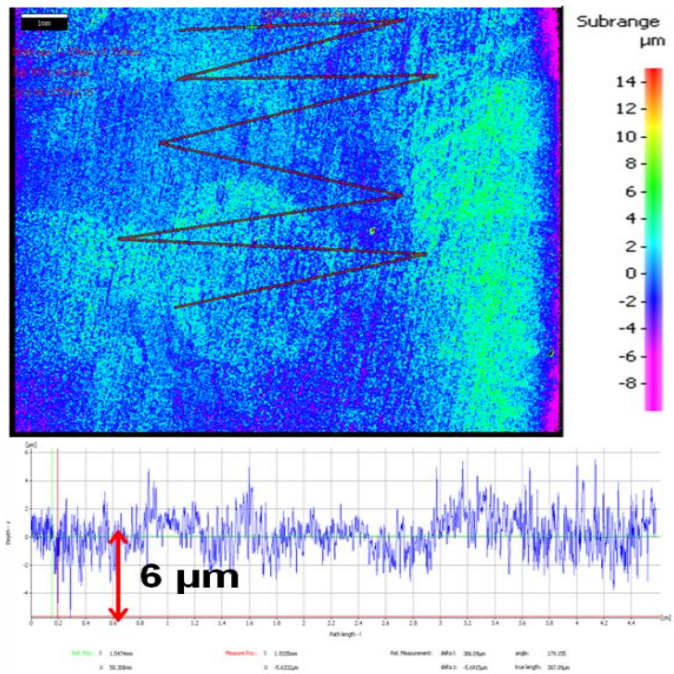


Profilometry Analysis. After corrosion product removal using Clarke solution [64], profilometry data was taken using an infinite focus microscope (IFM); as shown in Figure 81. Several locations were evaluated, and the maximum depth of pitting found was only 6 μm . Based on this depth and the general corrosion rates obtained from weight loss measurement, the pitting ratio was calculated to be 2; therefore, it was still general corrosion and not localized corrosion.

Overall, the high S_{FeCO_3} at the beginning of the experiment helped develop the precipitated iron carbonate layer. The reactions associated with this precipitation (equation (6) – equation (9)) caused a slight drop in the solution pH. The continued decrease in the $[\text{Fe}^{2+}]$ was due to continued precipitation over the remainder of the experiment which was confirmed by the increase in crystal size and low corrosion rate at the end of the experiment.

Figure 81

IFM images and analysis of the corrosion product layer after layer removal on day 14 (1 wt.% NaCl and 80 °C)

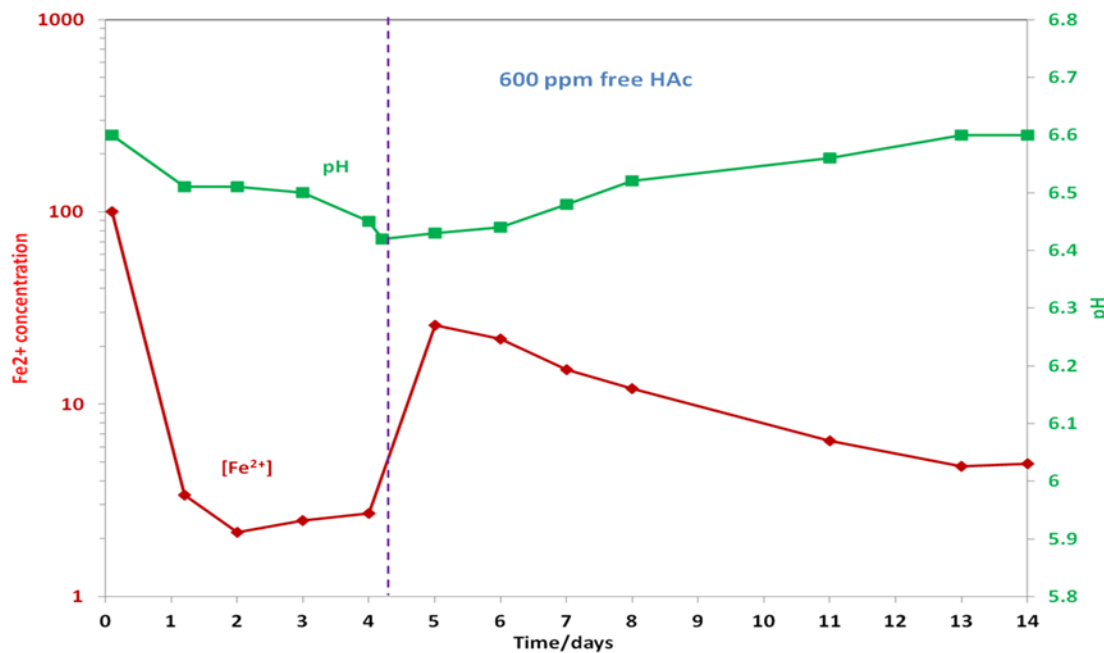


6.5.2 The Test in NaCl Electrolyte with 600 ppm Undissociated HAc

Corrosion Behavior. Trends of the ferrous ion concentration and pH of the system changing with time are shown in Figure 82. At the beginning, the ferrous ions concentration was 100 ppm and after 4 days decreased to less than 3 ppm, which indicated that Fe^{2+} was consumed to form the iron carbonate layer on the steel. The pH decreased from 6.6 to 6.4. After 600 ppm free HAc was added into the system, the iron concentration increased to around 30 ppm immediately, but the pH did not significantly change. Over the following 10 days, the iron concentration decreased, and the pH increased.

Figure 82

Change of bulk pH and $[Fe^{2+}]$ with time (1 wt.% NaCl and 80 °C)



Variation of saturation of $FeCO_3$ with time is shown in Figure 83. It is worth mentioning that the buffered solution increased the ionic strength from 0.2 to 0.9 due to more ions of Na^+ and Ac^- being added into the system. During the first 4 days, the saturation of $FeCO_3$ decreased significantly from 600 to less than 10. After the addition of 600 ppm free HAc, saturation rose to 30 then dropped over the following days. In Figure 83, the purple line is the S_{FeCO_3} calculated from Sun & Nesic model and the blue line is the S_{FeCO_3} calculated from the new model proposed in Chapter 5. The green dashed line shows the S_{FeCO_3} calculated from Sun & Nesic model when the change in ionic strength due to the buffer solution was not considered. It is noteworthy that the

S_{FeCO_3} calculated from the new model is almost the same as the S_{FeCO_3} calculated from Sun & Nesic model when not considering the ionic strength change.

Figure 83

The variation of saturation of $FeCO_3$ with time (1 wt.% NaCl and 80 °C)

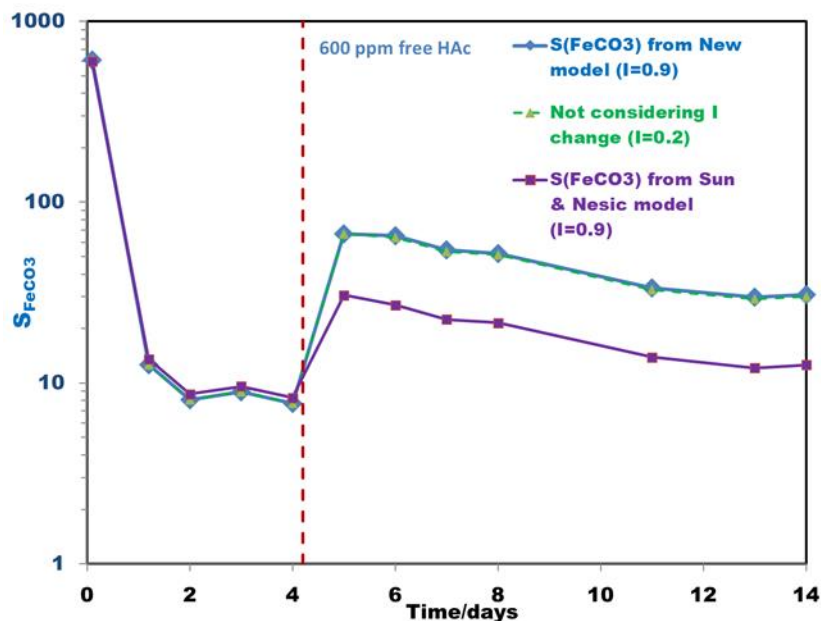


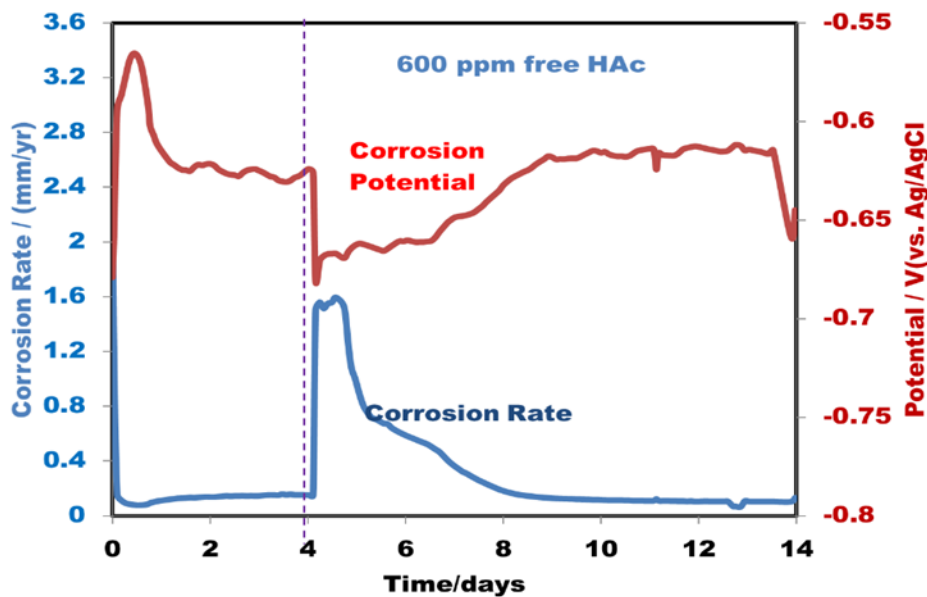
Figure 84 shows the change of corrosion rate and corrosion potential with time.

The initial corrosion potential was -680 mV at the beginning of the test. It increased to a maximum value of -565 mV over approximately one day, which likely resulted from formation of a pseudo-passive layer on the specimen surface. During the same test duration, the corrosion rate was observed to decrease simultaneously which indicated that the pseudo-passive layer was protective; it later returned to a stable value which was still ~ 60 mV above the initial OCP. The corrosion rate declined from 2.3 mm/yr to

approximate 0.1 mm/yr during the first four days. After 600 ppm free HAc was added into the system on day 4, the corrosion rate increased to 1.5 mm/yr and decreased slowly over the following days. The corrosion potential decreased to -680 mV immediately and then returned to its original value over the next few days.

Figure 84

Variation of corrosion rate and potential with test time as determined by LPR measurements (1 wt.% NaCl and 80 °C)

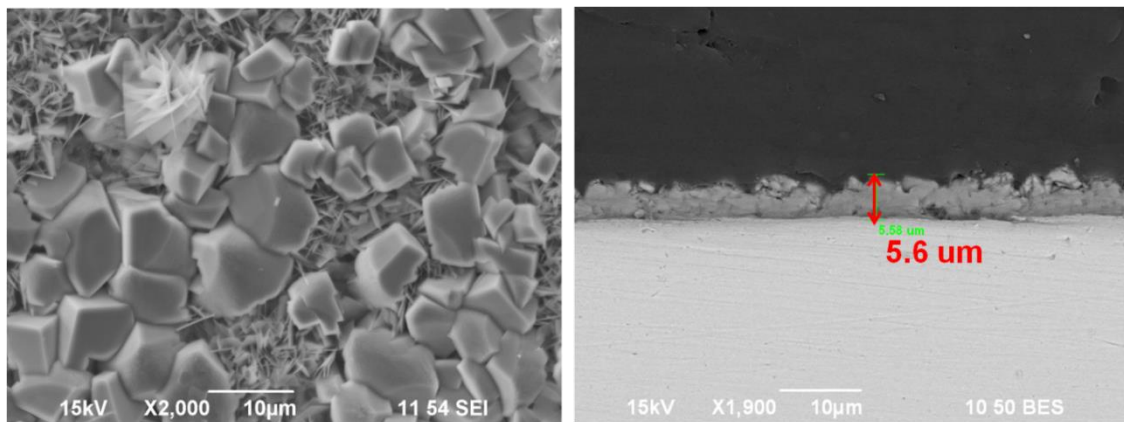


Surface Analysis by SEM and XRD. The layer morphology after 4 days of its building process is shown in Figure 85. It includes both FeCO_3 plates and prisms, which was similar to the one in the previous baseline test in Figure 77. Observation under SEM for the related cross-section indicated that the layer was dense and protective, and

exhibited a thickness of approximately 6 μm . The XRD analysis, as shown in Figure 88, revealed that both FeCO_3 and $\text{Fe}_2(\text{CO}_3)(\text{OH})_2$ were present on the surface.

Figure 85

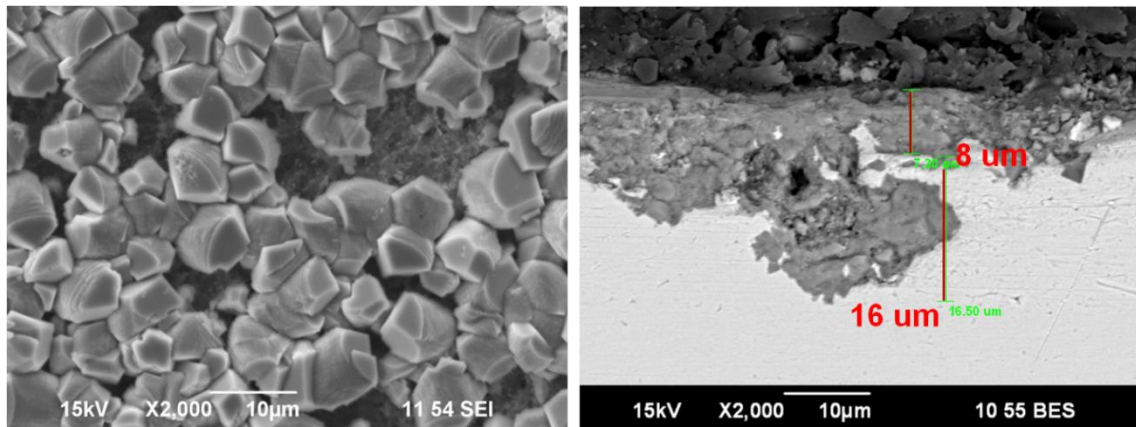
Surface and cross-section morphologies on day 4 (1 wt.% NaCl and 80 °C)



On day 7, another specimen was taken out and the SEM analysis was performed as shown in Figure 86. It can be observed that the surface primarily exhibits prism shaped crystal morphologies. The cross-section in Figure 86b shows that the corrosion product layer was approximately 8 μm while the pits exhibit a depth of 16 μm . By use of this pit depth, the pit penetration rate was determined to be 1.9 mm/yr. The general corrosion rate integrated from LPR was 0.4 mm/yr. Therefore, the pitting ratio was 5, larger than 3, which indicated that it was most likely localized corrosion. XRD analysis only detected FeCO_3 on the surface, as shown in Figure 88.

Figure 86

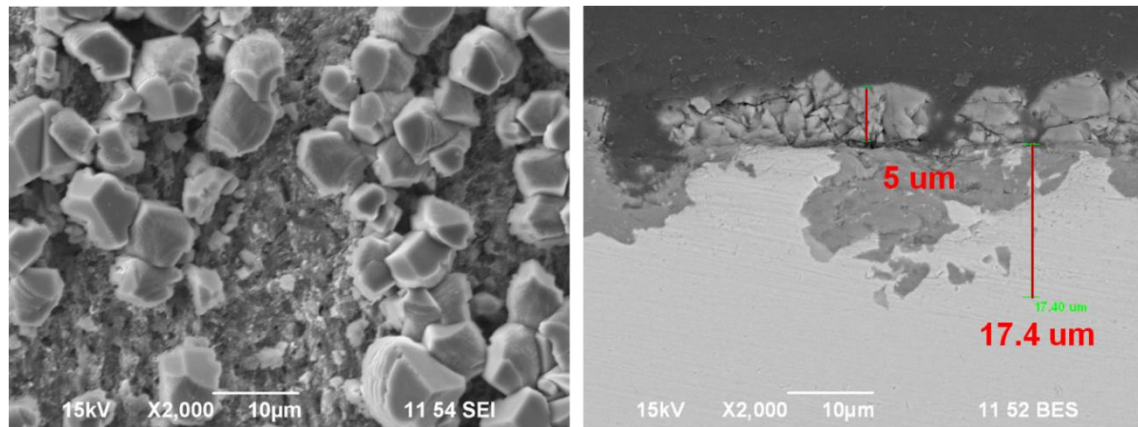
Surface and cross-section analysis on day 7 with HAc (1 wt.% NaCl, 80 °C)



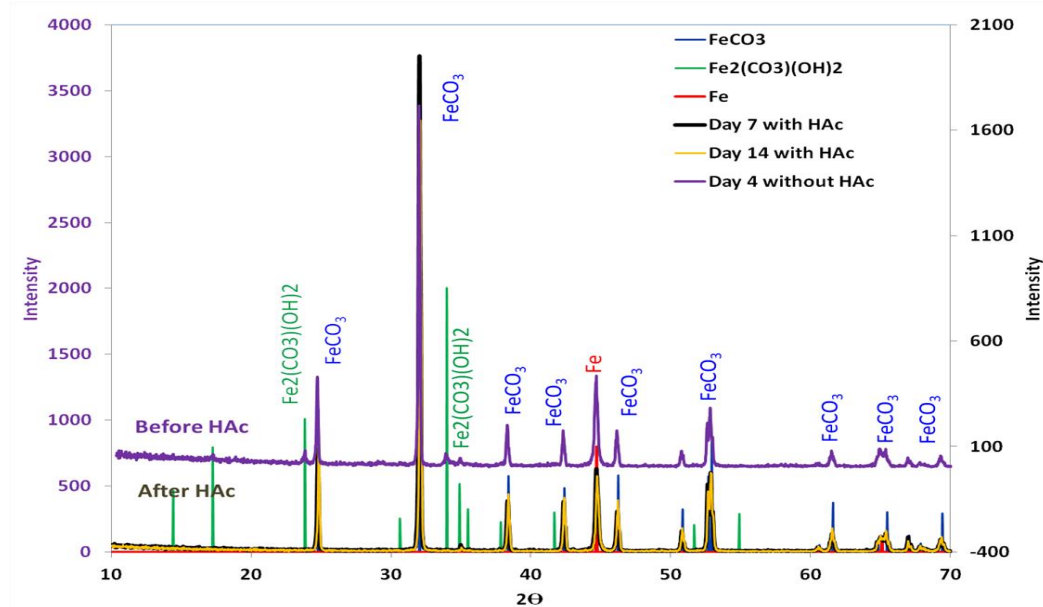
The surface morphology on day 14 is displayed in Figure 87. Compared to the one on day 7 (Figure 86), more bare steel was exposed. Figure 87b shows the cross-section, in which a 17 μm pit was present. Therefore, the pit penetration rate was 0.64 mm/yr , the general corrosion rate from weight loss measurement was 0.14 mm/yr . Thus, the pitting ratio was around 5; as this is larger than 3 this is indicative of localized corrosion. The XRD analysis in Figure 88 revealed that only FeCO_3 was detected on the surface, which was the same as on day 7.

Figure 87

Surface and cross-section analysis on day 14 with HAc (1 wt.% NaCl, 80 °C)

**Figure 88**

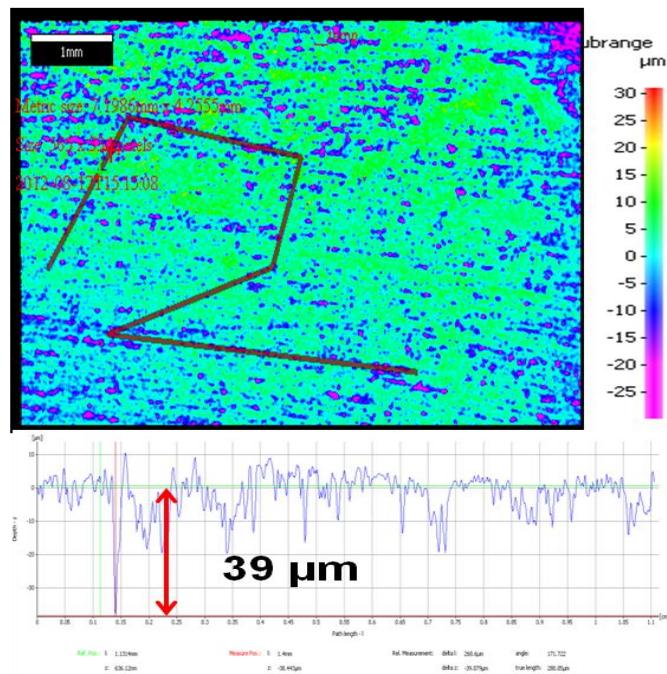
XRD results comparison for corrosion product on day 4, day 7 and day 14 (1 wt.% NaCl, 80 °C)



Profilometry Analysis. After corrosion product removal using Clarke solution [64], profilometry (by IFM) was performed; data from which is shown in Figure 89. The whole surface was scanned, and the maximum depth of pitting was 39 µm, which was equivalent to a pit penetration rate of 1.4 mm/yr. With the general corrosion rates obtained from weight loss measurement of 0.2 mm/yr, the calculated pitting ratio was 7, larger than 3, which indicated that it was localized corrosion.

Figure 89

IFM images and analysis of the corrosion product layer after layer removal on day 14 (1 wt.% NaCl, 80 °C)



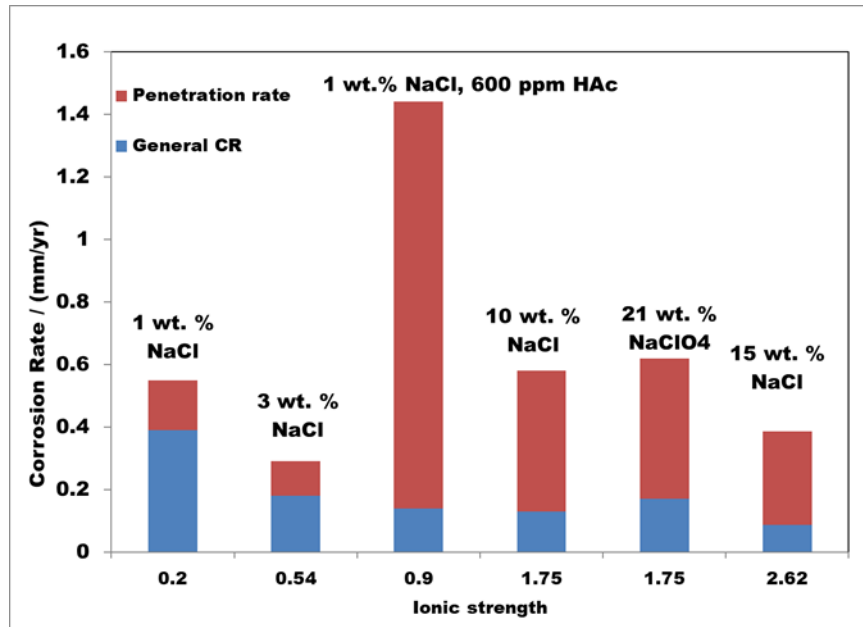
6.6 Discussion

The experimental results indicated that by addition of HAc it is possible to initiate localized corrosion. Since the pH did not change at the beginning, the reason was not the addition of hydrogen ions. It is noteworthy that the ionic strength was increased from 0.2 to 0.9 after the addition of HAc due to more ions of Na^+ and Ac^- being added into the system.

In the previous tests that were performed for various concentrations of NaCl and NaClO_4 solution, it was shown that the increase in ionic strength did not initiate localized corrosion. Figure 90 shows the relationship between when the localized corrosion occurred with respect to the ionic strength, it indicated that the pitting corrosion rate with HAc present far exceeded what was expected if the rate were only influenced by the change in ionic strength. Therefore, it seems that the presence of HAc also had a direct influence on the initiation of localized corrosion. More testing is needed to investigate this.

Figure 90

The relationship between when the localized corrosion occurred with respect to the ionic strength



6.7 Summary

- The presence of acetic acid initiated localized corrosion in a CO₂ saturated environment.
- The addition of a buffered HAc solution increased ionic strength but was not the reason for initiating localized corrosion.

Chapter 7: Localized Corrosion Initiation by O₂ in CO₂ Environments

7.1 Introduction

Little work has been done to study correlation between O₂ and localized corrosion in the presence of iron carbonate in CO₂ environments. An exception is the work of Rosli [74], who studied O₂ effects on the iron carbonate layers in CO₂ corrosion of mild steel under low (1 bar) and high pressure (40 bar and 90 bar). Localized corrosion was found in both low and high pressure. A corrosion mechanism was proposed in her research, which will be discussed later in this chapter.

The other exception is the work of Jiang [43], who studied the effect of 1 ppm of oxygen (0.3 ppm dissolved O₂, calculated according to Appendix III) contamination on CO₂ corrosion in the presence of a FeCO₃ layer. No localized corrosion was detected in Jiang's study. The reason might be that 0.3 ppm dissolved O₂ was not aggressive enough to initiate localized corrosion of mild steel with the presence of a protective FeCO₃ layer.

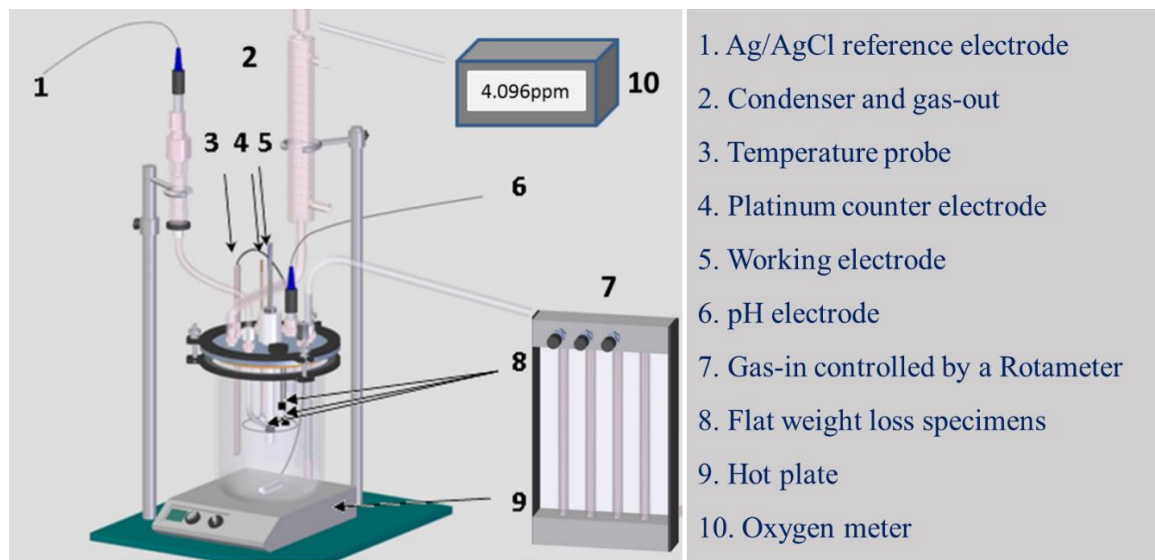
In this research, higher concentrations of 2.5 ppm and 1.4 ppm of dissolved O₂ were introduced to observe how localized corrosion could be initiated by oxygen ingress.

7.2 Experimental Setup.

A 2-liter glass cell and 3-electrode system was used for each test, as shown in Figure 91.

Figure 91

Glass cell setup used to determine the effect of O₂ on localized CO₂ corrosion



7.3 Experimental Procedure

The test conditions are shown in Table 12. A specific procedure to develop a repeatable iron carbonate layer at 80°C and pH 6.6, which was fully described in section 4.4.2 Experimental Procedure. In each of the following tests, a protective iron carbonate layer was first developed on the metal surface. Once the well-developed iron carbonate layer formed, O₂ was introduced into the system to challenge the FeCO₃ layer. Oxygen concentration was controlled by a rotameter (inlet) and measured by an Orbisphere 410 oxygen meter (outlet).

In each test, 2 electrochemical specimens and 5 flat specimens were exposed to the NaCl electrolyte with or without HAc, electrochemical specimens were used for

electrochemical measurements (LPR). Flat specimens were removed periodically for surface analysis (shown in Figure 92 and Figure 93).

Figure 92

Schematic of periodic removal of flat weight loss specimens for 2.5 ppm dissolved O₂ added experiment

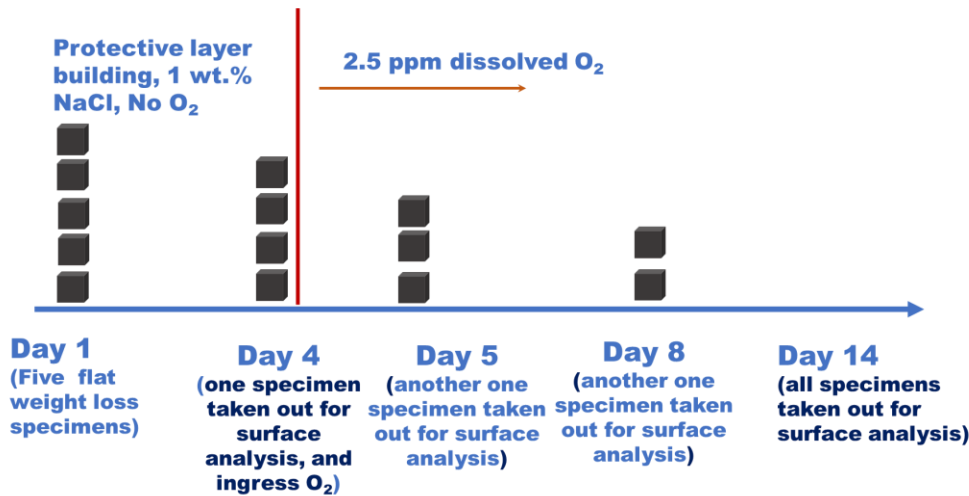
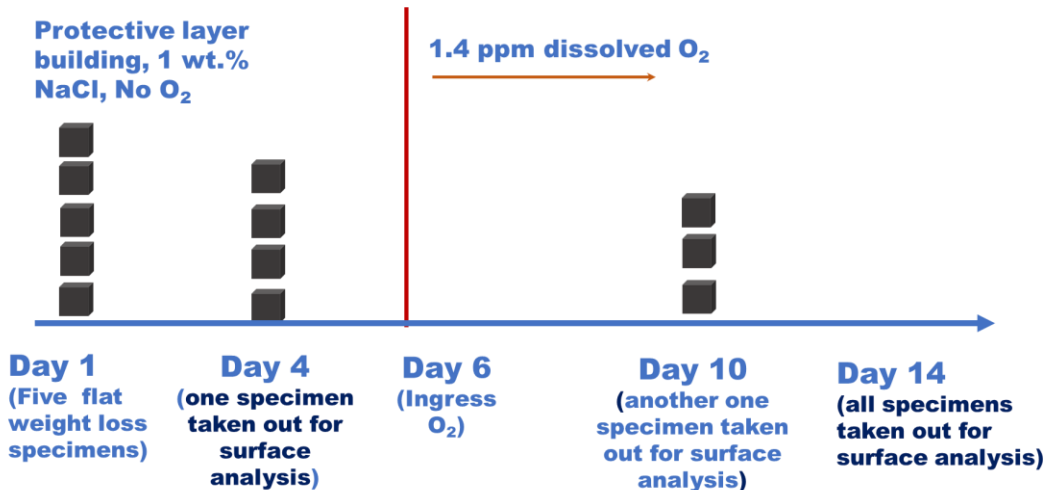


Figure 93

Schematic of periodic removal of flat weight loss specimens for 1.4 ppm dissolved O₂ added experiment

**Table 12**

Test matrix for tests with O₂

Parameter	Description	
Solution	1 wt.% NaCl	
Temperature (°C)	80	
pH (initial)	6.6	
CO ₂ pressure (bar)	0.49	0.43
Fe ²⁺ Added (ppm)	100	
O ₂ concentration (ppm) at the oxygen sensor	4	8
Dissolved O ₂ concentration (ppm) in the glass cell*	1.4	2.5
Total time (days)	14	

* See **Appendix II** for the calculation of the dissolved oxygen concentration in the glass cell

7.4 Results

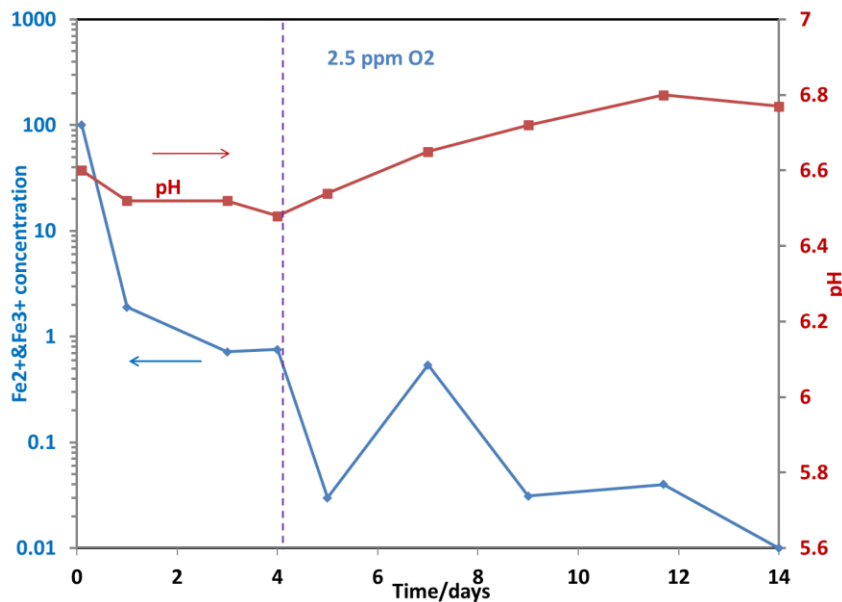
7.4.1 Test with 2.5 ppm of Dissolved O₂

Corrosion Behavior. Figure 94 shows the change of the total iron concentration and pH with time. During the first 4 days, the saturation of FeCO₃ decreased from 600 to 2.7. In the meantime, a decrease from 100 ppm to less than 1 ppm was observed for the concentration of Fe²⁺, which indicated that the iron ions were being consumed to form FeCO₃. The bulk pH had a small change from 6.6 to 6.5. Once 2.5 ppm of dissolved O₂ was introduced into the test at 4 days, the solution became red which meant that ferrous ion was being oxidized to ferric ions, forming iron (III) oxides and oxyhydroxides. The total concentration of iron in solution decreased due to the oxidation of Fe²⁺ by O₂ and the precipitation of iron oxide. The bulk pH increased slowly with time because Fe²⁺ was oxidized by O₂ and ferrous oxide was generated, as shown in reactions (10)-(13).

Figure 94

Change of measured bulk pH (red) and measured ferrous ion concentration (blue) (1

wt.% NaCl and 80 °C), 2.5 ppm of oxygen was continuously added from day 4

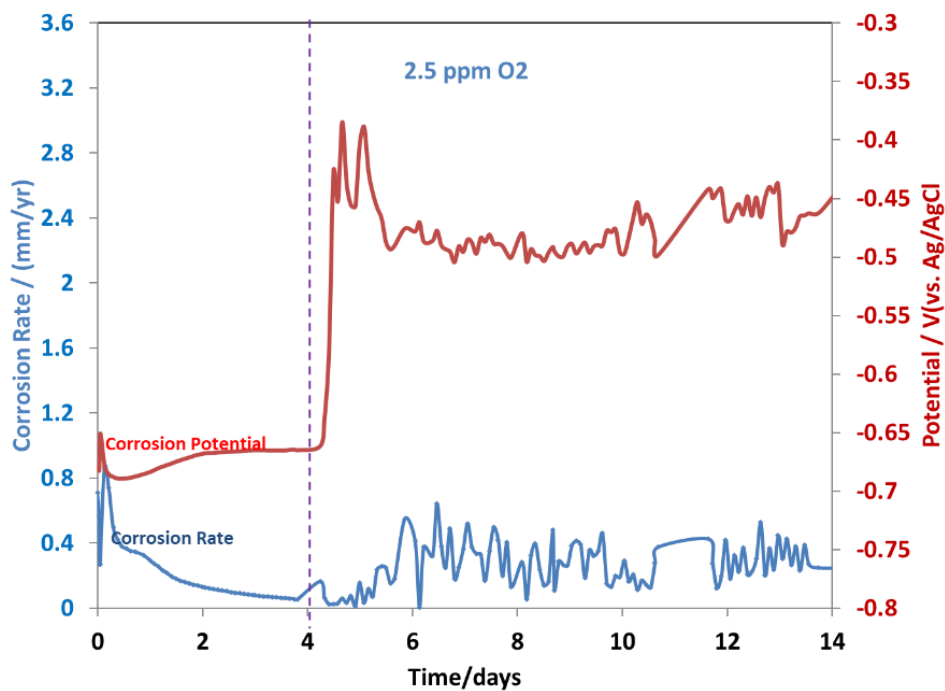


The change of the general corrosion rate and corrosion potential are shown in Figure 95. During the first 4 days, as the iron carbonate layer forms, the general corrosion rate decreased from around 1 mm/yr to 0.06 mm/yr, indicating a protective layer formed. The corrosion potential stabilized at around -660 mV. When O₂ was introduced into the glass cell, the potential immediately increased to around -430 mV. The general corrosion rate increased from 0.06 mm/yr to 0.16 mm/yr, suggesting that the increase in OCP is probably due to enhanced cathodic reaction rate from the increase in dissolved oxygen concentration. In the following days, the corrosion potential stabilized at around -470mV

and the corrosion rate fluctuated at 0.26 ± 0.14 mm/yr, suggesting the corrosion product layer was not protective.

Figure 95

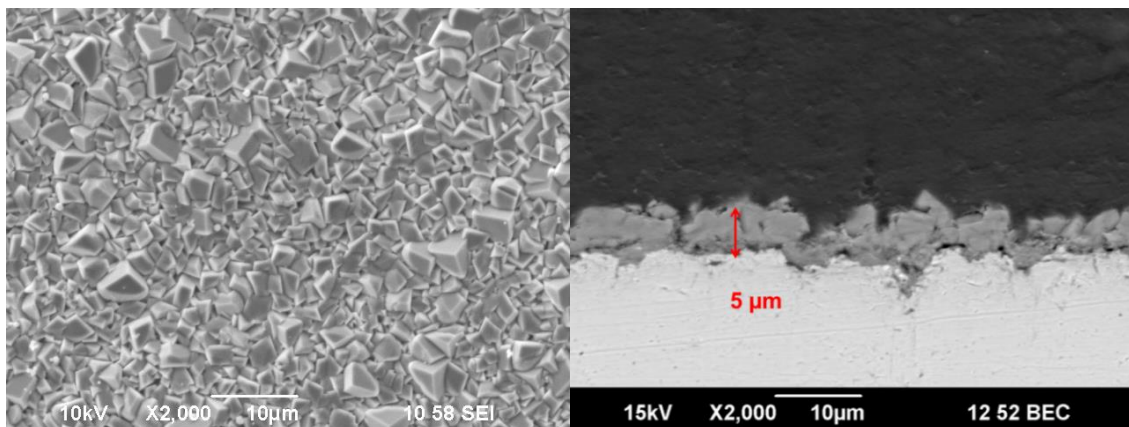
Variation of corrosion rate and corrosion potential with test time as determined by LPR (1 wt.% NaCl and 80 °C), 2.5 ppm of oxygen was continuously added from day 4



SEM Surface Analysis and XRD Analysis. The surface morphology of the layer after 4 days building process is shown in Figure 96. The layer appears dense, compact and covers the surface completely. From the view of the cross-section of the specimen, as shown in Figure 96b, the FeCO₃ layer was uniform and adherent to the metal with a thickness of around 5 µm.

Figure 96

Surface morphology and cross-section after 4 days in 1 wt.% NaCl at 80°C



A specimen was taken out 1 day after 2.5 ppm of dissolved O₂ was introduced. Figure 97 shows the surface morphologies of the specimen at different locations. Although, iron carbonate was still the main crystals, a variety of different morphologies of corrosion products appeared on the surface. In order to identify these corrosion products, measurements with EDS and XRD were conducted and comparisons made using the scientific literature. The corrosion products observed in Figure 97 have similar morphologies as those morphologies of iron oxides or iron hydroxides from the

literatures [75]–[78]. Figure 98 shows the composition analysis by EDS, which revealed that the corrosion product had a high percentage of O and small percentage of C. XRD data (Figure 99) demonstrated that the corrosion products were composed of iron carbonate (FeCO_3), magnetite (Fe_3O_4), hematite (Fe_2O_3) and goethite ($\alpha\text{-FeO(OH)}$). From the cross-section of the specimen illustrated in Figure 100, a penetration with a depth of 15 μm was observed.

Figure 97

Surface morphology after 1 days in 2.5 ppm O_2 (1 wt.% NaCl and 80 °C)

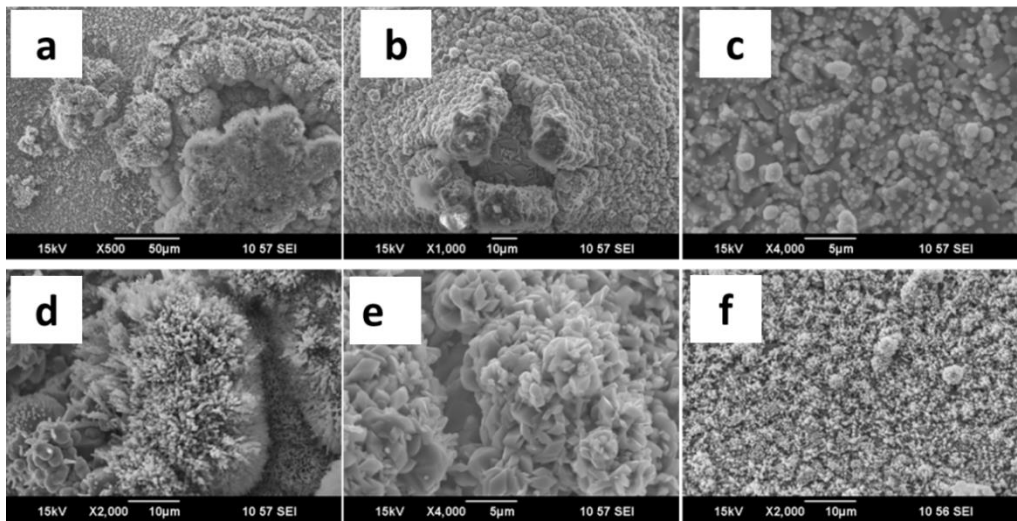
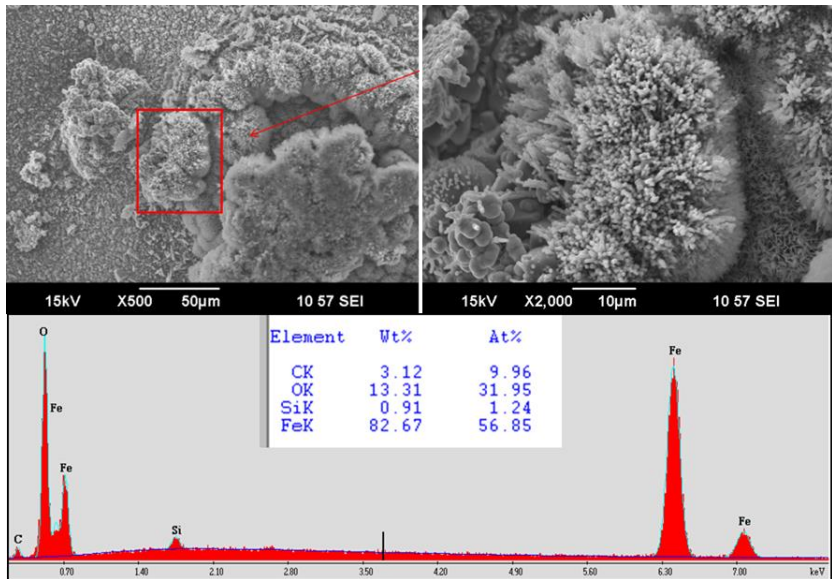


Figure 98

Composition analysis of the corrosion product by EDS after 1 in 2.5 ppm O₂ (1 wt.% NaCl and 80 °C)

**Figure 99**

XRD analysis after 1 days in 2.5 ppm O₂ (1 wt.% NaCl and 80 °C)

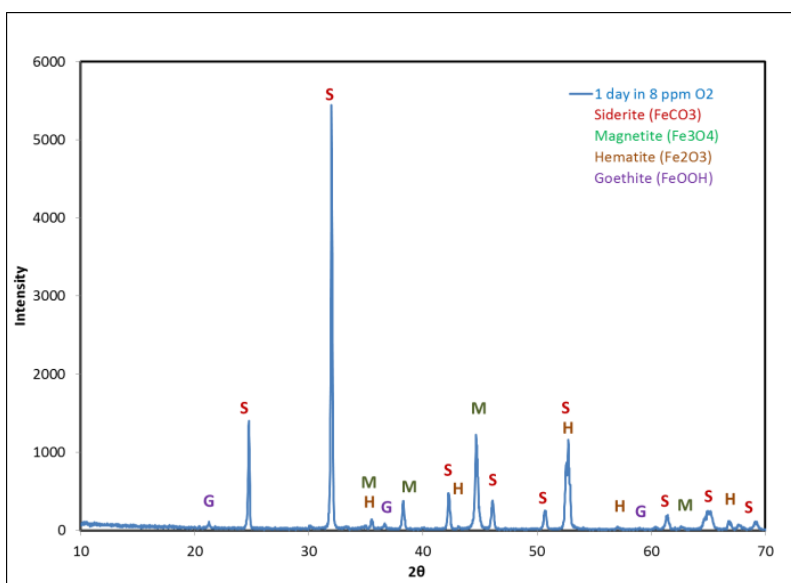
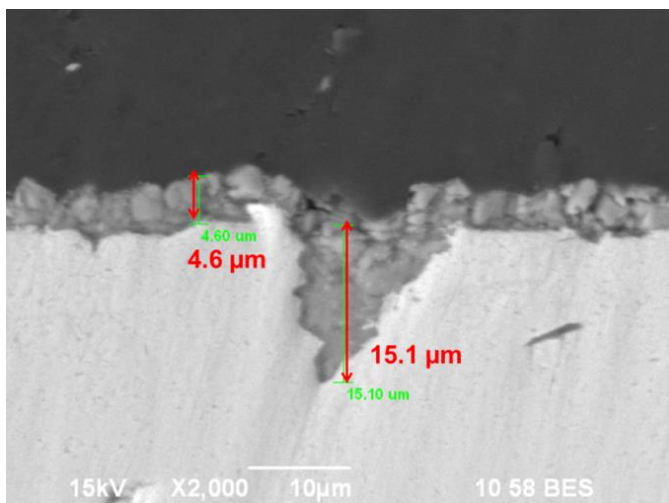


Figure 100

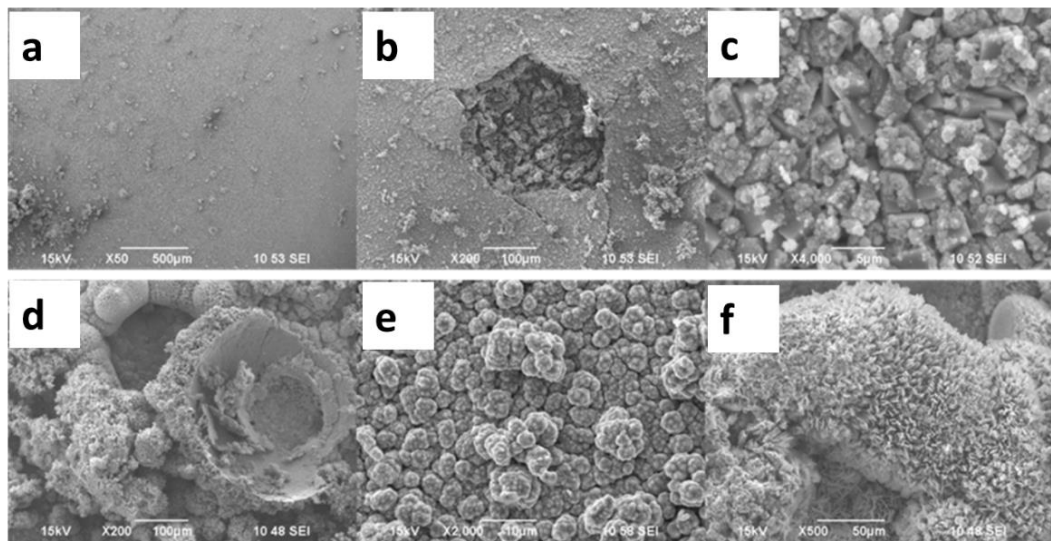
Cross-section after 1 days in 2.5 ppm O₂ (1 wt.% NaCl and 80 °C)



After 2.5 ppm O₂ had been added for 4 days, another specimen was retrieved. The surface morphologies of the specimen are shown in Figure 101. Still, FeCO₃ was the main corrosion product covering the surface. Other differently shaped corrosion products were observed on the metal as well. XRD data proved that the main corrosion product was FeCO₃, and also some amount of magnetite (Fe₃O₄), hematite (Fe₂O₃) and goethite (FeOOH) were detected, as shown in Figure 102. Two layers of corrosion product were observed from the cross-section in Figure 103. The outer layer has more Fe (69 wt. %) and less C (10 wt. %) compared with the inner layer (Fe 54 wt. % and C 18 wt. %), suggesting that the outer layer might be iron oxide, hydroxide or oxyhydroxide and the inner layer could be iron carbonate. It is noteworthy that the FeCO₃ layer on the steel surface was 25.6 μm thick, much thicker than that before the ingress of O₂ (5 μm in Figure 96b).

Figure 101

Surface morphology after 4 days in 2.5 ppm O₂ (1 wt.% NaCl and 80 °C)

**Figure 102**

XRD analysis after 4 days (in 2.5 ppm O₂ (1 wt.% NaCl and 80 °C)

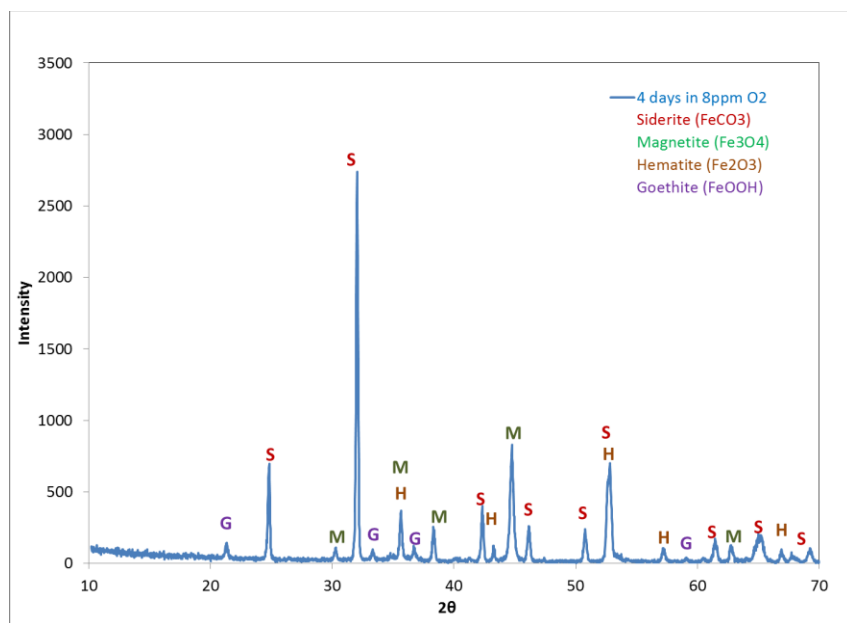
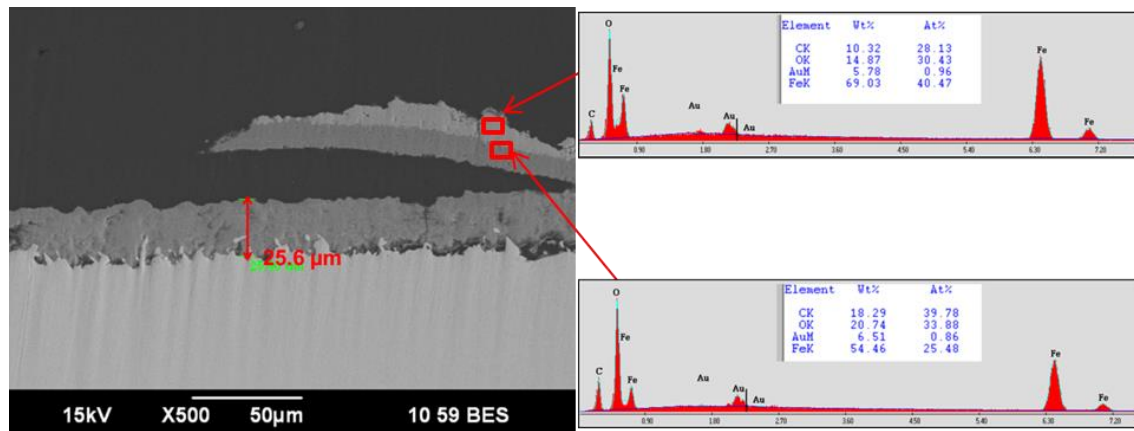


Figure 103

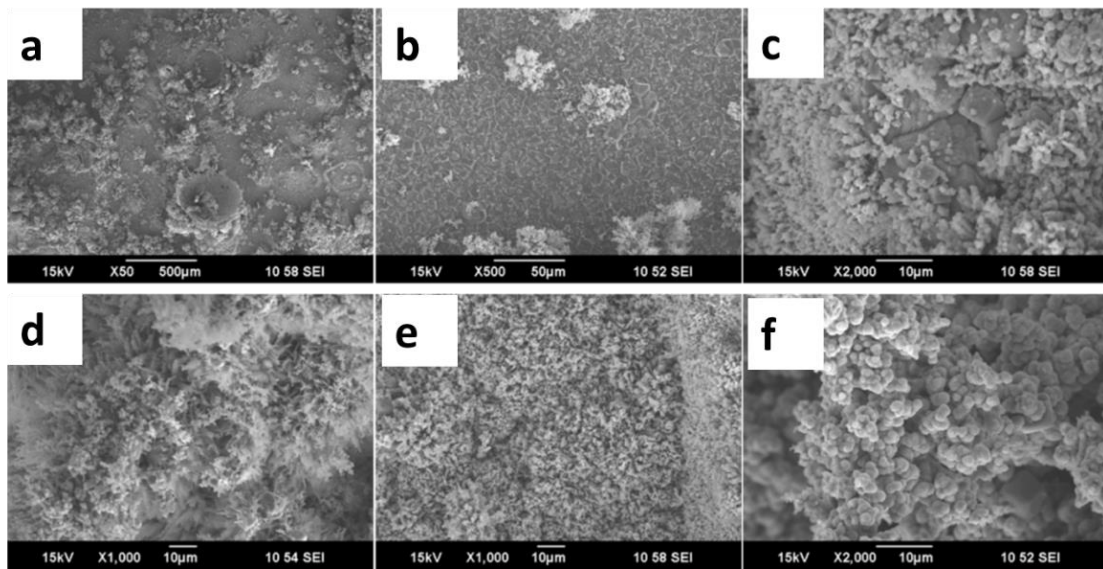
Cross-section after 4 days in 2.5 ppm O₂ (1 wt.% NaCl and 80 °C)



After adding 2.5 ppm of O₂ for 10 days, the test was stopped. The surface morphologies of the specimen at that point are shown in Figure 104. The metal surface has more areas covered by different morphologies of iron oxides, hydroxides and/or oxyhydroxides as compared with the one with O₂ for 4 days (Figure 101a). The EDS result in Figure 105 showed that, compared to FeCO₃ (the middle red rectangle area in Figure 105), those corrosion products (the top and the bottom ones in Figure 105) had more O, Fe and less C. According to the XRD result in Figure 107, it is indicated that besides the main corrosion product of iron carbonate (FeCO₃), magnetite (Fe₃O₄), hematite (Fe₂O₃) and goethite (α -FeO(OH)) were also observed. From the cross-section of the specimen illustrated in Figure 106, a penetration with a depth of 73 μm was observed.

Figure 104

Surface morphology at 6 different locations on the specimen after 10 days in 2.5 ppm O₂ (1 wt.% NaCl and 80 °C)

**Figure 105**

Composition analysis of the corrosion product by EDS after 10 days in 2.5 ppm O₂ (1 wt.% NaCl and 80 °C)

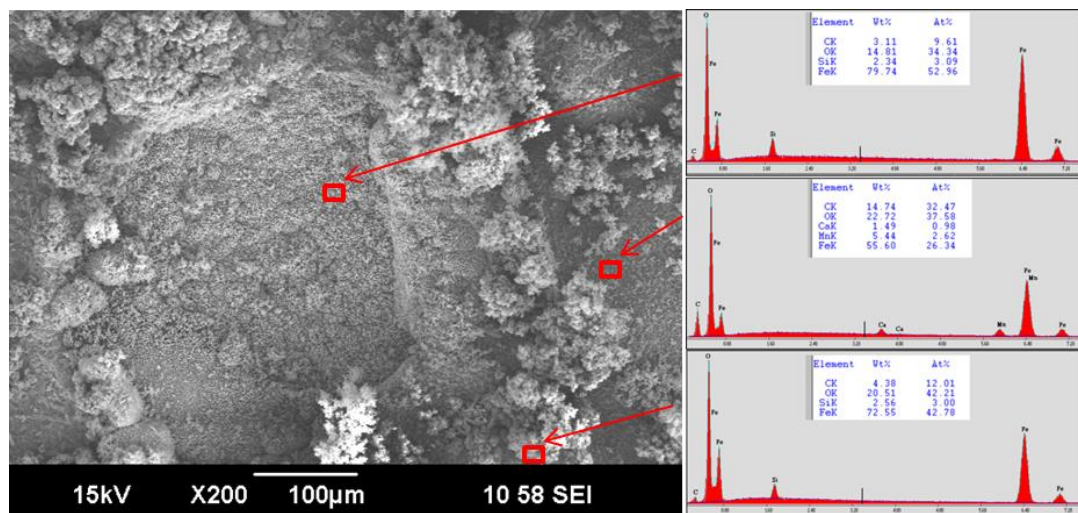
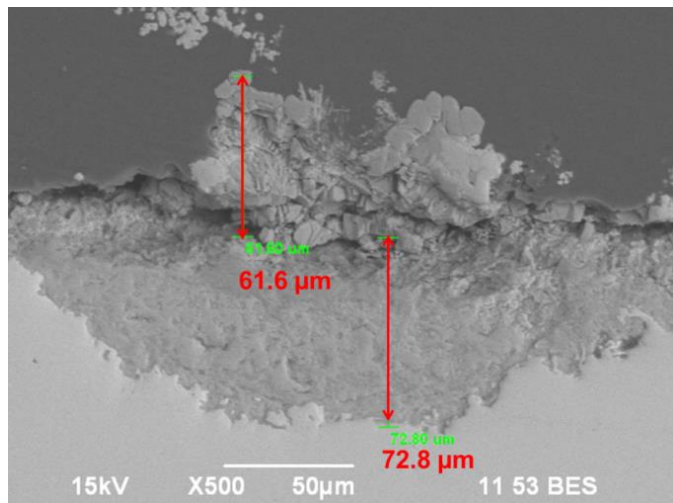
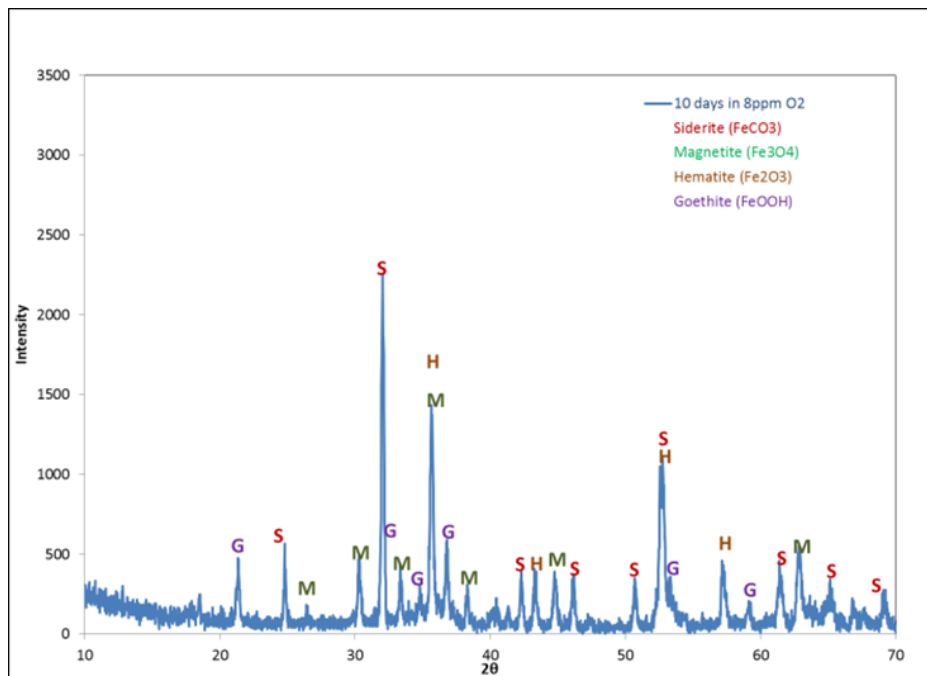


Figure 106

Cross-section after 10 days in 2.5 ppm O₂ (1 wt.% NaCl and 80 °C)

**Figure 107**

XRD analysis after 10 days in 2.5 ppm O₂ (1 wt.% NaCl and 80 °C)



Profilometry (IFM) Analysis and Weight Loss. After exposure to 2.5 ppm O₂ for 10 days, the specimen was characterized using an IFM profilometer. Figure 108 and Figure 109 show 3D morphology before and after the corrosion product removal using Clarke solution [64], respectively. Before the layer removal, tubercles of corrosion product were observed. The red oval marks the same location on the same specimen before and after layer removal, which shows deep pits exposed from underneath the locations of tubercles, the same phenomena were observed during Rosli's research [74].

Figure 108

IFM 3D images of the corrosion product layer before layer removal after 10 days in 2.5 ppm O₂ (1 wt.% NaCl and 80 °C)

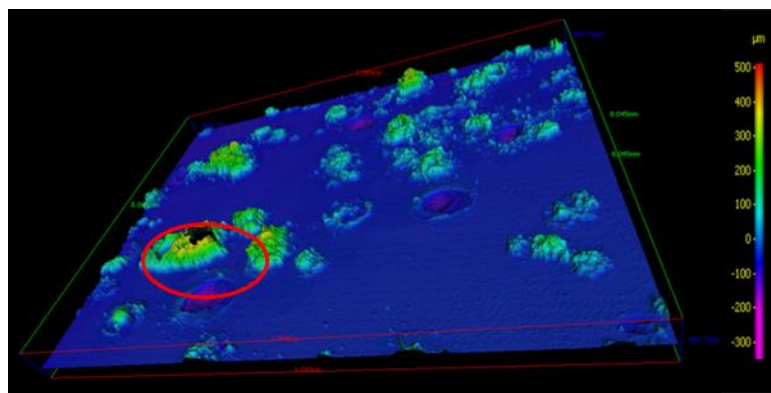
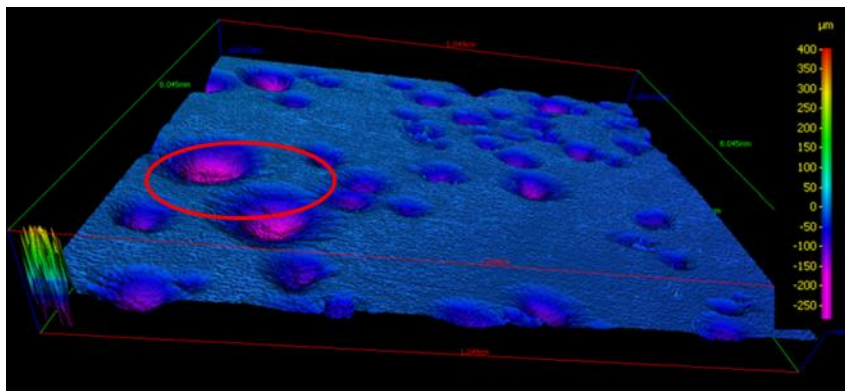
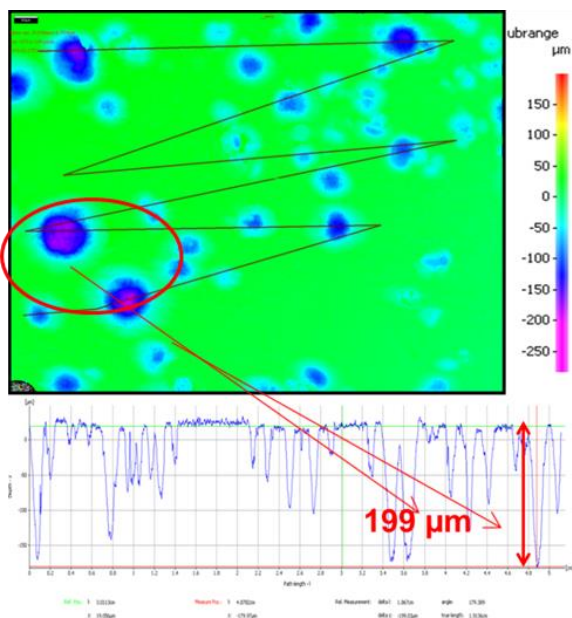


Figure 109

IFM 3D images of the corrosion product layer after layer removal after 10 days in 2.5 ppm O₂ (1 wt.% NaCl and 80 °C)

**Figure 110**

IFM images and analysis of the corrosion product layer after layer removal after 10 days in 2.5 ppm O₂ (1 wt.% NaCl and 80 °C)



As shown in Figure 110, the deepest penetration observed from almost the whole surface was 199 μm ; which was underneath the tubercles before the layer removal. Based on this depth, the pit penetration rate, which is calculated as the depth of the pit divided by the total time (counted from when O₂ ingress to when the specimen was taken out), was 7.3 mm/yr. This specimen was also analyzed by weight loss measurement. The general corrosion rate from the weight loss was 1.2 mm/yr. Therefore, the pitting ratio, which is the ratio of the pit penetration rate with respect to general corrosion rate, was 6:1; suggesting the pitting corrosion rate was much higher than the general corrosion rate, which indicated that it was localized corrosion. Pitting ratio is used as a criterion of localized corrosion, as explained in Appendix II Calculation of General Corrosion Rate, Pitting Penetration Rate and Pitting Ratio.

7.4.2 Test with 1.4 ppm of Dissolved O₂

Localized corrosion was initiated in the presence of 2.5 ppm O₂. Therefore, experiments were conducted with a lower concentration of O₂ in order to determine if localized attack was again initiated.

Corrosion Behavior. Figure 111 shows the change of the [Fe²⁺/Fe³⁺] and pH with time. During the first 5.5 days of 0 ppm O₂, the bulk pH decreased from 6.6 to 6.4 and at the same time the concentration of aqueous Fe ions decreased from 100 ppm to less than 1 ppm. When 1.4 ppm dissolved O₂ was added into the system after 6 days, the solution turned red immediately, indicating Fe²⁺ was oxidized into Fe³⁺ and then precipitated as solid ferric oxides and oxyhydroxides. The total dissolved iron concentration (the sum of

$[Fe^{2+}]$ and $[Fe^{3+}]$) decreased. In the last 8 days, almost no iron ions (only 0.01-0.02 ppm) were detected.

Figure 111

Change of measured bulk pH (red) and measured total ferrous and ferric ion concentration (green) with time, 1.4 ppm of oxygen was added after 6 days (1 wt.% NaCl and 80 °C)

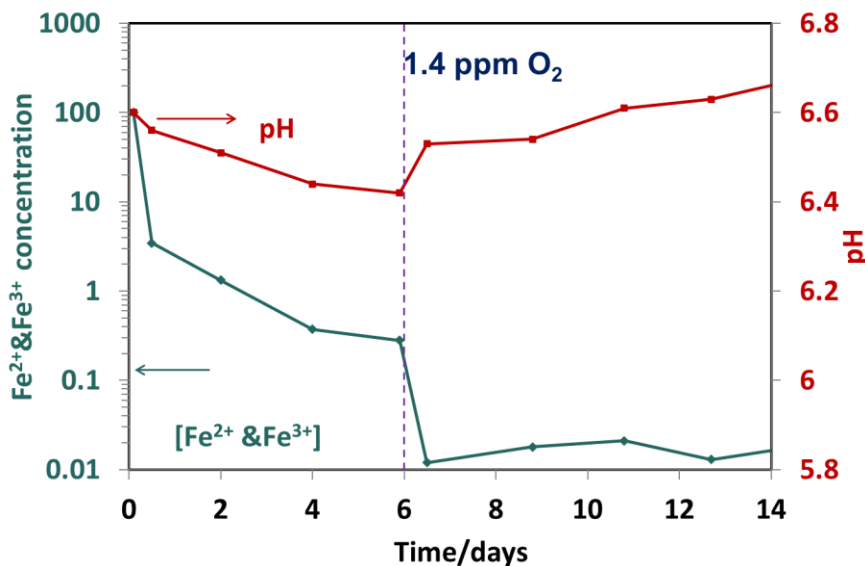
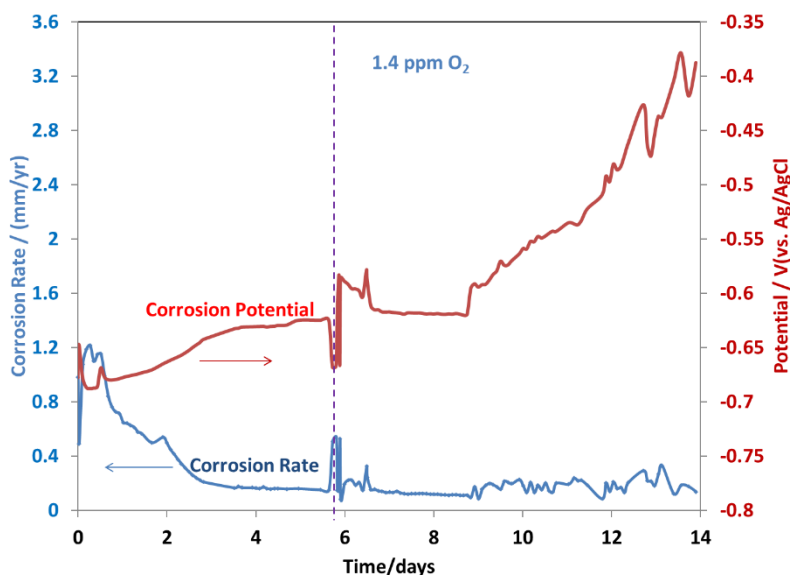


Figure 112 shows the change of the general corrosion rates and corrosion potential with time. Before saturating the solution with the dissolved O_2 , the general corrosion rate and corrosion potential stabilized at around 0.15 mm/yr and -630 mV respectively, suggesting that protective $FeCO_3$ formed on the surface. Once 1.4 ppm dissolved O_2 was introduced into the system continuously, the general corrosion rate increased significantly from 0.15 mm/yr to 0.5 mm/yr and the corrosion potential had a

sudden decline, which indicated that the protectiveness of FeCO_3 was compromised immediately. This instant decrease of corrosion potential was not observed in the test with 2.5 ppm dissolved O_2 . After several hours, the general corrosion rate decreased again and the potential started to increase, perhaps due to the formation of new protective corrosion product; this postulate would be confirmed by surface analysis.

Figure 112

Variation of corrosion rate and corrosion potential with test time as determined by LPR , 1.4 ppm of oxygen was added at 6 days (1 wt.% NaCl and 80 °C)

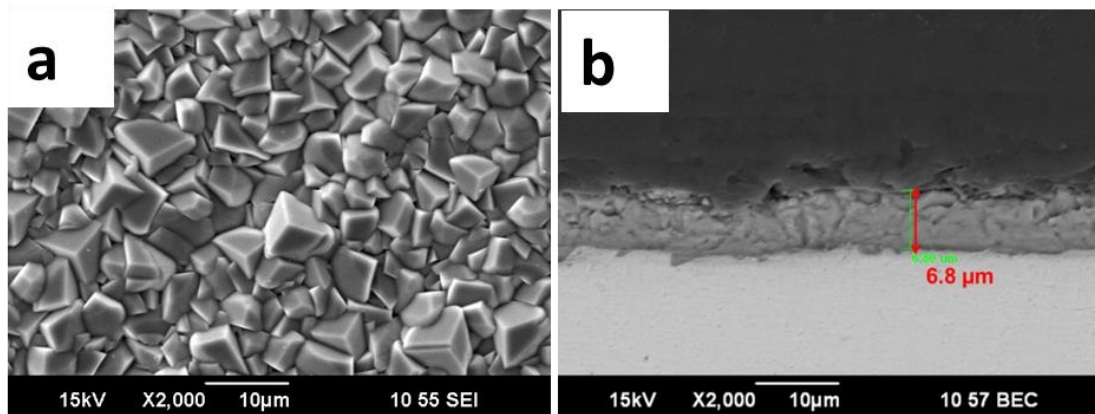


SEM Surface Analysis and XRD Analysis. Figure 113a shows the surface morphology of the developed layer after the 4 days building process. The crystalline layer, consistent with morphological characteristics of FeCO_3 , was dense, compact, and covered the steel completely. The cross-section of the specimen, as shown in Figure

113b, revealed that the FeCO₃ layer was uniform and adherent to the metal with a thickness of around 7 µm.

Figure 113

Surface morphology and cross-section after 4 days in 1 wt. % NaCl (80 °C, initial pH 6.6, initial [Fe²⁺] 100 ppm, and pCO₂ 0.53 bar)



After 1.4 ppm dissolved O₂ had been introduced after 4 days, a specimen was retrieved and examined by SEM (Figure 114). Most of the area of the specimen was still covered with FeCO₃ crystals (as shown in Figure 114a), while morphologies consistent with iron oxides or oxyhydroxides appeared on the surface (Figure 114bcd). XRD analysis (Figure 115) revealed that the corrosion products were composed of iron carbonate (FeCO₃), magnetite (Fe₃O₄), hematite (Fe₂O₃) and goethite (α -FeOOH). From the cross-section of the specimen shown in Figure 116, a tubercle appeared on the surface, which had two layers. The EDS analysis (Figure 117) shows that the outer layer has more Fe (75 wt. %) and less C (5 wt. %) compared the inner layer (Fe 58 wt. % and C

14 wt. %), suggesting that the outer layer is iron oxide or oxyhydroxide and the inner layer iron carbonate.

Figure 114

Surface morphology after 4 days in 1.4 ppm O₂ (1 wt.% NaCl and 80°C)

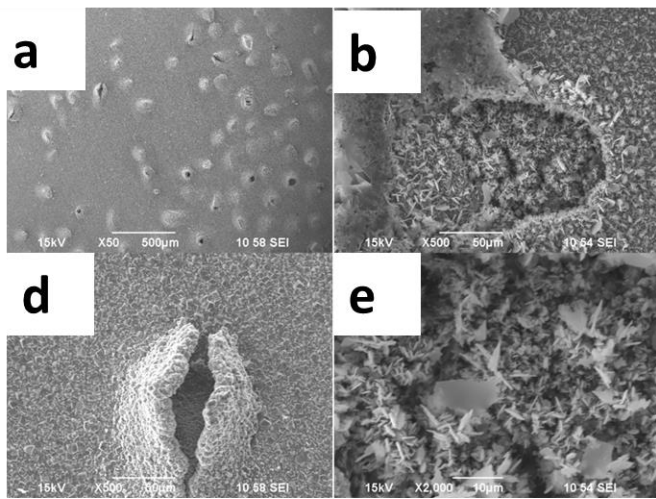
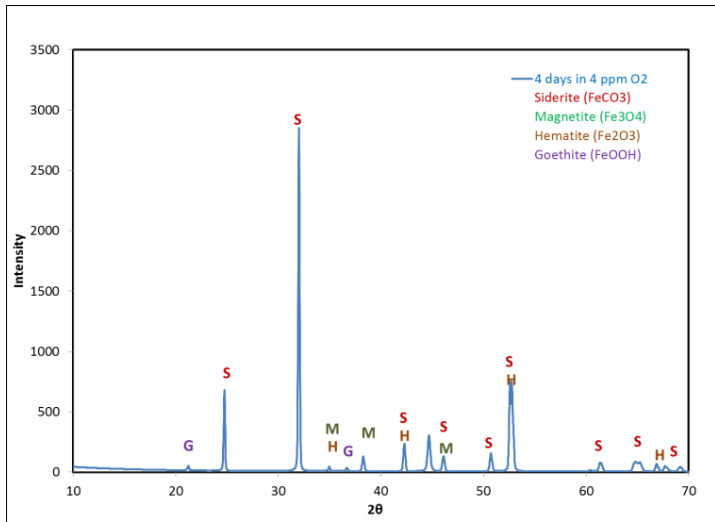


Figure 115

XRD analysis after 4 days in 1.4 ppm dissolved O₂ (1 wt.% NaCl and 80 °C)

**Figure 116**

Cross-section after 4 days in 1.4 ppm dissolved O₂ (1 wt.% NaCl and 80 °C)

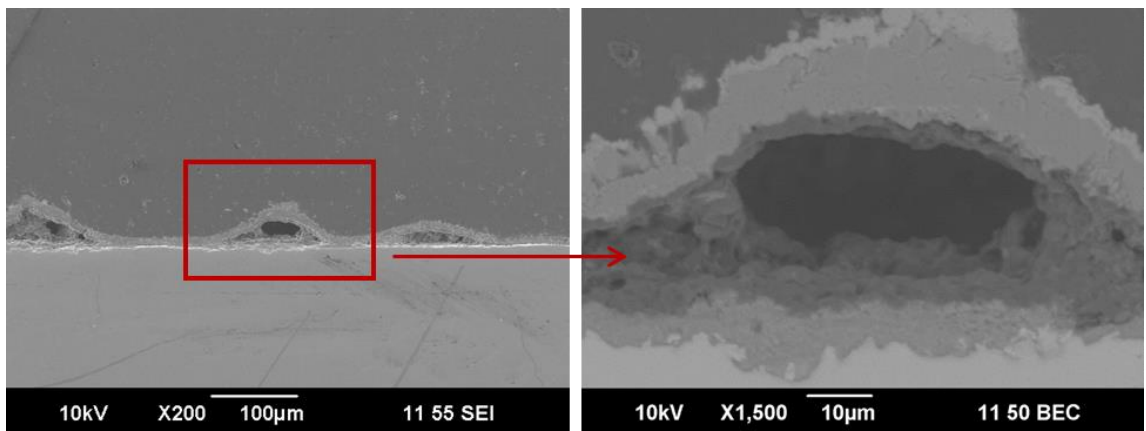
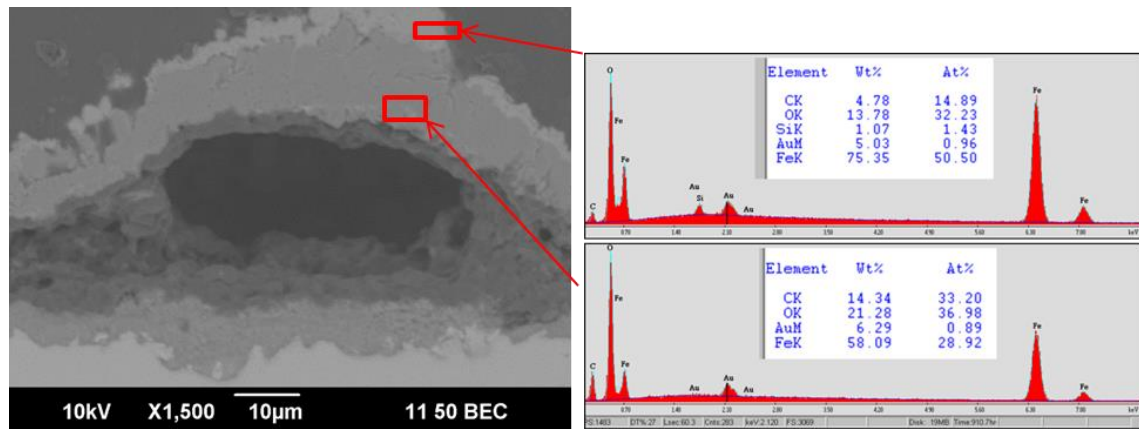


Figure 117

Cross-section and EDS analysis after 4 days in 1.4 ppm dissolved O₂ (1 wt.% NaCl and 80 °C)



On day 14, after having sparged with 1.4 ppm dissolved O₂ for 8 days, another specimen was retrieved. The surface morphologies of the specimen are shown in Figure 118. FeCO₃ was still the main corrosion product on the surface, and XRD analysis (Figure 32) confirmed that the main corrosion products were iron carbonate (FeCO₃), and magnetite (Fe₃O₄), hematite (Fe₂O₃) and goethite (α -FeOOH) were detected. A big tubercle, which had three layers of corrosion product, was observed from the cross-section in Figure 120. The outer layer has the lightest color, which indicated that it had more metal than the middle (darker color) and the inner layer (darker than the other two layers). It appears that a start of localized corrosion was initiated under the tubercle.

Figure 118

Surface morphology after 8 days in 1.4 ppm dissolved O_2 (1 wt.% NaCl and 80 °C)

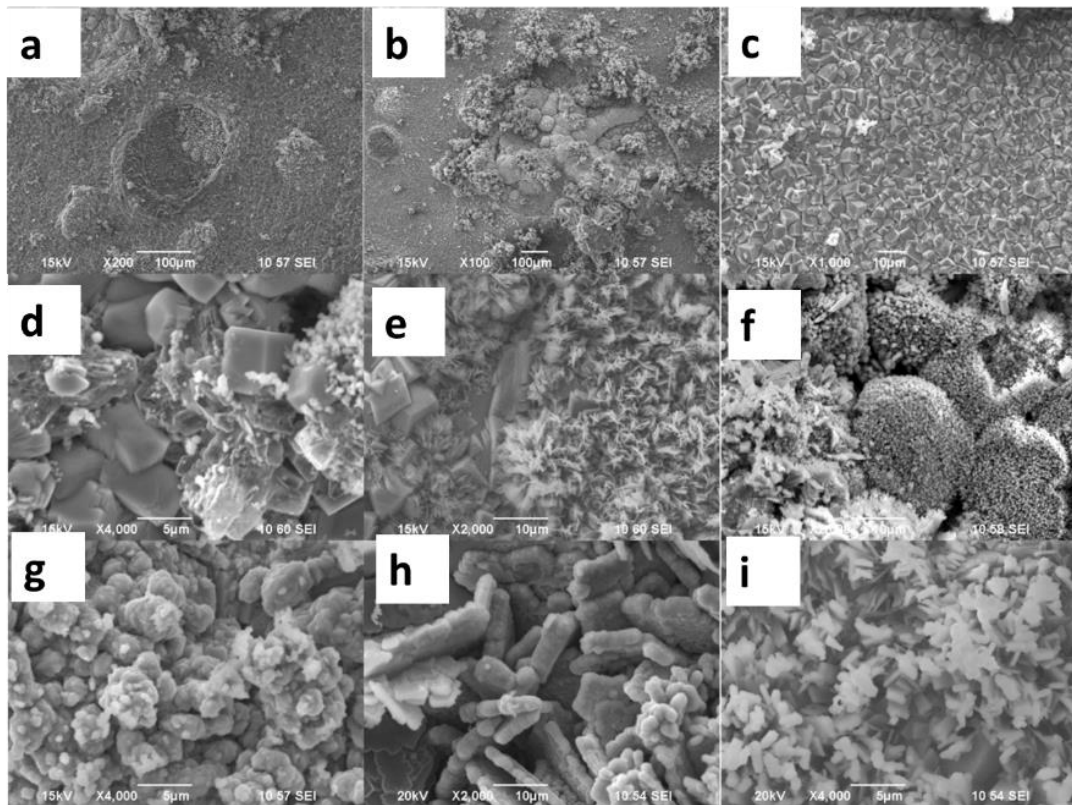
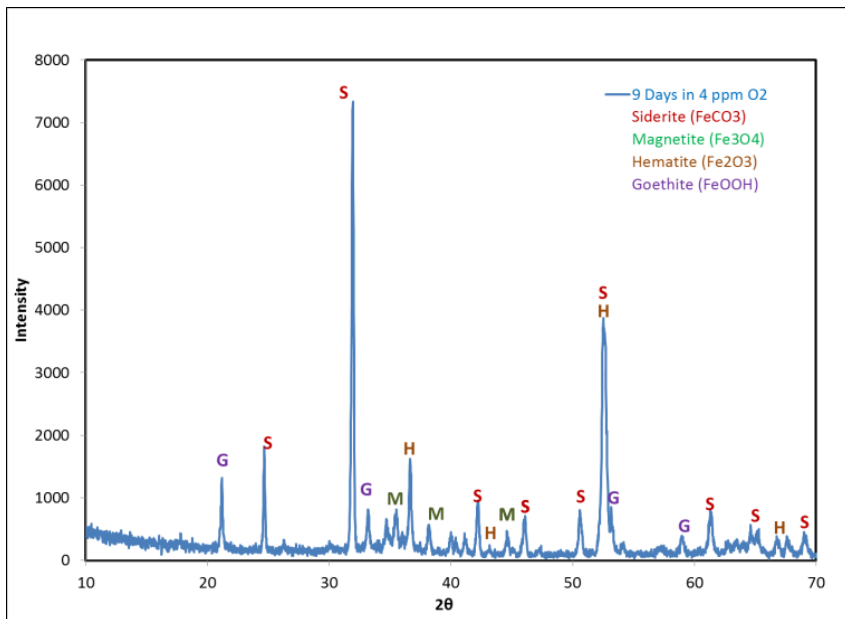
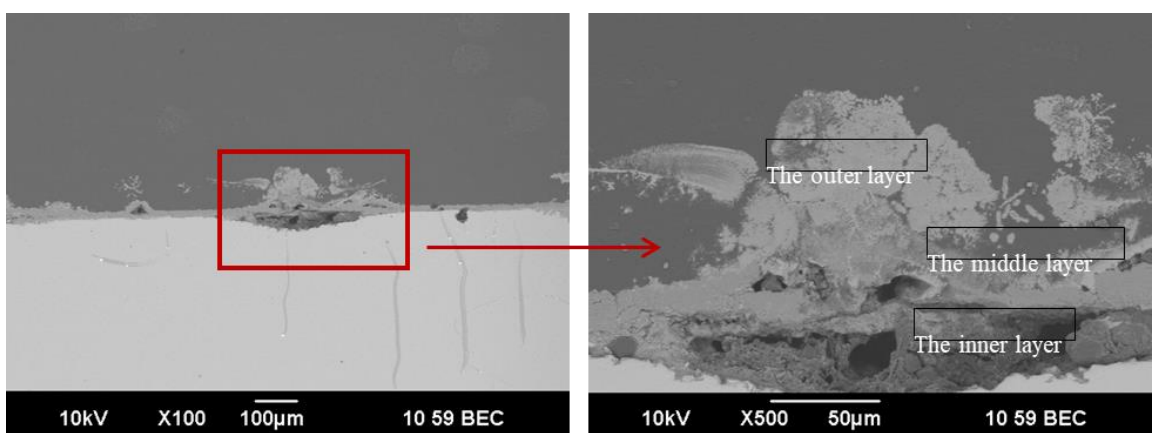


Figure 119

XRD analysis after 8 days in 1.4 ppm dissolved O₂ (1 wt.% NaCl and 80 °C)

**Figure 120**

Cross-section after 8 days in 1.4 ppm dissolved O₂ (1 wt.% NaCl and 80 °C)



Profilometry Analysis (by IFM) and Weight Loss. Figure 121 shows the 3D morphology with corrosion product and Figure 122 shows the 3D morphology after corrosion product removal by Clarke solution [64]. Before the layer removal, some tubercles of corrosion product were observed on the metal surface. After the layer removal, some deep pits became exposed underneath tubercles. From Figure 123, the deepest pit penetration of 64 μm was detected across the whole surface. The pit penetration rate calculated was 2.5 mm/yr and the general corrosion rate from the weight loss was 0.37 mm/yr. Therefore, the pitting ratio was 6.8, larger than 5, which indicated that it was localized corrosion.

Figure 121

IFM 3D images of the corrosion product layer before layer removal after 8 days in 1.4 ppm dissolved O₂ (1 wt.% NaCl and 80 °C)

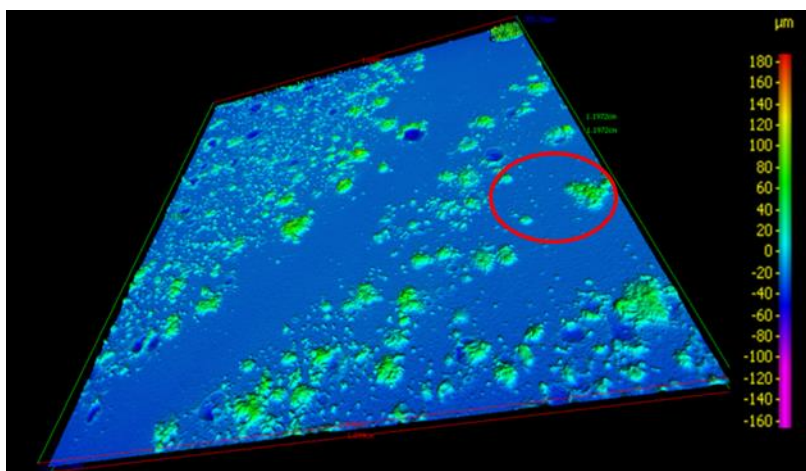
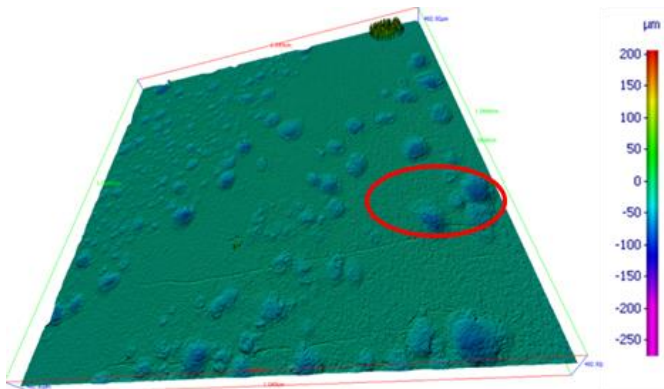
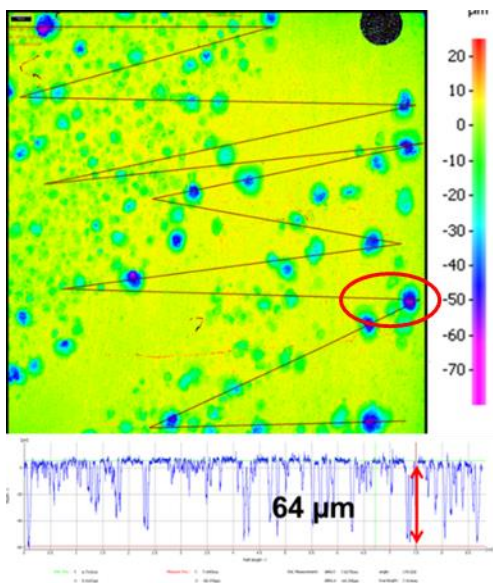


Figure 122

IFM 3D images of the corrosion product layer after layer removal after 8 days in 1.4 ppm dissolved O₂ (1 wt.% NaCl and 80 °C)

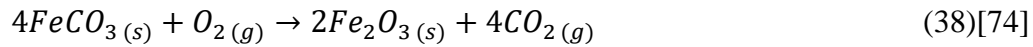
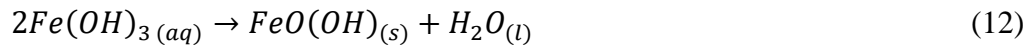
**Figure 123**

IFM images and analysis of the corrosion product layer after layer removal after 8 days in 1.4 ppm dissolved O₂ (1 wt.% NaCl and 80 °C)



7.5 Discussion

Rosli's corrosion mechanism. Rosli [74] proposed a comprehensive corrosion mechanism. Before the ingress of O₂, the surface is protected by formation of a FeCO₃ layer (Figure 124a). When oxygen enters the system, ferrous ions in the electrolyte are oxidized by the introduced O₂ to ferric ions and then insoluble iron oxide is formed (shown in equations (35), (37), (12) and (13)). Then, iron oxide precipitates (Figure 124b). O₂ is reduced according to equation (36). At the same time, part of the iron carbonate layer reacts with O₂ as shown in equation (38), forming iron oxide. About 48.8% volume is reduced due to the conversion of 2 moles FeCO₃ into 1 mole Fe₂O₃. Consequently, void spaces within the iron carbonate layer is created (Figure 124c).



It is hypothesized in Rosli's mechanism that an acid micro-environment develops in the cavity. More CO₂ and H₂ gas releases and is confined under the corrosion product layer, leading to higher pressure inside, causing the cavity to become bigger (Figure 124d). Inwards O₂ diffusion is retarded by the outer layer. In the cavity, O₂ is consumed and an oxygen deficient area is created. This O₂ deficient area works as an anode and the larger surface works as a cathode. Therefore, crevice corrosion is developed. Underneath

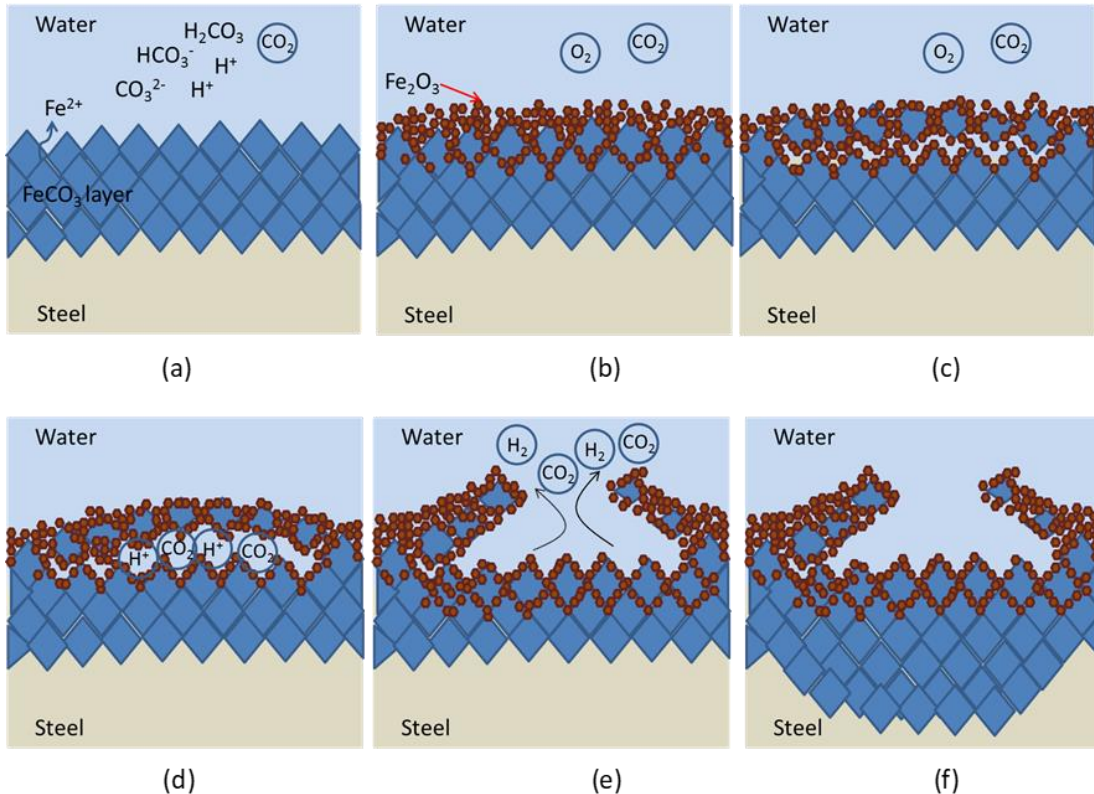
the tubercle, more ferrous and ferric ions are produced according to the anodic reactions (equations (1) and (35)).

The top layer of the cavity breaks due to the higher and higher build-up of pressure under it or the stress at the crystal boundaries (Figure 124e). The burst tubercle works as an anode and the rest of the specimen surface works as a cathode. Then a galvanic cell for corrosion is developed. The localized corrosion occurs under the burst tubercle, causing more FeCO_3 to form in the area where metal loss occurred, which explains how the FeCO_3 layer became thicker in Figure 103 than that shown in Figure 96 before introducing O_2 (Figure 124d).

Rosli's mechanism explains why there was cavity formation under the tubercle, why there were two FeCO_3 layers between the cavity, and why the FeCO_3 layer on the metal surface is thickened after the ingress of O_2 . However, more work is still needed to further prove this postulate.

Figure 124

Proposed tuberculation mechanism by Rosli in CO₂ corrosion with O₂ intrusion, taken from Roslin[74]



7.6 Summary

- Severe pitting corrosion was observed with introduction of 1.4 ppm or 2.5 ppm dissolved O₂.
- Corrosion potential increased significantly with introduction of 1.4 ppm or 2.5 ppm of dissolved O₂ while corrosion rate did not have a significant change.

- Iron oxides or ferric oxyhydroxides, such as magnetite (Fe_3O_4), hematite (Fe_2O_3), and goethite ($\alpha\text{-FeOOH}$) were detected by XRD. However, FeCO_3 was still the main corrosion product.
- Pits were found underneath the tubercles of iron oxides/oxyhydroxides. However, tubercles can also occur with shallow or no pits.
- Ingress of O_2 can partially damage FeCO_3 and then initiate localized corrosion in CO_2 environments.
- Rosli's mechanism can be used to explain the phenomena, although more work is needed to prove it.

Chapter 8: Conclusions and Future Work

Conclusions

The work described in this dissertation investigated the mechanism of CO₂ localized corrosion initiation on mild steel, including the effects of chloride, oxygen and acetic acid. The following can be concluded:

- Saturation of FeCO₃ was decreased by increasing the ionic strength by adding either NaCl or NaClO₄. But localized corrosion was not initiated by adding more salts.
- A new water chemistry model based on Oddo & Tomson's equation was proposed by the author. Predicted pH values by the new model are in better agreement with measured values over the temperature range from 30°C to 80°C and changes in ionic strength from 1 wt.% to 25 wt.% aqueous NaCl.
- Based on EQCM results, a new model to calculate the solubility constant of iron carbonate in non-ideal solution at 80°C was developed based on Sun & Nesic model. S_{FeCO₃} from the new proposed model reflects the experimental values from EQCM and the previous experiments in Chapter 4 with better accuracy.
- The presence of acetic acid initiated localized corrosion in a CO₂ saturated environment. The addition of a buffered HAc solution increased ionic strength but was not the reason for initiation of localized corrosion.
- Introduction of 1.4 ppm or 2.5 ppm of dissolved O₂ can partially damage FeCO₃ and then initiate localized corrosion in CO₂ environments.

Recommendations for future work

- All the experiments were done at 80°C and 1 bar total pressure for the chloride effect. More experiments at different temperatures should be conducted, for example, at 70°C and 60°C, to check how temperature affects the saturation of FeCO_3 in non-ideal solution.
- The dissertation does not cover the use of corrosion inhibitors. The interaction between a corrosion inhibitor and chlorides or high ionic strength solutions may need to be considered.
- It was shown that the presence of HAc increased the rate of pitting corrosion, but the mechanism of HAc on CO_2 localized corrosion is still unclear and needs further study.
- Ingress of O_2 can partially damage FeCO_3 and then initiate localized corrosion in CO_2 environments. Although, Rosli's mechanism can be used to explain the phenomena, more work is needed to prove it.

References

- [1] S. Papavinasam, A. Doiron, R. W. Revie, and V. Sizov, "A model to predict internal pitting corrosion of oil and gas pipelines," CORROSION/2007, Houston, TX, 2007, paper no.07658.
- [2] S. Nesic, "Key issues related to modelling of internal corrosion of oil and gas pipelines—a review," *Corros. Sci.*, vol. 49, no. 12, pp. 4308–4338, 2007.
- [3] S. Papavinasam, A. Doiron, and R. W. Revie, "Effect of surface layers on the initiation of internal pitting corrosion in oil and gas pipelines," *Corrosion*, vol. 65, no. 10, 2009.
- [4] S. Nesic and W. Sun, "Corrosion in acid gas solutions," in *Shreir's Corrosion*, Tony J.A. Richardson, Ed. Oxford: Elsevier, 2010, pp. 1270–1298.
- [5] A. Kahyarian, "Mechanism and prediction of mild steel corrosion in aqueous solutions containing carboxylic acids, carbon dioxide, and hydrogen sulfide," Ph.D. dissertation, Ohio University, Athens, OH, 2018.
- [6] T. N. B. Tran, "Corrosion mechanisms of mild steel in weak acids.," Ph.D. dissertation, Ohio University, 2014.
- [7] V. Ruzic, "Mechanisms of protective FeCO_3 film removal in single-phase flow-accelerated CO_2 corrosion of mild steel," Ph.D. dissertation, School Eng. Phys. Sci. and Arch., University of Queensland, Australia, 2006.
- [8] C. De Waard and D. E. Milliams, "Carbonic acid corrosion of steel," *Corrosion*, vol. 31, no. 5, pp. 177–181, 1975.
- [9] C.de Waard and U. Lotz, "Prediction of CO_2 corrosion of carbon steel," CORROSION/1993, Houston, Texas, 1993, paper no. 69, 1993.
- [10] C.de Waard, U. Lotz, and A. Dugstad, "Influence of liquid flow velocity on CO_2 corrosion: a semi-empirical model," CORROSION/1995, Houston, TX, 1995, paper no. 95128.
- [11] L. G. Gray, B. G. Anderson, M. J. Danysh, and P. R. Tremaine, "Effect of pH and temperature on the mechanism of carbon steel corrosion by aqueous carbon dioxide," *Corros. Pap.*, no. 40, pp. 1–26, 1990.
- [12] S. Nesic, Magnus Nordsveen, Rolf Nyborg, and A. Stangeland, "Mechanistic modeling for CO_2 corrosion with protective iron carbonate films," CORROSION/2001, Houston, Texas, 2001, paper no.01040.
- [13] S. Nesic, M. Nordsveen, R. Nyborg, and A. Stangeland, "A mechanistic model for carbon dioxide corrosion of mild steel in the presence of protective iron carbonate films-part 2: a numerical experiment," *Corrosion*, vol. 59, no. 6, pp. 489–497, 2003.
- [14] S. Nesic and K. L. J. Lee, "A mechanistic model for carbon dioxide corrosion of mild steel in the presence of protective iron carbonate films-part 3: film growth model," *Corrosion*, vol. 59, no. 7, pp. 616–628, 2003.

- [15] S. Nesic, H. Li, J. Huang, and D. Sormaz, "An open source mechanistic model for CO₂ / H₂S corrosion of carbon steel," CORROSION/2009, Houston, TX, 2009, paper no.09752.
- [16] A. Kahyarian, M. Achour, and S. Nesic, "Mathematical modeling of uniform CO₂ corrosion," in *Trends in Oil and Gas Corrosion Research and Technologies*, A. M. El-Sherik, Ed. Boston: Woodhead Publishing, 2017, pp. 805–849.
- [17] S. M. Sharland, "A review of the theoretical modelling of crevice and pitting corrosion," *Corros. Sci.*, vol. 27, no. 3, pp. 289–323, 1987.
- [18] G. S. Frankel, "Localized corrosion of metals: a review of the rate-controlling factors in initiation and growth," in *Passivity of Metals and Semiconductors: Proceedings of the Eighth International Symposium*, The Electrochemical Society, 2001.
- [19] T. P. Hoar, D. C. Mears, and G. P. Rothwell, "The relationships between anodic passivity, brightening and pitting," *Corros. Sci.*, vol. 5, no. 4, pp. 279–289, Jan. 1965.
- [20] C. Y. Chao, L. F. Lin, and D. D. Macdonald, "A point defect model for anodic passive films: I. film growth kinetics," *J. Electrochem. Soc.*, vol. 128, no. 6, p. 1187, 1981.
- [21] H. H. Uhlig, "Adsorbed and reaction-product films on metals I," *J. Electrochem. Soc.*, vol. 97, no. 11, p. 6, 1950.
- [22] J. Han, D. Young, H. Colijn, A. Tripathi, and S. Nesic, "Chemistry and structure of the passive film on mild steel in CO₂ corrosion environments," *Ind. Eng. Chem. Res.*, vol. 48, no. 13, pp. 6296–6302, 2009.
- [23] W. Li, "Investigation of pseudo-passive layer formation in CO₂ corrosion," M.S. Thesis, Ohio University, Athens, OH, 2011.
- [24] H. Li, "A mechanistic model for CO₂ localized Corrosion of carbon Steel," Ph.D dissertation, Ohio University, Athens, OH, 2011.
- [25] Y. Yang, "Removal mechanisms of protective iron carbonate layer in flowing solutions," Ohio University, Ph.D. dissertation, Ohio University, Athens, OH, 2012.
- [26] S. Iteamsupapong, "Mechanisms of Iron Carbonate Formation on Mild Steel in Controlled Water Chemistry Conditions," Ph.D. dissertation, Ohio University, Athens, OH, 2016.
- [27] A. Dugstad, "Mechanism of protective film formation during CO₂ corrosion of carbon steel," CORROSION/1998, Houston, Texas, 1998, paper no.98031.
- [28] J. Han, "Galvanic mechanism of localized corrosion for mild steel in carbon dioxide environments," Ph.D. dissertation, Ohio University, Athens, OH, 2009.
- [29] R. Nyborg, "Initiation and growth of mesa corrosion attack during CO₂ corrosion of carbon steel," CORROSION/1998, Houston, Texas, 1998, paper no.98048.

- [30] J. Han, Y. Yang, B. Brown, and S. Nesić, “Electrochemical investigation of localized CO₂ corrosion on mild steel,” Corrosion/2007, Houston, TX, 2007, paper no. 07323.
- [31] R. Nyborg and A. Dugstad, “Understanding and prediction of mesa corrosion attack,” Corrosion/2003, Houston, TX, 2003, paper no. 03642, 2003.
- [32] Q. Y. Liu, L. J. Mao, and S. W. Zhou, “Effects of chloride content on CO₂ corrosion of carbon steel in simulated oil and gas well environments,” *Corros. Sci.*, vol. 84, pp. 165–171, Jul. 2014, doi: 10.1016/j.corsci.2014.03.025.
- [33] H. Fang, “Low temperature and high salt concentration effects on general CO₂ corrosion for carbon steel,” Master Thesis, Ohio University, Athens, OH, 2006.
- [34] G. Schmitt and S. Feinen, “Effect of anions and cations on the pit initiation in CO₂ corrosion of iron and steel,” CORROSION/2000, Houston, TX, paper no.00001.
- [35] Z. Ma, “Precipitation Kinetics of FeCO₃ and FeS in Non-ideal Solutions,” Institute for Corrosion and Multiphase Technology, Chemical Engineering, Ohio University, Athens, OH, 04, Apr. 2018.
- [36] Z. Ma, “Precipitation Kinetics of FeCO₃ in Non-Ideal Solutions,” Institute for Corrosion and Multiphase Technology, Chemical Engineering, Ohio University, Athens, OH, 04, Mar. 2019.
- [37] F. Madani Sani, “Effect of Chloride on Corrosion of Carbon Steels,” Institute for Corrosion and Multiphase Technology, Chemical Engineering, Ohio University, Athens, OH, 12, Oct. 2017.
- [38] J. E. Oddo and M. B. Tomson, “Simplified calculation of CaCO₃ saturation at high temperatures and pressures in brine solutions,” *J. Pet. Technol.*, vol. 34, no. 07, pp. 1–583, 1982.
- [39] Z. Duan and R. Sun, “An improved model calculating CO₂ solubility in pure water and aqueous NaCl solutions from 273 to 533 K and from 0 to 2000 bar,” *Chem. Geol.*, vol. 193, no. 3, pp. 257–271, Feb. 2003.
- [40] H. Zhao, M. V. Fedkin, R. M. Dilmore, and S. N. Lvov, “Carbon dioxide solubility in aqueous solutions of sodium chloride at geological conditions: experimental results at 323.15, 373.15, and 423.15K and 150bar and modeling up to 573.15K and 2000bar,” *Geochim. Cosmochim. Acta*, vol. 149, pp. 165–189, Jan. 2015.
- [41] Y. Sun, “Localized CO₂ corrosion in horizontal wet gas flow,” Ph.D. dissertation, Ohio University, Athens, OH, 2003.
- [42] R. L. Martin, “Corrosion consequences of oxygen entry into oilfield brines,” CORROSION/2002, Houston, TX, 2002, paper no. 02270.
- [43] X. Jiang, “Effect of oxygen contamination on CO₂ corrosion in presence of FeCO₃ film,” ICMT, Chemical Engineering, Ohio University, Athens, OH, 11, Nov. 2008.

- [44] B. W. A. Sherar, P. G. Keech, Z. Qin, F. King, and D. W. Shoesmith, "Nominally anaerobic corrosion of carbon steel in near-neutral pH saline environments," *Corrosion*, vol. 66, no. 4, pp. 045001–045001, 2010.
- [45] S. Wang, "Effect of oxygen on CO₂ corrosion of mild steel," M.S. thesis, Ohio University, Athens, OH, 2009.
- [46] F. M. Song, D. W. Kirk, J. W. Graydon, and D. E. Cormack, "CO₂ corrosion of bare steel under an aqueous boundary layer with oxygen," *J. Electrochem. Soc.*, vol. 149, no. 11, pp. B479–B486, 2002.
- [47] K. George, S. Nesic, and K. de Waard, "Electrochemical investigation and modeling of carbon dioxide corrosion of carbon steel in the presence of acetic acid," CORROSION/2004, Houston, TX, paper no. 04379, Jan. 2004.
- [48] J. L. Crolet, A. L. Dugstad, and N. L. Thevenot, "Role of free acetic acid on the CO₂ corrosion of steels," CORROSION/1999, Houston, TX, 1999, paper no. 99024.
- [49] J. Amri, E. Gulbrandsen, and R. P. Nogueira, "Effect of acetic acid on propagation and stifling of localized attacks in CO₂ corrosion of carbon steel," CORROSION/2009, Houston, TX, 2009, paper no. 09284, 2009.
- [50] V. Fajardo, "Localized CO₂ corrosion in the presence of organic acids," M.S. thesis, Ohio University, Athens, OH, 2011.
- [51] D. Pletcher, D. Sidorin, and B. Hedges, "A comparison of the corrosion of carbon and 13% chromium steels in oilfield brines containing acetate," CORROSION/2005, Houston, TX, 2005, paper no. 05301.
- [52] J. Amri, E. Gulbrandsen, and R. P. Nogueira, "Role of acetic acid in CO₂ top of the line corrosion of carbon steel," CORROSION/2011, Houston, TX, 2001, paper no. 11329.
- [53] M. Nordsveen, S. Nesic, R. Nyborg, and A. Stangeland, "A mechanistic model for carbon dioxide corrosion of mild steel in the presence of protective iron carbonate films-Part 1: theory and verification," *Corrosion*, vol. 59, no. 5, pp. 443–456, 2003.
- [54] Y. K. Kharaka, W. D. Gunter, and P. K. Aggarwal, "Solmineq.88; a computer program for geochemical modeling of water-rock interactions," U.S. Geological Survey, Menlo Park, CA, 88–4227, 1988. Accessed: Dec. 12, 2019. [Online]. Available: <https://pubs.er.usgs.gov/publication/wri884227>.
- [55] D. A. Palmer and R. Van Eldik, "The chemistry of metal carbonato and carbon dioxide complexes," *Chem. Rev.*, vol. 83, no. 6, pp. 651–731, Dec. 1983.
- [56] D. Li and Z. Duan, "The speciation equilibrium coupling with phase equilibrium in the H₂O–CO₂–NaCl system from 0 to 250 °C, from 0 to 1000 bar, and from 0 to 5 molality of NaCl," *Chem. Geol.*, vol. 244, no. 3, pp. 730–751, Oct. 2007, doi: 10.1016/j.chemgeo.2007.07.023.
- [57] C. E. Harvie, N. Møller, and J. H. Weare, "The prediction of mineral solubilities in natural waters: The Na-K-Mg-Ca-H-Cl-SO₄-OH-HCO₃-CO₃-H₂O system to high

- ionic strengths at 25°C,” *Geochim. Cosmochim. Acta*, vol. 48, no. 4, pp. 723–751, Apr. 1984, doi: 10.1016/0016-7037(84)90098-X.
- [58] E. Hoyer, “stability constants of metal-ion complexes part a: inorganic ligands,” *Z. Für Chem.*, vol. 23, no. 6, pp. 236–236, doi: 10.1002/zfch.19830230632.
- [59] “Cole-Parmer pH electrode, Refillable, low maintenance from Cole-Parmer.” <https://www.coleparmer.com/i/cole-parmer-ph-electrode-refillable-low-maintenance/0599181?searchterm=5991-81> (accessed Dec. 31, 2019).
- [60] A. E. Markham and K. A. Kobe, “The solubility of carbon dioxide and nitrous oxide in aqueous salt solutions,” *J Am Chem Soc*, vol. 2, no. 63, pp. 449–454, Feb. 1941, doi: 10.1021/ja01847a027.
- [61] Z. Ma, Y. Yang, B. Brown, S. Nesic, and M. Singer, “Investigation of precipitation kinetics of FeCO₃ by EQCM,” *Corros. Sci.*, vol. 141, pp. 195–202, Aug. 2018, doi: 10.1016/j.corsci.2018.06.017.
- [62] W. Sun, “Kinetics of iron carbonate and iron sulfide scale formation in CO₂/H₂S Corrosion,” Ph.D. dissertation, Ohio University, Athens, OH, 2006.
- [63] T. Tanupabrungsun, “Thermodynamics and kinetics of carbon dioxide corrosion of mild steel at elevated temperatures,” Ph.D. dissertation, Ohio University, Athens, OH, 2012.
- [64] ASTM G1-03 (2013), “Standard practice for preparing, cleaning, and evaluating corrosion test specimens,” 2003.
- [65] B. Brown, “The likelihood of localized corrosion in an H₂S/CO₂ environment,” CORROSION/2015, Houston, Texas, 2015, paper no. 5855, p. 15.
- [66] ASTM G46 - 94(2018), “Standard guide for examination and evaluation of pitting corrosion.”
- [67] F. Madani Sani, “Effect of salt concentration on uniform CO₂ corrosion of carbonsteels,” Institute for Corrosion and Multiphase Technology, Chemical Engineering, Ohio University, Athens, OH, Board meeting report, Apr. 2018.
- [68] J. Kestin, H. E. Khalifa, and R. J. Correia, “Tables of the dynamic and kinematic viscosity of aqueous KCl solutions in the temperature range 25–150 °C and the pressure range 0.1–35 MPa,” *J. Phys. Chem. Ref. Data*, vol. 10, no. 1, pp. 57–70, Jan. 1981, doi: 10.1063/1.555640.
- [69] G. Sauerbrey, “Verwendung von schwingquarzen zur wägung dünner schichten und zur mikrowägung,” *Z. Für Phys.*, vol. 155, no. 2, pp. 206–222, Apr. 1959.
- [70] “DR /3000 Procedure Code I.2, Method 8146, page 2-179.” .
- [71] F. Madani Sani, B. Brown, Z. Belarbi, and S. Nesic, “An experimental investigation on the effect of salt concentration on uniform CO₂ Corrosion,” CORROSION/2019, Houston, TX, 2019, paper no.13026.

- [72] A. Dugstad, "Fundamental aspects of CO₂ metal loss corrosion part I: mechanism," CORROSION/2006, Houston, TX, 2006, paper no. 06111, 2006.
- [73] J. L. Crolet, N. Thevenot, and S. Nesic, "Role of conductive corrosion products in the protectiveness of corrosion layers," *Corrosion*, vol. 54, no. 3, pp. 194–203, 1998.
- [74] N. R. Rosli, "The effect of oxygen in sweet corrosion of carbon steel for enhanced oil recovery applications," Ph.D. dissertation, Ohio University, Athens, OH, 2015.
- [75] C. Han, D. Zhao, C. Deng, and K. Hu, "A facile hydrothermal synthesis of porous magnetite microspheres," *Mater. Lett.*, vol. 70, pp. 70–72, Mar. 2012, doi: 10.1016/j.matlet.2011.11.115.
- [76] M. Gotić and S. Musić, "Mössbauer, FT-IR and FE SEM investigation of iron oxides precipitated from FeSO₄ solutions," *J. Mol. Struct.*, vol. 834–836, pp. 445–453, May 2007, doi: 10.1016/j.molstruc.2006.10.059.
- [77] J. Štajdohar, M. Ristić, and S. Musić, "The effect of experimental conditions on the microstructure of hematite particles precipitated by the forced hydrolysis of FeCl₃ solutions," *J. Mol. Struct.*, doi: 10.1016/j.molstruc.2012.09.073.
- [78] M. Carbucicchio, R. Cipriani, F. Ospitali, and G. Palombarini, "Morphology and phase composition of corrosion products formed at the zinc–iron interface of a galvanized steel," *Corros. Sci.*, vol. 50, no. 9, pp. 2605–2613, Sep. 2008, doi: 10.1016/j.corsci.2008.06.007.
- [79] Perry, Robert H. and Green, Don W., *Perry's Chemical Engineers' Handbook*, 7th ed. McGraw-Hill Professional, 1997.
- [80] D. Tromans, "Temperature and pressure dependent solubility of oxygen in water: a thermodynamic analysis," *Hydrometallurgy*, vol. 48, no. 3, pp. 327–342, May 1998, doi: 10.1016/S0304-386X(98)00007-3.
- [81] Degrémont, s.a, *Water treatment handbook*, 7th [English] ed. Rueil-Malmaison, France : Cachan, France: Degrémont ; Distributed by Lavoisier, 2007.
- [82] M. Geng and Z. Duan, "Prediction of oxygen solubility in pure water and brines up to high temperatures and pressures," *Geochim. Cosmochim. Acta*, vol. 74, no. 19, pp. 5631–5640, Oct. 2010, doi: 10.1016/j.gca.2010.06.034.
- [83] F. J. Millero, F. Huang, and A. L. Laferiere, "Solubility of oxygen in the major sea salts as a function of concentration and temperature," *Mar. Chem.*, vol. 78, no. 4, pp. 217–230, Jun. 2002, doi: 10.1016/S0304-4203(02)00034-8.

Appendix A: Procedure of Iron Ion Measurement

Before measuring $[Fe^{2+} + Fe^{3+}]$, it helps to have a rough understanding of how much $[Fe^{2+}]$ in your test solution. If $[Fe^{2+}] < 3\text{ppm}$, there is no need to dilute the sample. If $[Fe^{2+} + Fe^{3+}] > 3\text{ppm}$, then the solution needs to be diluted so $[Fe^{2+} + Fe^{3+}] < 3\text{ppm}$. For example, if $[Fe^{2+} / Fe^{3+}]$ is estimated to be around 10 ppm, the solution will be diluted to 5 times with DI water. This process might need some trial and error before the correct dilution is determined.

Measured by A Thermo Scientific GENESYS 10vis Spectrophotometer

Step 1: take 5 ml solution from the test equipment (for example, glass cell).

Step 2: filter the 5ml solution by using a syringe with $0.45\mu\text{m}$ filter.

Step 3: add 20ml (dependent on how many times it is supposed to dilute) DI H_2O to dilute the solution 5 times as mentioned at the beginning.

Step 4: take 10ml of the diluted solution and inject it into a container.

Step 5: add a package of *FerroVer®Iron Reagent* (for determination of iron by the 1,10 phenanthroline method) into the container and mix it well.

Step 6: wait at least 3 minutes. Then, fill a cuvette with one-half to three-quarters full.

Step 7: measure by Thermo Scientific GENESYS 10vis Spectrophotometer according to the procedure posted next to the instrument and write down the value.

Measured by HACH spectrophotometer (Method 8146 [70]

Step 1: Enter the program mode by pressing “2 5 STORED PROGRAM” and rotate the wavelength selector dial to “510 nm”.

Step 2: take 5 ml solution from the test equipment (for example, glass cell).

Step 3: filter the 5ml solution by using a syringe with 0.45 μ m filter.

Step 4: add 55ml (dependent on how many times it is supposed to dilute) DI H₂O to dilute the solution 12 times as mentioned at the beginning.

Step 5: take 25ml of the diluted solution and inject it into a clean sample cell.

Step 6: add a package of *FerroVer®Iron Reagent* (for determination of iron by the 1,10 phenanthroline method) into the sample cell and mix it well.

Step 7: wait 3 minutes. Then, fill a second sample cell with 25 ml of the sample in Step 4.

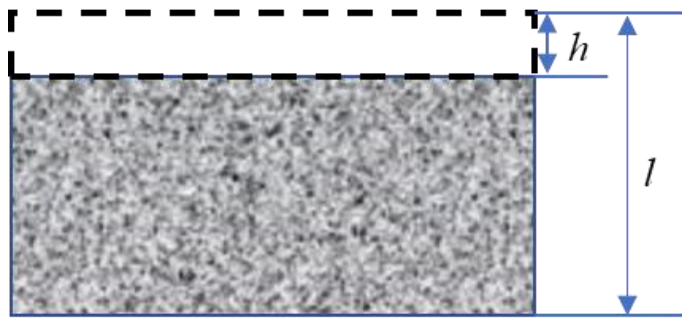
Step 8: measure by the Spectrophotometer according to the procedure posted next to the instrument and write down the value.

Appendix B: Calculation of General Corrosion Rate, Pitting Penetration Rate and Pitting Ratio

General corrosion rate:

Figure 125

Cross section diagram of a weight loss specimen



$$\text{General corrosion rate}(\text{mm/yr}) = \frac{h}{t}$$

$$h = \frac{V}{A}$$

$$V = \frac{\Delta m}{d}$$

Δm = the original weight before the test

– the weight after the test after Clarke solution

l is the original height of the specimen, mm.

h is the height that is corroded away, mm.

t is the total test time, year.

V is the volume of the corroded part of the specimen, mm³.

A is the surface area of the specimen, mm².

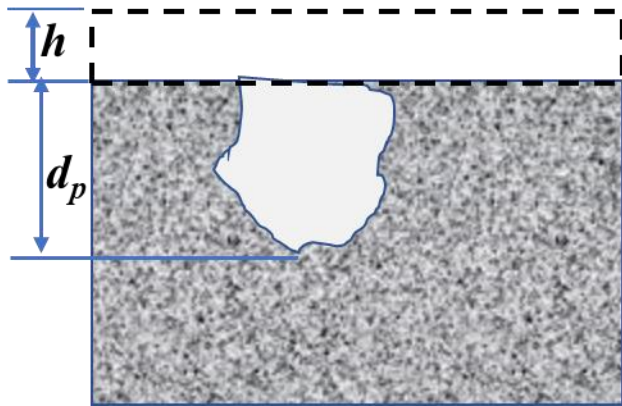
Δm is the weight loss of the specimen, g.

d is the density of the specimen, g/mm^3 .

Pitting penetration rate [65]:

Figure 126

Cross section diagram of a weight loss specimen with a pitting



$$\text{Pit penetration rate (mm/yr)} = \frac{d_p}{t}$$

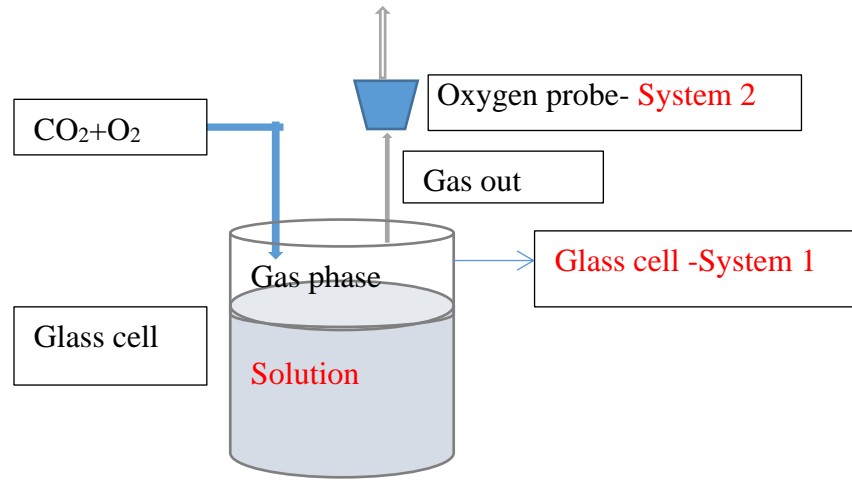
d_p is measured pit depth by IFM, mm.

Pitting ratio [65]:

$$\text{Pitting ratio} = \frac{\text{General corrosion rate}}{\text{Pit penetration rate}}$$

Qualifying Statement	Result
Pitting Ratio < 3	Not localized corrosion.
3 < Pitting Ratio < 5	Possible localized corrosion
Pitting Ratio > 5	Localized corrosion.

Appendix C: Calculation of the Dissolved Oxygen Concentration in The Glass Cell



Assumptions:

- The pressure of gas out is equal to the one of gas in.
- The volumes of gas phase in glass cell (defined as System 1) and oxygen probe (defined as System 2) are much bigger than all the tubing. Therefore, the volumes of the tubing can be ignored.
- The molar ratio (equal to the ratio of the partial pressure) of CO₂ and O₂ is same in System 1 and System 2.
- Total pressure of each system is 1 bar.

Conditions:

System 1: T=80°C=353K, p₁CO₂+p₁O₂+p₁H₂O=1

System 2: T=25°C=298K, p₂CO₂+p₂O₂+p₂H₂O=1,

Question: what is the concentration of dissolved O₂ in System 1?

Calculation:

System 2:

The partial pressure of H₂O is dependent on temperature and pressure of the system,

$$p_2H_2O = f(P, T) = 0.03 \text{ bar} [79]$$

[O₂]₂ = K_{O2} p₂O₂ (Henry's Law, K_{O2} is Henry's law constant of oxygen)

Read from oxygen meter, we got [O₂]₂ = 8 ppm = 2.5E-4 mol/L.

K_{O2} is related to temperature, based on the literature[80],

$$k_{O2}$$

$$= \exp \left\{ \frac{0.046T^2 + 203.35T \ln \left(\frac{T}{298} \right) - (299.378 + 0.092T)(T - 298) - 20.591 \times 10^3}{8.3144T} \right\} \quad (39)$$

at T=298K, K_{O2}=0.001278 mol/L/bar

So, p₂O₂ = C_{O2}/ K_{O2} = 0.195 bar.

Then, p₂CO₂ = 1 - 0.03 - 0.195 = 0.775 bar

So, p₂O₂: p₂CO₂ = 0.195:0.775

System 1:

At T=353K, p₁H₂O=f (P, T)=0.47 bar

So, p₁O₂+ p₁CO₂=0.53 bar and p₁O₂: p₁CO₂=0.195:0.775

So, p₁O₂=0.1 bar, p₁CO₂=0.43 bar at 353 K and 8 ppm O₂ measured with the oxygen probe.

And at T=353K, K_{O2}=0.000793 mol/L/bar (from equation (39))

$$[O_2]_1 = 7.94E-5 \text{ M} = 2.53 \text{ ppm}$$

The solubility of oxygen at 353K at 0.1 bar of the pressure of oxygen is 2.46 ppm.[81]

So, when the reading number of oxygen meter is 8 ppm in the liquid phase at 298K (25 °C), the dissolved oxygen concentration in the glass cell at 80 °C is 2.46 ppm.

Similarly, when the reading number of oxygen meter is 4 ppm in the liquid phase at 298K (25 °C), the dissolved oxygen concentration in the glass cell at 80 °C is 1.35 ppm.

This calculation is based on oxygen solubility in pure water. During the test, the solution was 1 wt. % NaCl (0.17M). According to literature[82][83], oxygen solubility was affected by the concentration of NaCl. However, 0.17M is very low and the solution is still ideal. As shown in Table 13, when the concentration of NaCl is less than 0.3M, the difference is negligible.

Table 13

Solubility of oxygen in NaCl solutions as a function of temperature and concentration[80]

Temperature (°C)	Molality of NaCl	[O ₂] μmol (kg H ₂ O) ⁻¹
25	0	258.9
25	0.1589	248
25	0.3034	238.3
25	0.5165	223.3
25	0.7857	206.7
25	0.9694	195.9
25	1.5151	169.8
25	2.0337	148.6
25	2.6664	127
25	2.8916	120.4
25	4.0404	93.6
25	5.0069	77.3

Appendix D: Mass Change, S_{FeCO_3} and pH Variation on a Polarized Au-coated Crystal at Various Accumulated NaCl concentrations from 10 wt.% to 25 wt.%.

Figure 127

Mass change (left) and S_{FeCO_3} (right) obtained on a polarized Au-coated quartz crystal with adding more NaCl (10 wt.%) at 80°C

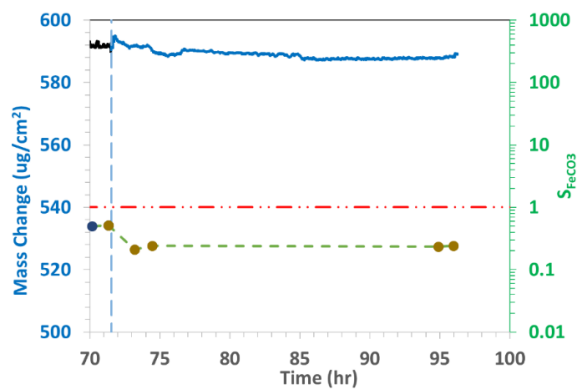
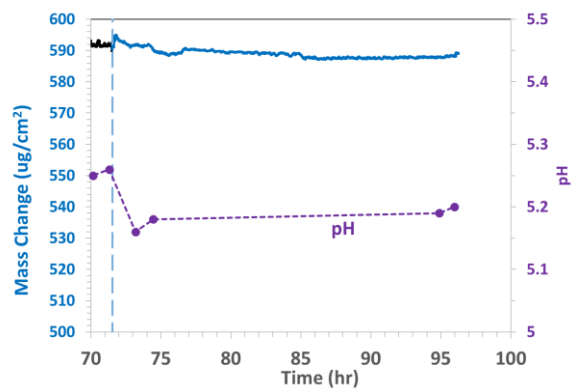


Figure 128

Mass change (left) and the pH variation (right) on a polarized Au-coated quartz crystal with adding more NaCl (10 wt.%) at 80°C

**Figure 129**

Mass change (left) and S_{FeCO_3} (right) obtained on a polarized Au-coated quartz crystal with adding more NaCl (15 wt.%) at 80°C

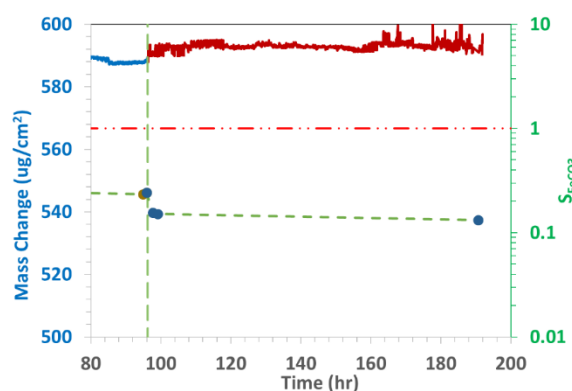
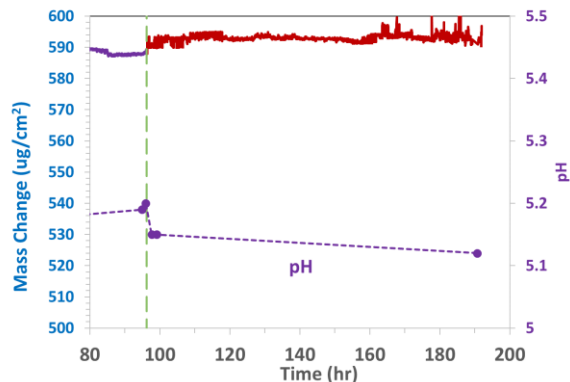


Figure 130

Mass change (left) and the pH variation (right) on a polarized Au-coated quartz crystal with adding more NaCl (15 wt.%) at 80°C

**Figure 131**

Mass change (left) and S_{FeCO_3} (right) obtained on a polarized Au-coated quartz crystal with adding more NaCl (25 wt.%) at 80°C

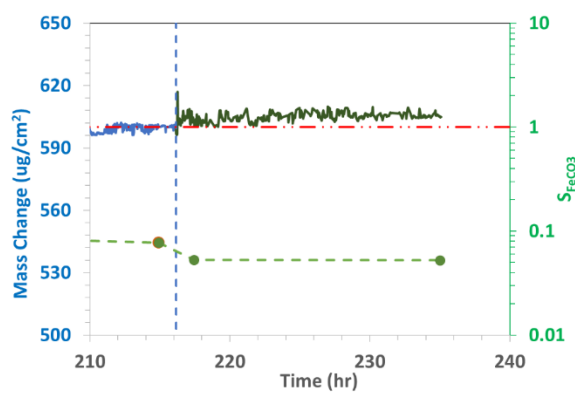
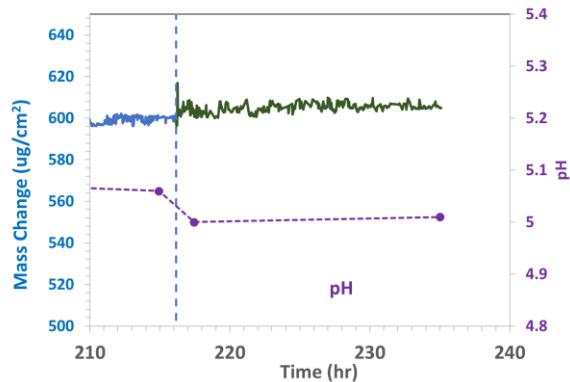


Figure 132

Mass change (left) and the pH change variation (right) obtained on a polarized Au-coated quartz crystal with adding more NaCl (25 wt.%) at 80°C

**Figure 133**

Mass change (left) and S_{FeCO_3} (right) obtained on a polarized Au-coated quartz crystal with adding more NaCl (20 wt.%) at 80°C

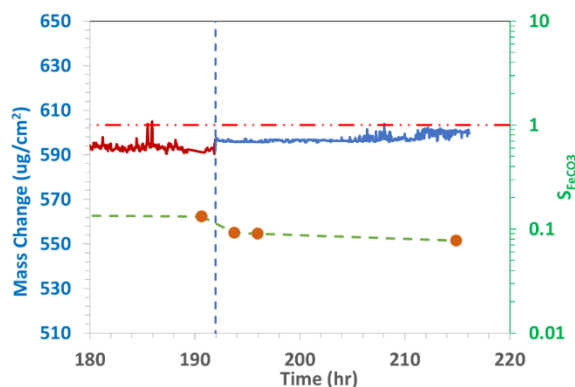
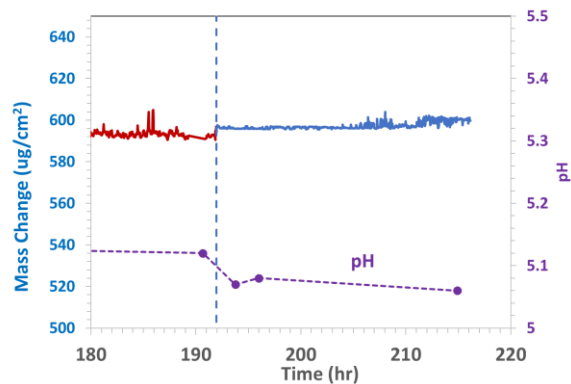


Figure 134

Mass change (left) and the pH variation (right) on a polarized Au-coated quartz crystal with adding more NaCl (20 wt.%) at 80°C





Thesis and Dissertation Services